

CORRELATION OF RESTITUTION COEFFICIENT: EXPERIMENT AND  
COMPUTATIONAL FLUID DYNAMICS SIMULATION



A Dissertation Submitted in Partial Fulfillment of the Requirements  
for the Degree of Doctor of Philosophy in Chemical Technology

Department of Chemical Technology

FACULTY OF SCIENCE

Chulalongkorn University

Academic Year 2019

Copyright of Chulalongkorn University

สหสัมพันธ์ของสัมประสิทธิ์การคืนสู่สภาพเดิม: การทดลองและการจำลองพลศาสตร์ของไหลเชิง  
คำนวณ



วิทยานิพนธ์นี้เป็นส่วนหนึ่งของการศึกษาตามหลักสูตรปริญญาวิทยาศาสตรดุษฎีบัณฑิต

สาขาวิชาเคมีเทคนิค ภาควิชาเคมีเทคนิค

คณะวิทยาศาสตร์ จุฬาลงกรณ์มหาวิทยาลัย

ปีการศึกษา 2562

ลิขสิทธิ์ของจุฬาลงกรณ์มหาวิทยาลัย



ธรรมาธิบดี ยุระดา : สหสัมพันธ์ของสัมประสิทธิ์การคืนสู่สภาพเดิม: การทดลองและการจำลอง  
 พลศาสตร์ของไหลเชิงคำนวณ. ( CORRELATION OF RESTITUTION COEFFICIENT:  
 EXPERIMENT AND COMPUTATIONAL FLUID DYNAMICS SIMULATION) อ.ที่ปรึกษาหลัก  
 : รศ. ดร.เบญจพล เฉลิมสินสุวรรณ, อ.ที่ปรึกษาร่วม : ศ. ดร.พรพจน์ เปี่ยมสมบุญ, ดร.ยูซิง เฟิง

การจำลองพลศาสตร์ของไหลเชิงคำนวณด้วยวิธีดิสครีทเอลิเมนต์ (Computational fluid dynamics with discrete element method) ถูกนำมาใช้อย่างกว้างขวาง เพื่อทำนายพลศาสตร์ของการไหลหลายวัฏภาคระหว่างของไหล และของแข็ง หรือกระบวนการฟลูอิดเซชัน ค่าสัมประสิทธิ์การชน (Coefficient of restitution) เป็นหนึ่งในตัวแปรที่สำคัญ และจำเป็นต่อการศึกษาพลศาสตร์ของไหลเชิงคำนวณ ด้วยวิธีดิสครีทเอลิเมนต์ ค่าสัมประสิทธิ์การชนมีนิยาม คืออัตราส่วนของความเร็วสัมพัทธ์หลังการชนกับความเร็วสัมพัทธ์ก่อนการชน การใช้ค่าสัมประสิทธิ์การชนที่เหมาะสม ทำให้การจำลองพลศาสตร์ของไหลเชิงคำนวณสามารถทำนายการชนกันของของแข็งได้สมจริง อย่างไรก็ตามปัจจุบันค่าสัมประสิทธิ์การชนนี้ถูกเลือกโดยการลองผิดลองถูกในการจำลองพลศาสตร์ของไหลเชิงคำนวณแบบดั้งเดิม เนื่องจากไม่มีวิธีการอ้างอิงมาตรฐานสำหรับค่าสัมประสิทธิ์การชนนี้

ในการศึกษานี้ ความสำคัญของค่าสัมประสิทธิ์การชนได้ถูกศึกษา นอกจากนี้ผลกระทบของวัสดุแข็ง ความเร็วกระแทก และอุณหภูมิที่มีต่อค่าสัมประสิทธิ์การชน ได้ถูกสร้างขึ้นจากผลการทดลองการตกอย่างอิสระ โดยพฤติกรรมการชนถูกบันทึกด้วยกล้องความเร็วสูง และใช้การวิเคราะห์ภาพ (Image analysis) เพื่อวัดค่าสัมประสิทธิ์การชน จากนั้นสหสัมพันธ์จะถูกพัฒนาผ่านความสัมพันธ์ของความเร็วกระแทก ไมโครสโคปียัดหยุ่น อัตราส่วนของบิวชอง และอุณหภูมิ การจำลองพลศาสตร์ของไหลเชิงคำนวณด้วยวิธีดิสครีทเอลิเมนต์ โดยใช้ค่าสัมประสิทธิ์การชนแบบค่าคงที่ และแบบพลวัตถูกนำมาเปรียบเทียบ ในระบบต่างๆ เช่น เครื่องปฏิกรณ์ฟลูอิดเบดที่เชื่อมต่อกันสามเครื่อง เครื่องปฏิกรณ์ฟลูอิดเบด แบบหมุนเวียนภายใน ถังปั่นหมุน และสเปาเต็ดเบด ผลลัพธ์ที่ได้แสดงความสำคัญของการจำลองพลศาสตร์ของไหลเชิงคำนวณด้วยกระบวนการวิธีดิสครีทเอลิเมนต์โดยการใช้ค่าสัมประสิทธิ์การชนแบบพลวัต และได้แนวทางในการใช้งานค่านี้ต่อไป

สาขาวิชา เคมีเทคนิค

ปีการศึกษา 2562

ลายมือชื่อ นิสิต .....

ลายมือชื่อ อ.ที่ปรึกษาหลัก .....

ลายมือชื่อ อ.ที่ปรึกษาร่วม .....

ลายมือชื่อ อ.ที่ปรึกษาร่วม .....

# # 5872813923 : MAJOR CHEMICAL TECHNOLOGY

KEYWORD: CFD-DEM simulation, Contact force, Coefficient of restitution

Tarabordin Yurata : CORRELATION OF RESTITUTION COEFFICIENT: EXPERIMENT AND COMPUTATIONAL FLUID DYNAMICS SIMULATION. Advisor: Assoc. Prof. BENJAPON CHALERMSINSUWAN, Ph.D. Co-advisor: Prof. PORNPOTE PIUMSOMBOON, Ph.D., Yuqing Feng, Ph.D.

The computational fluid dynamics with the discrete element method (CFD-DEM) is widely used to predict the hydrodynamics profile of the multiphase flow of fluid-solid or fluidization process. The coefficient of restitution (COR) is one of the most important parameters which is vital for CFD-DEM simulation. This parameter denotes the ratio of the relative velocity after the collision to the relative velocity before the collision. The appropriate value of the coefficient of restitution must receive attention to obtain the realistic collision and hydrodynamics profile. However, this parameter is still selected by trial and error in traditional CFD-DEM due to the lacking of the standard reference for this collision parameter.

In this study, the significance of COR in multiphase flow systems was investigated. In addition, the effect of solid materials, impact velocity and temperature on the COR were investigated by the free-fall experiment. The collision behaviour was captured by a high-speed camera and the image analysis was employed to interpret the result. The new correlation was then proposed in terms of impact velocity, elastic modulus, Poisson's ratio, and temperature. The CFD-DEM simulations using a constant value of COR were compared with the CFD-DEM simulation using the correlation of the coefficient of restitution in the various systems such as three interconnected fluidized bed reactors, spouted bed reactor, internal circulating fluidized bed (ICFB) and rotating drum. The obtained results showed the importance of the correlation of dynamics COR and the guideline for further using this collision parameter.

Field of Study: Chemical Technology

Academic Year: 2019

Student's Signature .....

Advisor's Signature .....

Co-advisor's Signature .....

Co-advisor's Signature .....

## ACKNOWLEDGEMENTS

My deep gratitude goes first and foremost to my supervisor, Assoc. Prof. Dr. Benjapon Chalermnsinsuwan who gives me the golden opportunity. I respect for his dedication and expert guidance involving both life and research which continually inspire me including the past, present and future. I would like to acknowledge Prof. Dr. Pornpote Piumsomboon as my co-advisor for the insightful criticism, numerous perspectives, critical suggestion and positive energy which promote the curiosity to accomplishment. I would like to express my deepest appreciation to Dr. Yuqing Feng who push me up to gain the profound and invaluable experience in the frontier research institute namely "The Commonwealth Scientific and Industrial Research Organisation (CSIRO)". I am extremely grateful to Dr. Liangguang Tang who fulfil the hole of knowledge with closely take care and rigorous imparting knowledge. I also would like to extend my deepest gratitude to Dr. Chao'en Li who gives me the important occasion and publication. I am also sincerely grateful to Dr. Doki Yamaguchi who supports and treats me with friendly and good intention. I'd like to recognize the assistance for image analysis that I received from Surapol Vorapatratom, Ph.D. candidate. I also wish to thank to Panuwat Vichuviwat and Kirana Ko-udomvit who always beside as the best friends, Dr. Sutthichai Boonprasop as brother, Dr. Prathana Nimmanterdwong as sister and Thorfun Leathee for a good relationship. I also have great pleasure to be friend with Wenjie Rong, Jason J. Sun and Piriya Roeksahakul. Thanks should also go to my college from cybernetics laboratory group for a good working environment.

Finally, my success will not have been possible without the enormous support and encouragement from my lovely parents.

This study is funded by a scholarship from the Thailand Research Fund (TRF), Thailand through the Royal Golden Jubilee Ph.D. Program (Grant No. PHD/0042/2558). The facilities are supported by Department of Chemical Technology, Faculty of Science, Chulalongkorn University and Department of Energy, The Commonwealth Scientific and Industrial Research Organisation (CSIRO).

Tarabordin Yurata

## TABLE OF CONTENTS

	Page
.....	iii
ABSTRACT (THAI).....	iii
.....	iv
ABSTRACT (ENGLISH) .....	iv
ACKNOWLEDGEMENTS.....	v
TABLE OF CONTENTS.....	vi
LIST OF TABLES.....	xi
LIST OF FIGURES .....	xiii
Chapter 1 Introduction .....	1
1.1 Background.....	1
1.2 Objectives .....	3
1.3 Scope of the dissertation .....	3
Chapter 2 Theory and literature review.....	4
2.1 Computational fluid dynamics simulation.....	4
2.1.1 TFM simulation .....	7
2.1.1.1 The momentum equations .....	7
2.1.1.2 The kinetic theory of granular flow.....	8
2.1.1.3 Momentum interphase transfer.....	9
2.2 DEM simulation .....	10
2.2.1 Contact model .....	11
2.3 MFIX open source code.....	14

2.4 Coefficient of restitution .....	19
2.5 The important of the coefficient of restitution on CFD simulation.....	22
2.6 Literature review.....	23
CHAPTER 3 Methodology .....	30
3.1 Study the effect of coefficient of restitution and contact parameters on CFD simulation.....	30
3.1.1 CFD simulation of three interconnected fluidized bed reactors using TFM approach.....	31
3.1.2 Geometry and initial and boundary conditions.....	32
3.1.3 Numerical configuration.....	35
3.2 CFD simulation of internal circulating fluidized bed (ICFB) using DEM approach	37
3.2.1 Geometry and initial and boundary conditions.....	37
3.2.2 Numerical configuration.....	39
3.3 CFD simulation of rotating drum using DEM approach .....	41
3.3.1 Geometry and initial and boundary conditions.....	41
3.3.2 Numerical configuration.....	42
3.4 CFD simulation of the spouted bed using DEM approach .....	43
3.4.1 Geometry and initial and boundary conditions.....	43
3.4.2 Numerical configuration .....	45
3.4.3 Numerical configuration: Experimental design.....	47
3.5 Develop the correlation of coefficient of restitution from experimental results and other literature results .....	53
3.5.1 COR measurement.....	53
3.5.2 Image analysis .....	56



3.5.3 Correlation of coefficient of restitution .....	58
3.6 Develop the CFD-DEM with the dynamics coefficient of restitution.....	59
CHAPTER 4 Sensitivity analysis of the coefficient of restitution in a various computational fluid dynamics (CFD) simulation models using one-factor-at-a-time (OFAT) methodology .....	61
4.1 CFD simulation of three interconnected fluidized bed reactors using TFM approach .....	61
4.1.1 Grid independency .....	61
4.1.2 Model validation .....	63
4.1.3 The effect of coefficient of restitution on the hydrodynamics profile .....	65
4.2 CFD simulation of internal circulating fluidized bed (ICFB) using DEM approach	68
4.2.1 Grid independency .....	68
4.2.2 The effect of coefficient of restitution on the hydrodynamics profile of internal circulating fluidized bed (ICFB) .....	69
4.3 CFD simulation of rotating drum using DEM approach .....	73
4.3.1 The effect of coefficient of restitution on the hydrodynamics profile of rotating drum .....	73
4.4 CFD simulation of the spouted bed using DEM approach .....	76
4.4.1 Grid independency test.....	76
4.4.2 The effect of coefficient of restitution on the hydrodynamics profile of the spouted bed.....	77
4.5 Conclusion .....	79
CHAPTER 5 Study the effect of contact parameters on CFD-DEM simulation on spouted bed reactor .....	80
5.1 Model validation .....	80

5.2 The $2^k$ factorial experimental design .....	84
5.2.1 Effect of contact force modeling parameters on kinetic energy .....	86
5.2.2 Effect of contact force modeling parameters on the bed expansion ratio... 93	
5.2.3 Effect of contact force modeling parameters on the standard deviation of the pressure drop.....	99
5.4 Conclusion .....	104
CHAPTER 6 Developing the correlation of coefficient of restitution from experimental results and other literature results.....	105
6.1 The effect of diameter on the coefficient of restitution .....	105
6.2 The effect of impact velocity on the coefficient of restitution .....	106
6.3 The effect of material type on the coefficient of restitution.....	108
6.4 The effect of temperature on the coefficient of restitution.....	109
6.5 The correlation of coefficient of restitution.....	113
6.6 The validation of correlation coefficient of restitution by free fall of the single particle .....	119
6.7 Conclusion .....	124
CHAPTER 7 The development of the CFD-DEM simulation with the dynamics coefficient of restitution .....	125
7.1 Internal circulating fluidized bed .....	125
7.2 Rotating drum.....	132
7.3 Spouted bed .....	134
7.4 The limited of correlation coefficient on CFD simulation .....	138
7.5 Conclusion .....	138
CHAPTER 8 Conclusion .....	139

Research outcomes .....	141
Recommendations for future studies .....	142
REFERENCES.....	143
VITA .....	155



## LIST OF TABLES

	Page
Table 2.1 The pros and cons of simulation approaches .....	6
Table 3.1 Parameters for three interconnected fluidized bed reactors for chemical looping hydrogen production simulation .....	36
Table 3.2 Grid-independent study for three interconnected fluidized bed reactors for chemical looping hydrogen production simulation .....	36
Table 3.3 Grid-independent study for Internal circulating fluidized bed .....	39
Table 3.4 Simulation parameters of ICFB model .....	40
Table 3.5 The simulation parameters of the rotating drum .....	42
Table 3.6 Geometries and parameters for the base case numerical simulations .....	45
Table 3.7 Grid independency test studies .....	47
Table 3.8 Operating conditions for model validation .....	47
Table 3.9 The reference information .....	50
Table 3.10 Level of modeling parameters .....	51
Table 3.11 Simulation case in $2^k$ factorial experimental design .....	52
Table 3.12 Drop test experimental cases .....	55
Table 3.13 Drop test experimental results from reference literatures .....	56
Table 5.1 Simulation results of case B1 in $2^k$ factorial experimental design .....	85
Table 5.2 The results using B2 operating condition .....	86
Table 5.3 ANOVA analysis of translation kinetic energy .....	87
Table 5.4 ANOVA analysis of rotational kinetic energy .....	90
Table 5.5 ANOVA analysis of bed expansion ratio .....	95

Table 5.6 ANOVA analysis of the standard deviation of pressure drop .....	101
Table 6.1 Material properties and calculated effective elastic modulus.....	108
Table 6.2 The coefficient in the correlation of coefficient of restitution at each range of effective elastic modulus ( $E^*$ ).....	115
Table 6.3 The coefficient for temperature correction factor .....	116



## LIST OF FIGURES

	<b>Page</b>
Figure 2.1 The comparison of Eulerian and Lagrangian computational approaches .....	5
Figure 2.2 The contact model schematic with the contact force component .....	11
Figure 2.3 a) linear spring-dashpot contact model in the normal direction, and b) linear spring-dashpot contact model in the tangential direction .....	13
Figure 2.4 The user interface of MFIX open source code .....	15
Figure 2.5 Debugging the MFIX source code in Microsoft visual studio .....	15
Figure 2.6 The solver algorithm of CFD-DEM simulation of MFIX open-source code for DEM simulation using a constant coefficient of restitution .....	17
Figure 2.7 The solver algorithm of CFD-DEM simulation of MFIX open-source code for DEM simulation using dynamics coefficient of restitution .....	18
Figure 2.8 The collision phenomena at each coefficient of restitution .....	20
Figure 2.9 a) The collision schematic (Weir & Tallon, 2005) and b) the contact force loop during the contact (Horabik et al., 2017) .....	20
Figure 2.10 The kinetic energy distribution after contact .....	21
Figure 2.11 Coefficient of restitution as a function of impact velocity (Gilardi & Sharf, 2002).....	21
Figure 2.12 The procedure of traditional simulation with a constant coefficient of restitution .....	22
Figure 2.13 The scale metric effect of coefficient of restitution .....	23
Figure 3.1 The concept of three interconnected fluidized bed reactors for chemical looping hydrogen production.....	32

Figure 3.2 The geometry of the CLHP reactor with boundary conditions. (AR: air reactor; SR: steam reactor; FR: fuel reactor; LS: loop seal; MI: mass inflow boundary condition; PO: pressure outlet boundary condition) .....	34
Figure 3.3 Internal circulating fluidized bed geometry configuration.....	38
Figure 3.4 Rotating drum geometry .....	41
Figure 3.5 Schematic of the three-dimensional spouted bed reactor.....	44
Figure 3.6 The example of main effect and interaction effect .....	49
Figure 3.7 The procedure of $2^k$ factorial experimental design .....	49
Figure 3.8 Drop test apparatus where a) background, b) plate, c) plate holder, d) high speed camera, e) continuous light source, f) motorized releaser and g) heat gun with temperature controller .....	54
Figure 3.9 a) The algorithm of image analysis for particle tracking, b) grayscale to binary image conversion, c) image subtraction and d) particle tracking analysis .....	57
Figure 3.10 Free fall simulation .....	60
Figure 4.1 The solid volume fraction profile of AR with various grid sizes. (Solid inventory: 5 kg, where $V_{AR} = 170$ cm/s, $V_{SR} = 170$ cm/s, $V_{FR} = 50$ cm/s and $V_{LS} = 5$ cm/s) .....	62
Figure 4.2 The pressure profiles of cold flow model simulation for a) AR, b) SR and c) FR (solid inventory = 5 kg, $V_{AR} = 170$ cm/s, $V_{SR} = 170$ cm/s, $V_{FR} = 50$ cm/s and $V_{LS} = 5$ cm/s) .....	64
Figure 4.3 Void fraction snapshot of three interconnected fluidized bed reactors at difference coefficient of restitution (COR) a) COR 0.70, b) COR 0.85 and c) COR 0.99	66
Figure 4.4 Solid flux over simulation time at each coefficient of restitution.....	67
Figure 4.5 The average solid flux of each coefficient of restitution .....	67
Figure 4.6 The solid volume fraction profile of high velocity (HV) chamber with various grid sizes .....	68

Figure 4.7 The snapshot of glass bead in ICFB model with constant coefficient of restitution ( $e_n$ ) : a) $e_n = 0.8$ , b) $e_n = 0.9$ and c) $e_n = 0.99$ .....	70
Figure 4.8 The snapshot of polypropylene in ICFB model with constant coefficient of restitution ( $e_n$ ) : a) $e_n = 0.8$ , b) $e_n = 0.9$ and c) $e_n = 0.99$ .....	71
Figure 4.9 The solid flux of ICFB with difference solid materials: a) glass bead and b) polypropylene .....	72
Figure 4.10 The snapshot at 15 s of rotating drum simulation at difference rotating speed and coefficient of restitution approaches with a) 15 RPM and b) 35 RPM .....	74
Figure 4.11 The predicted power draw of rotating drum at each operating condition and coefficient of restitution approach with a) 15 RPM and b) 35 RPM .....	75
Figure 4.12 The solid volume fraction profile (EPs) along the axial direction with various grid sizes .....	76
Figure 4.13 Discrete solid particles movement at each coefficient of restitution condition .....	77
Figure 4.14 The comparison of average solid vertical velocity at each coefficient of restitution approach and experimental results a) $V_{sp} = 60$ m/s at 15 cm above the bottom, b) $V_{sp} = 60$ m/s at 25 cm above the bottom, c) $V_{sp} = 90$ m/s at 15 cm above the bottom and d) $V_{sp} = 90$ m/s at 25 cm above the bottom.....	78
Figure 5.1 a) The pressure drop of the spouted bed reactor for case B1 ( $V_{sp} = 60$ m/s) and b) the pressure drop of spouted bed reactor for case B2 ( $V_{sp} = 90$ m/s).....	81
Figure 5.2 Simulation and experimental time-averaging of the lateral vertical particle velocity profile on the central xy-plane at different heights: a) $V_{sp} = 60$ m/s, $y = 0.15$ m; b) $V_{sp} = 60$ m/s, $y = 0.25$ m; c) $V_{sp} = 90$ m/s, $y = 0.15$ m; and d) $V_{sp} = 90$ m/s, $y = 0.25$ m .....	82
Figure 5.3 Instantaneous contour plots of void fraction on the central xy-plane of the spouted bed reactor of a) $V_{sp} = 60$ m/s and b) $V_{sp} = 90$ m/s.....	83



Figure 5.4 The instantaneous particle patterns in the spouted bed reactor of a) $V_{sp} = 60$ m/s and b) $V_{sp} = 90$ m/s .....	84
Figure 5.5 The main effect plot of translational kinetic energy .....	88
Figure 5.6 The interaction effect plot of the translational kinetic energy of a) AB, b) AD and c) BD .....	88
Figure 5.7 The main effect plot of rotational kinetic energy.....	91
Figure 5.8 The interaction effect plot of the rotational kinetic energy of a) AB, b) AC, c) AD, d) AE, e) BD, f) CD, g) CE and h) DE .....	92
Figure 5.9 The main effect plot of bed expansion ratio .....	96
Figure 5.10 The interaction effect plot of the bed expansion ratio of a) AB, b) AC, c) AD, d) BC and e) BD .....	97
Figure 5.11 The average solid volume fraction classification for a) Group A, b) Group B .....	98
Figure 5.12 The average solid volume fraction classification for a) Group A, b) Group B and c) the contour plots of the averaged void fraction on the central XY-plane of the spouted bed reactor for the base case B1, Group A (case 23), and Group B (case 27)99	
Figure 5.13 The main effect plot of the standard deviation of pressure drop.....	102
Figure 5.14 The interaction effect plot of the standard deviation of $P_{drop}$ of a) AB, b) AC, c) AD, d) BC, e) BD, f) CD and g) DE.....	103
Figure 6.1 The sizing independent of coefficient of restitution for the contact between glass bead and acrylic plate.....	105
Figure 6.2 The sizing independent of the coefficient of restitution for the collision between polypropylene and acrylic plate.....	106
Figure 6.3 The effect of impact velocity on the coefficient of restitution at difference effective elastic modulus ( $E^*$ ).....	107

Figure 6.4 The effect of temperature on coefficient of restitution at difference impact velocity of the collision between glass bead and steel plate, a) $V_{imp} = 1.4$ m/s, b) $V_{imp} = 2.4$ m/s, c) $V_{imp} = 3.1$ m/s, d) $V_{imp} = 3.7$ m/s, e) $V_{imp} = 4.2$ m/s, f) $V_{imp} = 4.6$ m/s, g) $V_{imp} = 5.0$ m/s and h) $V_{imp} = 5.4$ m/s .....	111
Figure 6.5 The effect of temperature on coefficient of restitution at difference impact velocity of the collision between polypropylene and steel plate, a) $V_{imp} = 1.4$ m/s, b) $V_{imp} = 2.4$ m/s, c) $V_{imp} = 3.1$ m/s, d) $V_{imp} = 3.7$ m/s, e) $V_{imp} = 4.2$ m/s, f) $V_{imp} = 4.6$ m/s, g) $V_{imp} = 5.0$ m/s and h) $V_{imp} = 5.4$ m/s .....	112
Figure 6.6 The comparison of predicted coefficient of restitution with the existing model of the collision between glass bead and steel plate at difference impact velocity and temperature .....	117
Figure 6.7 The comparison of predicted coefficient of restitution with the existing model of the collision between polypropylene and steel plate at difference impact velocity and temperature .....	118
Figure 6.8 The comparison between drop test from experiment and simulation.....	120
Figure 6.9 The comparison of predicted rebound height at each coefficient of restitution a) the collision of the glass bead and acrylic plate at room temperature and b) the collision of polypropylene and acrylic plate at room temperature .....	121
Figure 6.10 The predicted free fall height at difference impact velocity and temperature of the collision between glass bead and steel plate a) Room temperature, b) 100 °C, c) 170 °C, d) 240 °C and e) 310 °C .....	122
Figure 6.11 The predicted free fall height at different impact velocity and temperature of the collision between polypropylene and steel plate a) Room temperature, b) 60 °C, c) 90 °C, d) 120 °C and e) 150 °C .....	123
Figure 7.1 The snapshots of glass bead in ICFB model with constant coefficient of restitution ( $e_n$ ) : a) $e_n = 0.8$ , b) $e_n = 0.9$ and c) $e_n = 0.99$ .....	127

Figure 7.2 The snapshots of glass bead in ICFB model with dynamics coefficient of restitution ( $e_n$ ) at each operating temperature : a) 298 K, b) 600 K and c) 900 K .....	128
Figure 7.3 The solid flux of ICFB with glass bead at coefficient of restitution approach .....	129
Figure 7.4 The snapshots of polypropylene in ICFB model with constant coefficient of restitution ( $e_n$ ) : a) $e_n = 0.8$ , b) $e_n = 0.9$ and c) $e_n = 0.99$ .....	130
Figure 7.5 The snapshots of polypropylene in ICFB model with dynamics coefficient of restitution ( $e_n$ ) at each operating temperature : a) 298 K, b) 350 K and c) 400 K .....	131
Figure 7.6 The solid flux of ICFB with polypropylene at coefficient of restitution approach .....	132
Figure 7.7 The snapshots at 15 s of rotating drum simulation at different rotating speed and coefficient of restitution approaches: a) 15 RPM and b) 35 RPM .....	133
Figure 7.8 The predicted power draw of rotating drum at each operating condition and coefficient of restitution approaches: a) 15 RPM and b) 35 RPM .....	134
Figure 7.9 Discrete solid particles movement at each coefficient of restitution condition .....	135
Figure 7.10 The pressure drop fluctuation of spouted bed reactor at $V_{sp} = 90$ m/s.....	136
Figure 7.11 The comparison of average solid vertical velocity at each coefficient of restitution approach and experimental results a) $V_{sp} = 60$ m/s at 15 cm above the bottom, b) $V_{sp} = 60$ m/s at 25 cm above the bottom, c) $V_{sp} = 90$ m/s at 15 cm above the bottom and d) $V_{sp} = 90$ m/s at 25 cm above the bottom.....	137

## Chapter 1

### Introduction

#### 1.1 Background

Fluidization is a process in which the movement of solid behaves like the fluid. Its ability enhances the efficiency of mass and heat transfers between the fluid phase and the solid phase. It is widely used in various fields such as petroleum, petrochemical, food industries, pharmaceutical and energy production. The performance of the fluidization unit is depended on its design and operating conditions. In the past, the fluidization has been designed and improved under the real experiment. However, it consumes high operation costs and time because it requires many equipment and measurement depending on the number of interesting points. Recently, the design of the fluidization unit using computational fluid dynamics (CFD) simulation is received attention. The complex partial differential equations such as heat transfer, mass transfer and momentum transfer are solved by numerical methods that have been handled by the computational unit. The advantages of using CFD simulation are time-saving, cost-effectiveness, and safe environment. The simulation can also apply to predict the phenomena of the system under severe conditions and the results can show the behaviour of solid inside the fluidized bed system via graphical results and numeric data. However, it requires some specific modelling parameters in the model.

The coefficient of restitution is the parameter that affects the dissipation energy when collisions occur in the reactor. The definition of the coefficient of restitution is the ratio of kinetic energy before the collision and kinetic energy after the collision. The numeric values of the coefficient of restitution are varying between 0 and 1. The coefficient of restitution equals to 1 represents the perfectly elastic collision which no kinetic energy loss. In case that the coefficient of restitution is equalled to 0, the solid object is performed as the perfectly inelastic collision. The kinetic energy is fully converted to heat dissipation and permanent deformation. There are several research studies about the coefficient of restitution. Most of the research studied the effect of typical parameters such as density, Poisson's ratio, sizing, sphericity, and impact velocity on the coefficient of restitution.

However, the previous studies were conducted at room temperature. In reality, the fluidized bed reactor is operated at high temperature such as in combustion, drying and coating processes. The ability to remain the kinetic energy of solid objects might be changed depending on the operating condition. This is because the properties of the material significantly change when the temperature is changed. The simulation that uses the constant coefficient of restitution thus cannot represent the actual hydrodynamics behaviour for the fluidized bed system. Thus, the effect of the coefficient of restitution on simulation results is needed to take into consideration. The changing in the coefficient of restitution influences the homogeneity and forming of the bubble. If the ability to contain the kinetic energy is decreased, the bubble can grow up beside the particle easily due to the pressure difference between the voids around the solid particles. In this study, the effect of fundamental properties of solid materials, impact velocity and temperature on the coefficient of restitution are investigated. Afterwards, the new correlation is proposed from the experimental result. The coefficient of restitution result is simplified to correlate in terms of impact velocity, granular temperature, elastic modulus, Poisson's ratio, solid diameter, and temperature. The correlation of dynamics coefficient of restitution is then synchronized with the computational fluid dynamics. The traditional simulation with constant coefficient of restitution is compared with the novel simulation approach with correlation of dynamics coefficient of restitution. Using the dynamics coefficient of restitution will have the ability to get more accurate in simulation and serve as a baseline for further use of the coefficient of restitution in the other process systems.

## 1.2 Objectives

1. Study the effect of operating parameters on solid coefficient of restitution by experiment.
2. Develop the correlation of solid coefficient of restitution.
3. Study the effect of solid coefficient of restitutions on the hydrodynamics in the fluidized bed system by computational fluid dynamics simulation.
4. Compare the traditional CFD simulation results with the dynamics coefficient of restitution and the conventional CFD simulation with constant coefficient of restitution.

## 1.3 Scope of the dissertation

1. The coefficient of restitution is studied in the elastic regime only which neglects the permanent deformation after the collision.
2. The solid particle with adhesive, cohesive and electrostatic are neglected in this study.
3. The effects of the contact parameters in computational fluid dynamics simulation are investigated by statistical technique.
4. The novel approach of computational fluid dynamics simulation with the dynamics coefficient of restitution is compared with the traditional simulation using a constant coefficient of restitution.

## Chapter 2

### Theory and literature review

#### 2.1 Computational fluid dynamics simulation

Computational fluid dynamics (CFD) is a numerical approach for solving the multiphase flow problem. The powerful of CFD simulation can propose the quantitative and precise predictions of the multiphase flow phenomena. It implements the detail and information in which the experiment cannot obtain. The CFD simulation consists of two approaches. There are the Eulerian-Eulerian approach and the Lagrangian-Eulerian approach, as shown in Figure 2.1. In the Eulerian-Eulerian approach, the fluid and solid phases are treated as the continuum phase. It incorporates with the kinetic theory of granular flow (KTGF) to predict the hydrodynamics of solid phases (J. Ding & Gidaspow, 1990). It computes the hydrodynamics profile or flow field of both phases in the specific control element or volume in which the flow field is time-dependent. The CFD simulation with Eulerian-Eulerian approach is typically called the two-fluid model (TFM) simulation which firstly proposed by Tommeijer (1952). TFM simulation usually applies to the fluid-solid model in which the solid particles are enough to assume as the continuum phase. Besides, the Eulerian-Lagrangian approach treats multiphase flow separately. The fluid phase is solved as the continuum phase like the Eulerian-Eulerian approach. The hydrodynamics profile is computed in the specific control element or volume. The solid phase is treated as the discrete individual particle based on Newton's laws of motion. The contact model handles the collision between solid particles as the constitutive equations. The CFD simulation using the Eulerian-Lagrangian approach is called discrete element model (DEM) simulation which was introduced by Cundall and Strack (1979). The strengths and weaknesses of each approach are summarized in Table 2.1.

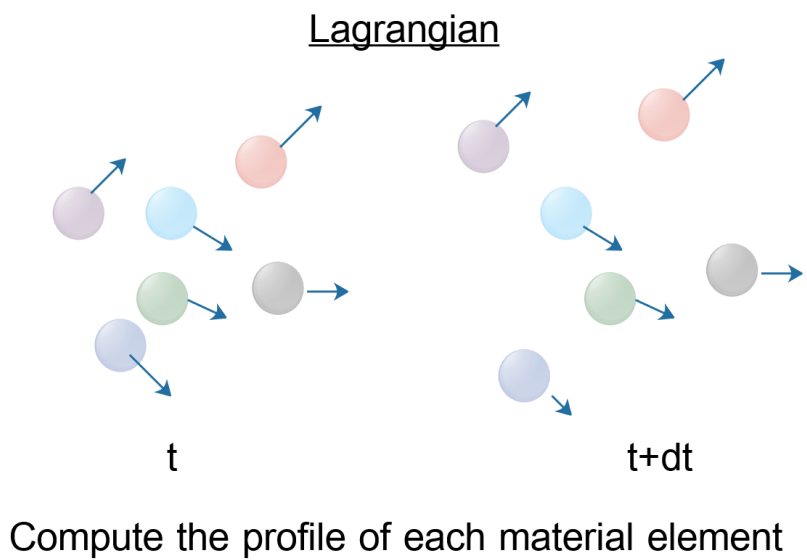
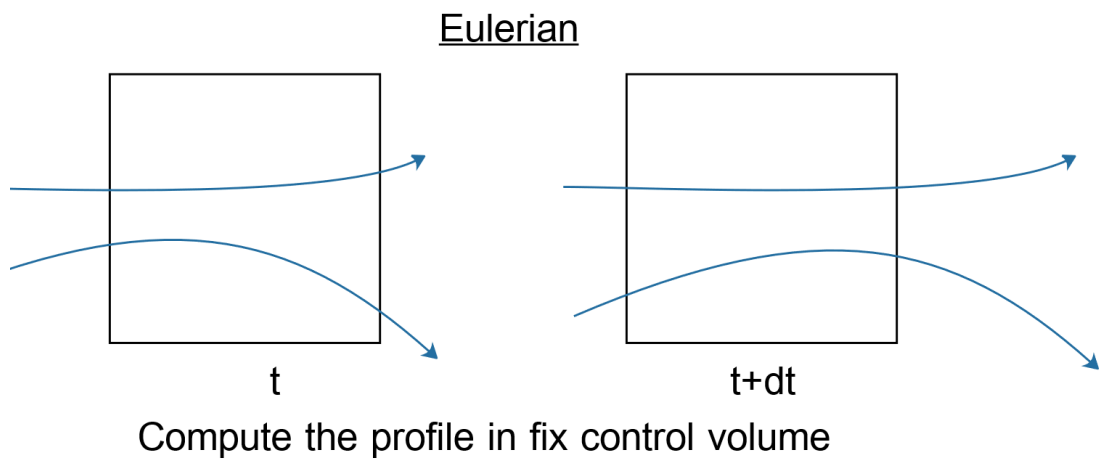


Figure 2.1 The comparison of Eulerian and Lagrangian computational approaches



Table 2.1 The pros and cons of simulation approaches

Method	Strengths	Weaknesses
TFM (Eulerian-Eulerian)	<ul style="list-style-type: none"> <li>- Require low computation resource</li> <li>- Prefer for the dense system which solid phase can be assumed to the continuous phase</li> </ul>	<ul style="list-style-type: none"> <li>- Defer for the large diameter of solid due to lack of the accuracy</li> <li>- Consist of many constitutive equations</li> <li>- Lack of knowledge in the polydispersion model</li> <li>- Consist of many constitutive equations</li> </ul>
DEM (Eulerian-Lagrangian)	<ul style="list-style-type: none"> <li>- Store the profile such as position, velocity, force and temperature of solid particle individually</li> <li>- Obtain realistic collision between the solid phase</li> <li>- Can simulate the irregular shape particle</li> </ul>	<ul style="list-style-type: none"> <li>- Consume high computation resource for many solid particles</li> <li>- Lack of knowledge in the physical properties of solid</li> </ul>

### 2.1.1 TFM simulation

The TFM has been widely used to simulate the multiphase flow of the gas-solid fluidization system. The method is commonly used for the system employing more than one phases. It requires less computational resource than the DEM simulation. However, the disadvantage of TFM simulation treats the solid phase by averaging procedure to the entire flow domain instead of individual particle. The governing equations are illustrated below.

- The continuity equation

The continuity equation represents the changing of mass which equals to the difference between flows entering and leaving from the control volume. The continuity equations can be expressed below.

- Continuity equation for gas phase g

$$\frac{\partial}{\partial t}(\varepsilon_g \rho_g) + \frac{\partial}{\partial x_i}(\varepsilon_g \rho_g U_{gi}) = \sum_{n=1}^{N_g} R_{gn} \quad (1)$$

- Continuity equations for solids phases m=1, M

$$\frac{\partial}{\partial t}(\varepsilon_m \rho_m) + \frac{\partial}{\partial x_i}(\varepsilon_m \rho_m U_{mi}) = \sum_{n=1}^{N_m} R_{mn} \quad (2)$$

#### 2.1.1.1 The momentum equations

Newton's laws of motion perform motion analysis. According to Newton's 2<sup>nd</sup> Law, the rate of change of momentum is the proportion of the resultant force acting on the body or element in which results in the same direction of the force. In fluid dynamics, the conservation of momentum can be written in the derivative form below.

- Momentum equations for gas phase g:

$$\left[ \frac{\partial}{\partial t}(\varepsilon_g \rho_g U_{gi}) + \frac{\partial}{\partial x_j}(\varepsilon_g \rho_g U_{gj} U_{gi}) \right] = -\varepsilon_g \frac{\partial P_g}{\partial x_i} + \frac{\partial \tau_{gij}}{\partial x_j} - \sum_{m=1}^M I_{gmi} + f_{gi} + \varepsilon_g \rho_g g_i \quad (3)$$

- Momentum equations for solids phases m = 1, M

$$\left[ \frac{\partial}{\partial t}(\varepsilon_m \rho_m U_{mi}) + \frac{\partial}{\partial x_j}(\varepsilon_m \rho_m U_{mj} U_{mi}) \right] = -\varepsilon_m \frac{\partial P_g}{\partial x_i} + \frac{\partial \tau_{mij}}{\partial x_j} + I_{gmi} - \sum_{k=1}^M I_{kmi} + \varepsilon_m \rho_m g_i \quad (4)$$

### 2.1.1.2 The kinetic theory of granular flow

The kinetic theory of granular flow (KTGF) is usually employed in TFM model for treating the solid phase. The KTGF is based on the statistical average of the kinetic energy from solid fluctuation. The expression is shown below.

- Granular temperature equations for solids phases  $m = 1, M$

$$\frac{3}{2} \rho_m \left[ \frac{\partial \varepsilon_m \Theta_m}{\partial t} + \frac{\partial \varepsilon_m U_{mj} \Theta_m}{\partial x_j} \right] = \frac{\partial}{\partial x_i} \left( \kappa_m \frac{\partial \Theta_m}{\partial x_i} \right) + \tau_{mij} \frac{\partial U_{mi}}{\partial x_j} + \Pi_m - \varepsilon_m \rho_m J_m \quad (5)$$

- Solid stresses

$$\tau_{mij} = \left( -P_m + \eta \mu_b \frac{\partial U_{mi}}{\partial x_i} \right) \delta_{ij} + 2 \mu_m S_{mij} \quad (6)$$

Where

$$S_{mij} = \frac{1}{2} \left( \frac{\partial U_{mi}}{\partial x_j} + \frac{\partial U_{mj}}{\partial x_i} \right) - \frac{1}{3} \frac{\partial U_{mi}}{\partial x_i} \quad (7)$$

- Solid pressure

$$P_m = \varepsilon_m \rho_m \Theta_m \left[ 1 + 4\eta \sum_{n=1}^M (\varepsilon_n g_{0,mn}) \right] \quad (8)$$

- Solid viscosity

$$\mu_m = \left( \frac{2+\alpha}{3} \right) \left[ \frac{\mu_m^*}{g_{0,mn} \eta (2-\eta) \left( 1 + \frac{8}{5} \eta \sum_{n=1}^M (\varepsilon_n g_{0,mn}) \right) \left( 1 + \frac{8}{5} \eta (3\eta-2) \sum_{n=1}^M (\varepsilon_n g_{0,mn}) \right)} + \frac{3}{5} \eta \mu_b \right] \quad (9)$$

$$\mu_m^* = \frac{\rho_m \varepsilon_m g_{0,mn} \Theta_m \mu}{\rho_m \sum_{n=1}^M (\varepsilon_n g_{0,mn}) \Theta_m + \left( \frac{2\beta\mu}{\rho_m \varepsilon_m} \right)} \quad (10)$$

$$\mu = \frac{5}{96} \rho_m d_p \sqrt{\pi \Theta_m} \quad (11)$$

$$\mu_b = \frac{256}{5\pi} \mu \varepsilon_m \sum_{n=1}^M (\varepsilon_n g_{0,mn}) \quad (12)$$

- Solid conductivity

$$\kappa_m = \left( \frac{\kappa_m^*}{g_{0,mn}} \right) \left[ \left( 1 + 12\eta \sum_{n=1}^M (\varepsilon_n g_{0,mn}) \right) \left( 1 + \frac{12}{5} \eta^2 (4\eta-3) \sum_{n=1}^M (\varepsilon_n g_{0,mn}) \right) + \frac{64}{25\pi} (41-33\eta) \eta^2 \left( \sum_{n=1}^M (\varepsilon_n g_{0,mn}) \right)^2 \right] \quad (13)$$

$$\kappa_m^* = \frac{\rho_m \varepsilon_m g_{0,mm} \Theta_m \kappa}{\rho_m \sum_{n=1}^M (\varepsilon_n g_{0,mn}) \Theta_m + \left( \frac{6\beta\kappa}{5\rho_m \varepsilon_m} \right)} \quad (14)$$

$$\kappa = \frac{75\rho_m d_p \sqrt{\pi\Theta_m}}{48\eta(41-33\eta)} \quad (15)$$

- Collisional dissipation

$$J_m = \frac{48}{\sqrt{\pi}} \eta(1-\eta) \frac{\sum_{n=1}^M (\varepsilon_n g_{0,mn})}{d_p} \Theta_m^{3/2} \quad (16)$$

$$\eta = \frac{1+e}{2} \quad (17)$$

- Exchange terms

$$\Pi_m = -3\beta\Theta_s + \frac{81\varepsilon_m \mu_g^2 |u_g - u_m|^2}{g_{0,mm} d_p^3 \rho_m \sqrt{\pi\Theta_m}} \quad (18)$$

### 2.1.1.3 Momentum interphase transfer

The interphase momentum exchange between gas and solid phase is commonly known namely “drag force”. The interphase momentum exchange between gas and solid can be written below.

- Gas-solids momentum interphase exchange

$$I_{gmi} = \beta_{gm} (u_{gi} - u_{mi}) \quad (19)$$

The drag coefficient ( $\beta_{gm}$ ) can be expressed by the correlation which developed from the experiment. In this study, drag correlations are summarized below.

- Reynolds number

$$\text{Re} = \frac{\rho_g \varepsilon_g d_{pm} |u_g - u_m|}{\mu_g} \quad (20)$$

- Wen-Yu drag correlation

$$\beta_{gm} = \frac{3\rho_g \varepsilon_g \varepsilon_m C_D |u_g - u_m| \varepsilon_g^{-2.65}}{4d_{pm}} \quad (21)$$

$$C_D = \begin{cases} \frac{24}{\text{Re}(1+0.15\text{Re}^{0.687})} & \text{Re} < 1000 \\ 0.44 & \text{Re} \geq 1000 \end{cases} \quad (22)$$

- Gidaspow drag correlation

$$\beta_{gm} = \begin{cases} \frac{3\rho_g \varepsilon_g \varepsilon_m C_D |u_g - u_m| \varepsilon_g^{-2.65}}{4d_{pm}} & \varepsilon_g \geq 0.8 \\ \frac{150\varepsilon_s(1-\varepsilon_g)\mu_g}{\varepsilon_g d_{pm}^2} + \frac{1.75\rho_g \varepsilon_m |u_g - u_m|}{d_{pm}} & \varepsilon_g < 0.8 \end{cases} \quad (23)$$

$$C_D = \begin{cases} \frac{24}{\text{Re}(1+0.15\text{Re}^{0.687})} & \text{Re} < 1000 \\ 0.44 & \text{Re} \geq 1000 \end{cases} \quad (24)$$

- Syamlal O'brien drag model

$$\beta_{gm} = \frac{3\rho_g \varepsilon_g \varepsilon_m}{4V_{rm}^2 d_{pm}} \left( 0.63 + 4.8 \sqrt{\frac{V_{rm}}{\text{Re}_m}} \right)^2 |u_g - u_m| \quad (25)$$

$$V_{rm} = 0.5 \left( A - 0.06\text{Re}_m + \sqrt{(0.06\text{Re}_m)^2 + 0.12\text{Re}_m(2B - A) + A^2} \right) \quad (26)$$

$$A = \varepsilon_g^{4.14} \quad (27)$$

$$B = \begin{cases} 0.8\varepsilon_g^{1.28} & \varepsilon_g \leq 0.85 \\ \varepsilon_g^{2.65} & \varepsilon_g > 0.85 \end{cases} \quad (28)$$

$$\text{Re}_m = \frac{\rho_g d_{pm} |u_g - u_m|}{\mu_g} \quad (29)$$

- Beetstra-Van der Hoef-Kuipers (BVK)

$$\beta_{gm} = \frac{18\mu\varepsilon_g(1-\varepsilon_g)F_{BVK}}{d_{pm}^2} \quad (30)$$

$$F_{BVK} = \frac{10(1-\varepsilon_g)}{\varepsilon_g^2} + \varepsilon_g^2(1+1.5\sqrt{1-\varepsilon_g}) + \frac{0.413\text{Re} \left[ \frac{\varepsilon_g^{-1} + 3\varepsilon_g(1-\varepsilon_g) + 8.4\text{Re}^{-0.343}}{1+10^{3(1-\varepsilon_g)}} \text{Re}^{-0.5-2(1-\varepsilon_g)} \right]}{24\varepsilon_g^2} \quad (31)$$

$$C_D = \begin{cases} \frac{24}{\text{Re}(1+0.15\text{Re}^{0.687})} \\ 0.44 \end{cases} \quad (32)$$

## 2.2 DEM simulation

This approach has been received attention to investigate the fluid-particle interaction systems. The KTGF from TFM is replaced by the conservation of momentum corresponding to Newton's laws of motion of an individual particle. The force vector is the multiplication of mass and acceleration as shown in Equation 33.

The set of equations of solid-phase are illustrated below.

$$\vec{F}_{T,i} = m_i \vec{a}_i = m_i \frac{d\vec{V}_i}{dt} = m \frac{d^2 \vec{X}_i}{dt^2} \quad (33)$$

$$\vec{F}_{T,i} = \vec{W}_i + \vec{F}_D + \vec{F}_{C,ij} \quad (34)$$

$$\vec{T}_i = \vec{F}_{t,ij} \times \vec{r}_i = I_i \frac{d\vec{\omega}_i}{dt} \quad (35)$$

### 2.2.1 Contact model

Contact schematic between solid particle is shown in Figure 2.2. The collision between solid particle  $i^{\text{th}}$  and  $j^{\text{th}}$  particle is assumed to be the partial elastic collision. The shape of the solid sphere can be changed during contact and return to the original shape.  $\vec{\delta}_n$  and  $\vec{\delta}_t$  represents the normal and tangential overlap displacements, respectively. The general motion parameters are demonstrated below.

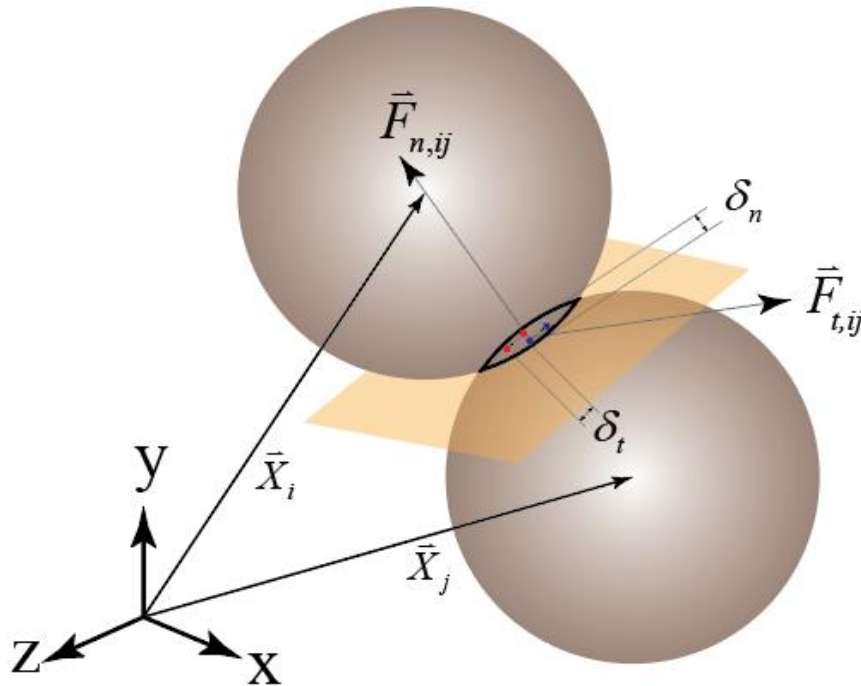


Figure 2.2 The contact model schematic with the contact force component

- Normal overlap displacement

$$\vec{\delta}_n = (0.5(D_i + D_j) - |\vec{X}_i - \vec{X}_j|)\vec{\eta}_{ij} \quad (36)$$

- Unit vector of contact direction

$$\vec{\eta}_{ij} = \frac{\vec{X}_j - \vec{X}_i}{|\vec{X}_j - \vec{X}_i|} \quad (37)$$

- Relative velocity between  $i^{\text{th}}$  and  $j^{\text{th}}$  solid particles

$$\vec{V}_{ij} = \vec{V}_i - \vec{V}_j + (L_i\vec{\omega}_i + L_j\vec{\omega}_j) \times \vec{\eta}_{ij} \quad (38)$$

- The distance between the center of solid spherical to contact plane of  $i^{\text{th}}$  particle

$$L_i = \frac{|\vec{X}_j - \vec{X}_i|^2 + (r_i^2 - r_j^2)}{2|\vec{X}_j - \vec{X}_i|} \quad (39)$$

- The distance between the center of solid spherical to contact plane of  $j^{\text{th}}$  particle

$$L_j = |\vec{X}_j - \vec{X}_i| - L_i \quad (40)$$

- Relative velocity between  $i^{\text{th}}$  and  $j^{\text{th}}$  solid particles in normal direction

$$\vec{V}_{n,ij} = \vec{\eta}_{ij} \cdot \vec{V}_{ij} \vec{\eta}_{ij} \quad (41)$$

- Relative velocity between  $i^{\text{th}}$  and  $j^{\text{th}}$  solid particles in tangential direction

$$\vec{V}_{t,ij} = \vec{V}_{ij} - \vec{V}_{n,ij} \quad (42)$$

- Tangential contact direction

$$\vec{t}_{ij} = \frac{\vec{V}_{ij} - \vec{V}_{n,ij}}{|\vec{V}_{ij} - \vec{V}_{n,ij}|} \quad (43)$$

Contact force ( $\vec{F}_{C,ij}$ ) is a force that defines at contact point during the collision between solid particle. It is developed to describe the contact behaviour which governed by Newton's Laws of motion. The contact force is divided into two direction such as normal direction and tangential direction. The contact force equation is shown below.

- Total Contact force

$$\vec{F}_{C,ij} = \vec{F}_{n,ij} + \vec{F}_{t,ij} \quad (44)$$

The linear spring-dashpot (LSD) model was proposed by Cundall and Strack (1979). It is usually used to describe contact phenomena. In the computational, the solid particle has remained geometrically rigid in which the deformation is taken account. It is the principal of the contact model. It is famous for DEM simulation due to simplicity and

efficiency. In the model, spring is represented the elastic part and a dashpot is employed the dissipative mechanism as shown in Figure 2.3.

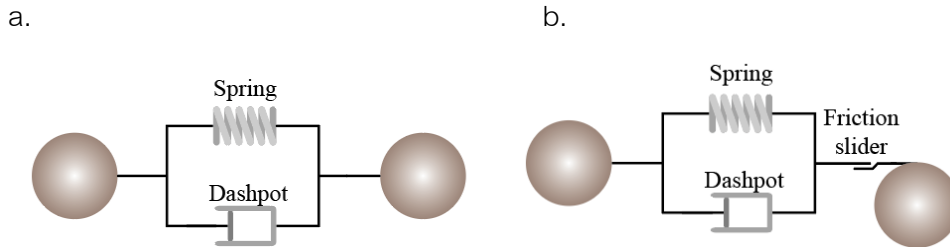


Figure 2.3 a) linear spring-dashpot contact model in the normal direction, and b) linear spring-dashpot contact model in the tangential direction

The normal contact direction and tangential contact direction are analogous in Figure 2.3a and Figure 2.3b, respectively. The normal contact force is acted at the surface of the contact point. The direction of the normal contact force is calculated by the difference between the center of mass of the  $i^{\text{th}}$  particle and the  $j^{\text{th}}$  particle as shown in Figure 2.2.

- LSD contact in normal direction

$$\vec{F}_{n,ij} = \vec{F}_{n,ij}^S + \vec{F}_{n,ij}^D \quad (45)$$

$$\vec{F}_{n,ij}^S = -k_n \vec{\delta}_n \quad (46)$$

$$\vec{F}_{n,ij}^D = -\eta_n \vec{V}_{n,ij} \quad (47)$$

- Dissipation or damping coefficient in normal direction

$$\eta_n = \frac{2 \ln e_n \sqrt{m_{\text{eff}} k_n}}{\sqrt{\pi^2 + \ln^2 e_n}} \quad (48)$$

- The effective mass

$$\frac{1}{m_{\text{eff}}} = \frac{1}{m_i} + \frac{1}{m_j} \quad (49)$$

- LSD contact in normal tangential direction

$$\vec{F}_{t,ij} = \vec{F}_{t,ij}^S + \vec{F}_{t,ij}^D \quad (50)$$

$$\vec{F}_{t,ij}^S = -k_t \vec{\delta}_t \quad (51)$$

$$\vec{F}_{t,ij}^D = -\eta_t \vec{V}_{t,ij} \quad (52)$$



- Dissipation or damping coefficient in tangential direction

$$\eta_t = \frac{2ln e_t \sqrt{m_{\text{eff}} k_t}}{\sqrt{\pi^2 + ln^2 e_t}} \quad (53)$$

$$\bar{\delta}_t = \bar{V}_{t,ij} \min \left( \frac{|\delta_n|}{|\bar{V}_{n,ij}|}, \Delta t \right) \quad (54)$$

$$\bar{\delta}_{t+\Delta t} = \bar{\delta}_t + \bar{V}_{t,ij} \Delta t \quad (55)$$

According to the Coulomb friction law, the tangential contact force equals the product of the friction coefficient and the normal contact force if the tangential contact force is over than that product. It is expressed as follows:

$$\vec{F}_{t,ij} = -\mu \left| \vec{F}_{n,ij} \right| \vec{t}_{ij} \quad \text{if } \left| \vec{F}_{t,ij} \right| > \mu \left| \vec{F}_{n,ij} \right| \quad (56)$$

### 2.3 MFIX open source code

Multiphase Flow with Interphase eXchanges open source code or “MFIX” is used to conduct the simulation in this study. MFIX has been developing by National Energy Technology Laboratory (NETL) since 1991. It is received attention tool to model fluidized bed reactor such as gasifier, cyclone, circulating fluidized bed and rotating drum etc. The code is developed on Fortran computer language which suitable for applying the case in the cluster, high-performance computer (HPC) and supercomputer. Due to the general-purpose of Fortran, it is a powerful programming language to compute the numeric computation and scientific calculation. The advantage of MFIX is that users can be easily changed the code with the developer. The flexibility to compute and develop are obtained. However, MFIX still has limitation for the case with complex geometry. The theory, simulation technique, code architecture, and user’s manual has published on the website of NETL “<https://mfix.netl.doe.gov/>”. The user interface (UI) of MFIX is shown in Figure 2.4. The code is promptly edited and developed via Microsoft visual studio as shown in Figure 2.5.

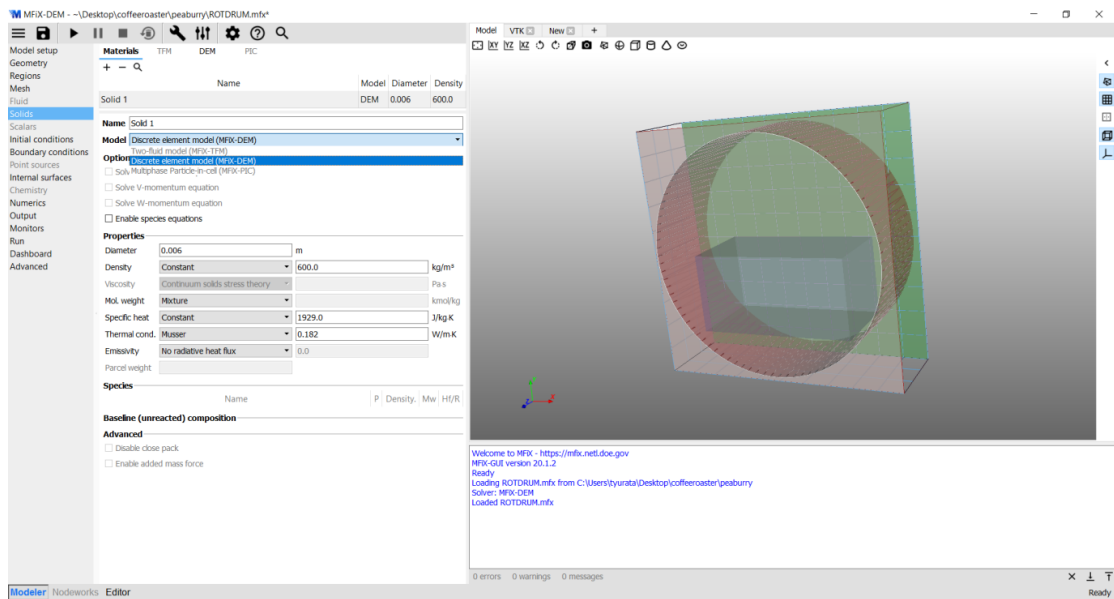


Figure 2.4 The user interface of MFX open source code

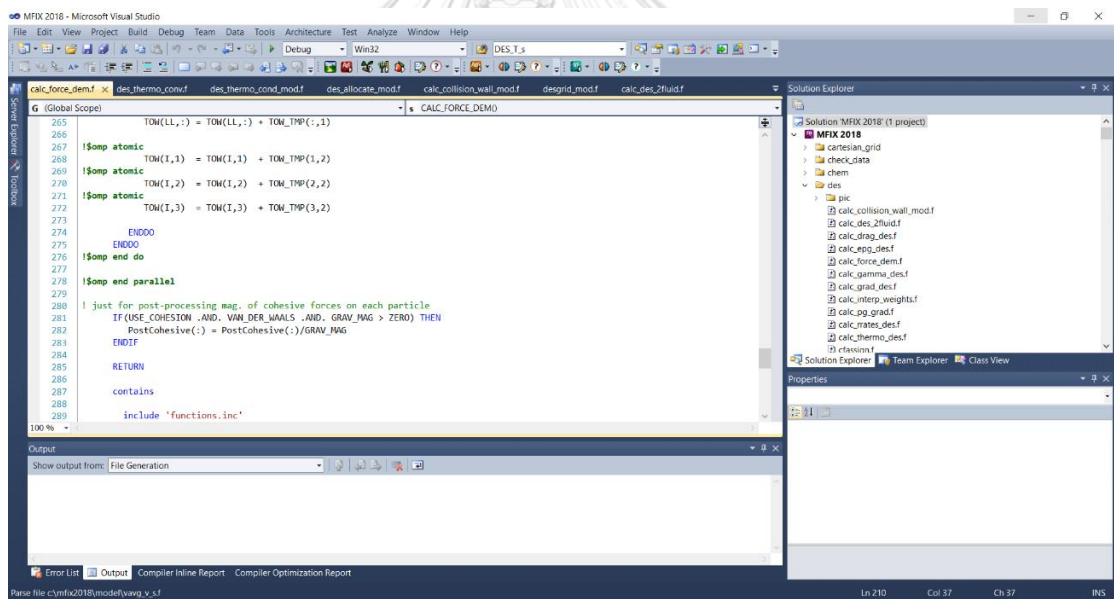


Figure 2.5 Debugging the MFX source code in Microsoft visual studio

The traditional algorithm to solve the CFD problem in MFIX consists of 2 sections. There are CFD solver section and DEM solver section as shown in Figure 2.6. The CFD solver is the first section which solves the problem in the fix control volume by Eulerian approach. It applies for single fluid phase computational and TFM simulation. Besides, the DEM simulation has an advanced section which solves the continuum phase of the fluid couple with the discrete phase of solid.

The first step of MFIX calculation is the computing the profile of fluid phases such as fluid velocity, pressure, temperature, etc. until the simulation time reaching to the defining time step. After that, the fluid profiles are replaced into the interphases exchange term which bases on 3<sup>rd</sup> laws of Newton. The DEM solver solves the discrete phase at the initially simulation time as same as the initially time in CFD solver. The solid phases are solved as individual particles. The contact force, the momentum exchange and other solid profile are solved by iterating the solid particles at different time step from CFD solver. The contact force is employed only while the collision between solid particles is happened by particle neighbour search algorithm. The neighbour search algorithm is the approach that MFIX used to search the collision. The time step in DEM simulation is typically smaller than the time in CFD simulation about 10-50 times. The DEM solver loop is ended when the simulation in DEM solver is equalled to the simulation time in CFD solver. After that, the predicted DEM parameters are replaced in the interphase exchange term transferring to the CFD solver at the next time step. Thus, this is the reasons why DEM simulation is taken more computational resource.

For the development of DEM simulation with the dynamics coefficient of restitution, the contact force modules are modified. The coefficient of restitution is changed by the correlation after checking the collision by neighbour searching. After that, the contact force is calculated with the local coefficient of restitution. The overall flow chart is shown in Figure 2.7.

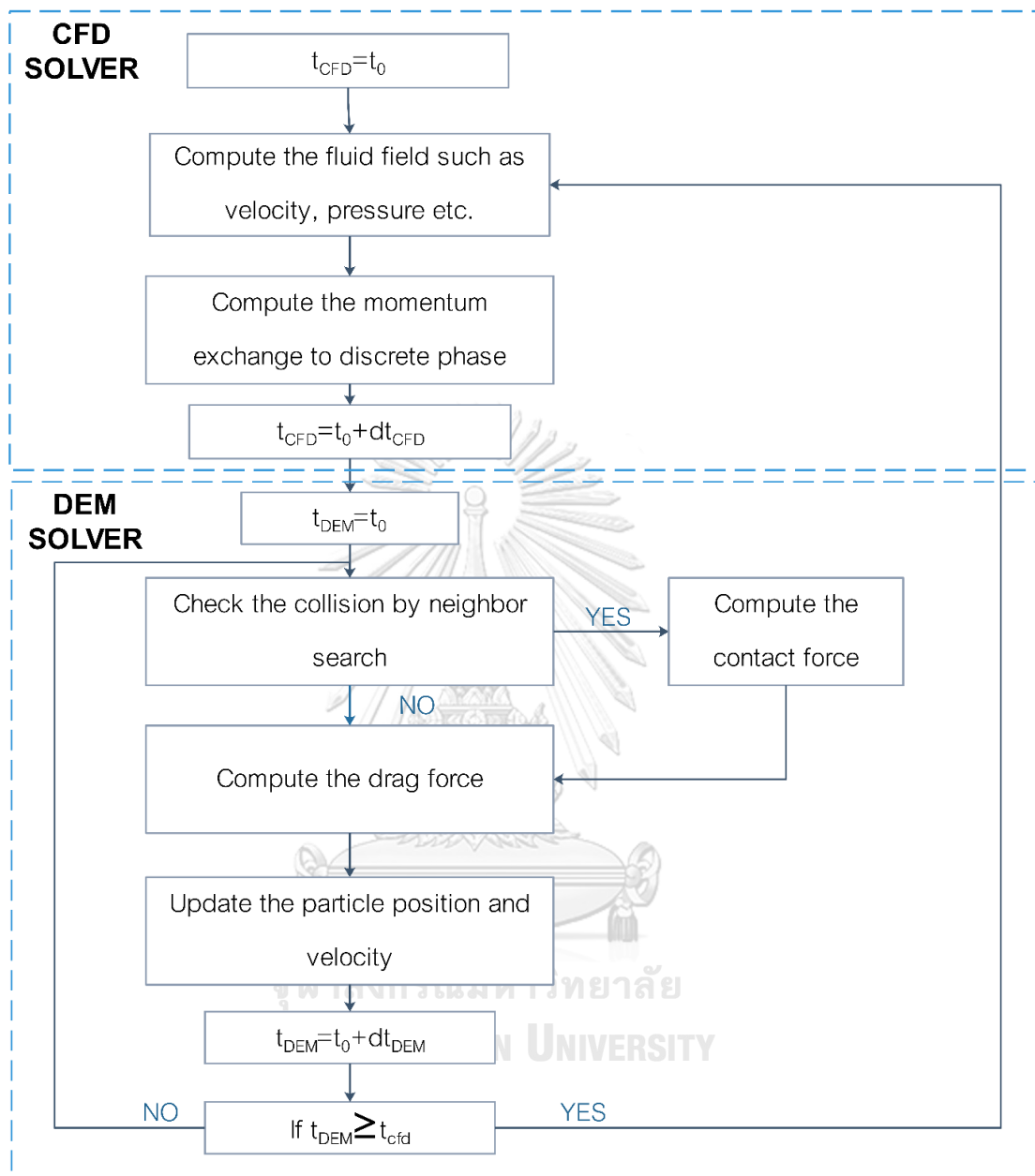


Figure 2.6 The solver algorithm of CFD-DEM simulation of MFIX open-source code for DEM simulation using a constant coefficient of restitution

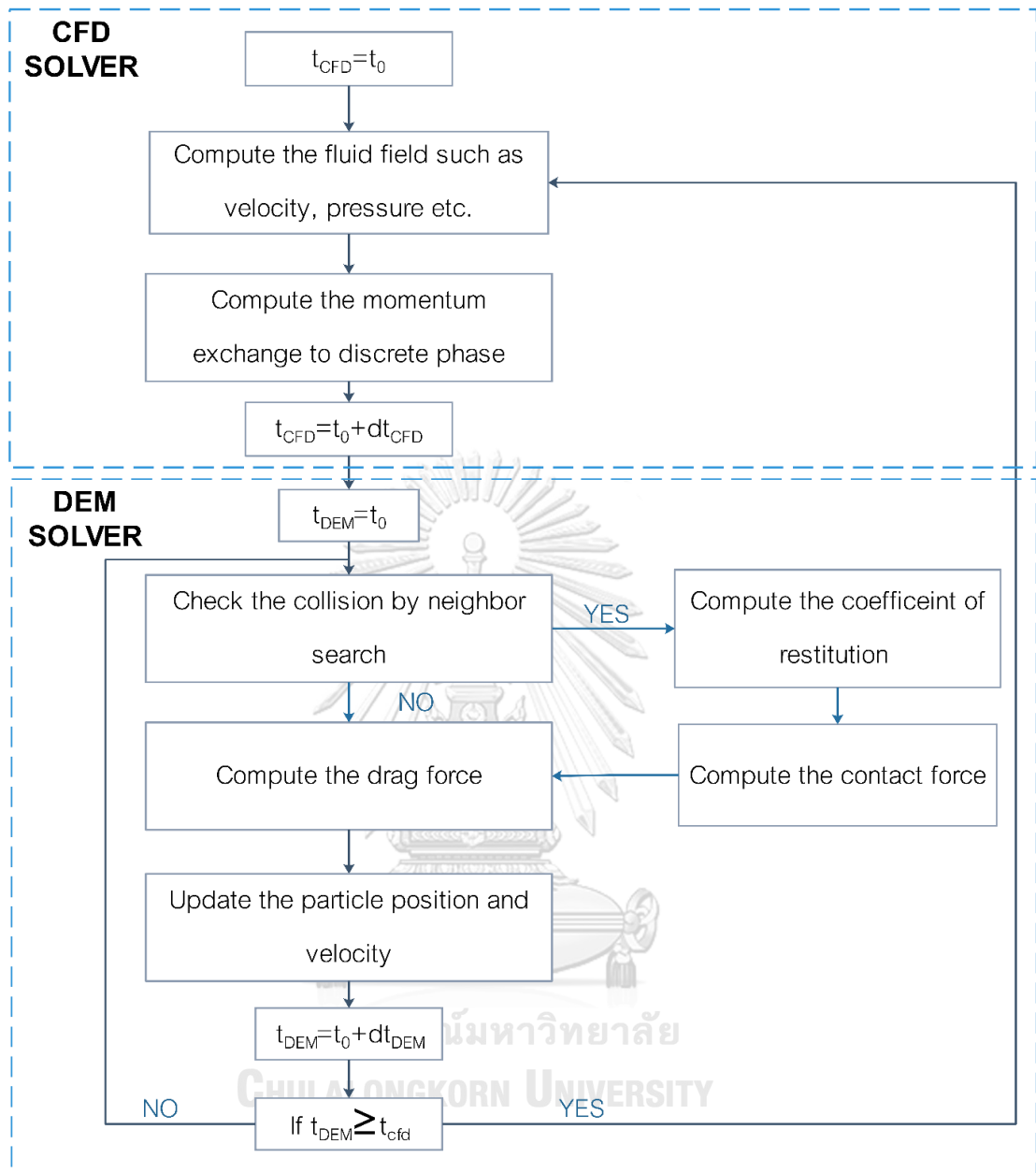


Figure 2.7 The solver algorithm of CFD-DEM simulation of MFIX open-source code for DEM simulation using dynamics coefficient of restitution

## 2.4 Coefficient of restitution

The coefficient of restitution is an important parameter which can be applied in various fields such as sports science, mechanical, robotics, earthquake and CFD simulation. It represents the energy loss during the contact. Newton (1687) defined the coefficient of restitution as the ratio of the relative velocity after the collision and relative velocity before the collision. It is typically represented by “ $e_n$ ”. The expression is shown below.

$$e_n = \frac{|v_f|}{|v_i|} \quad (57)$$

$v_f$  and  $v_i$  are the final relative velocity after contact and initial relative velocity before contact, respectively.

The coefficient of restitution is in the range between 0 and 1 as shown in Figure 2.8. The perfectly elastic collision or no kinetic energy loss during contact is represented by the coefficient of restitution equal to 1. In contrast, the zero coefficient of restitution indicates a perfectly plastic collision or total kinetic energy loss during the contact. Generally, the collision is quite difficult to maintain kinetic energy after contact. The contact models schematic are shown in Figure 2.9. Weir and Tallon (2005) proposed that the contact schematic between two objects by Figure 2.9a. The work is lost at the overlap area in which obtains the difference force pathway between the compression phase and restitution phase as shown in Figure 2.9b (Horabik et al., 2017). The total kinetic energy probably dissipates to sound, heat, viscous damping in the material, vibrational energy, wave propagation, deformation and etc. as shown in Figure 2.10 (Biele et al., 2017; Gilardi & Sharf, 2002). The trend of the coefficient of restitution and impact velocity depends on the type of material as illustrated in Figure 2.11. Also, the coefficient of restitution is a parameter which results from microscale collision.

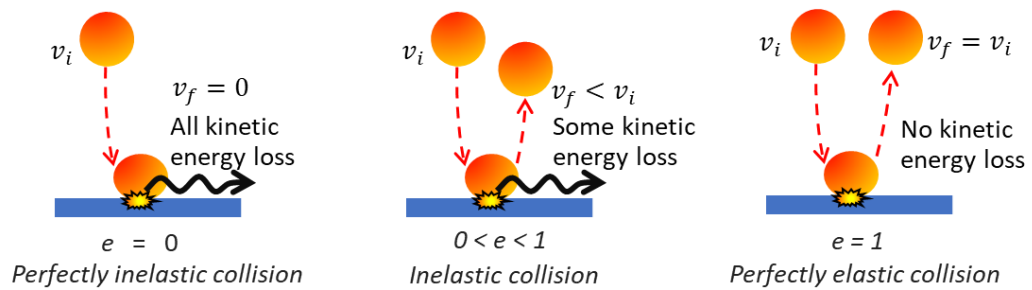


Figure 2.8 The collision phenomena at each coefficient of restitution

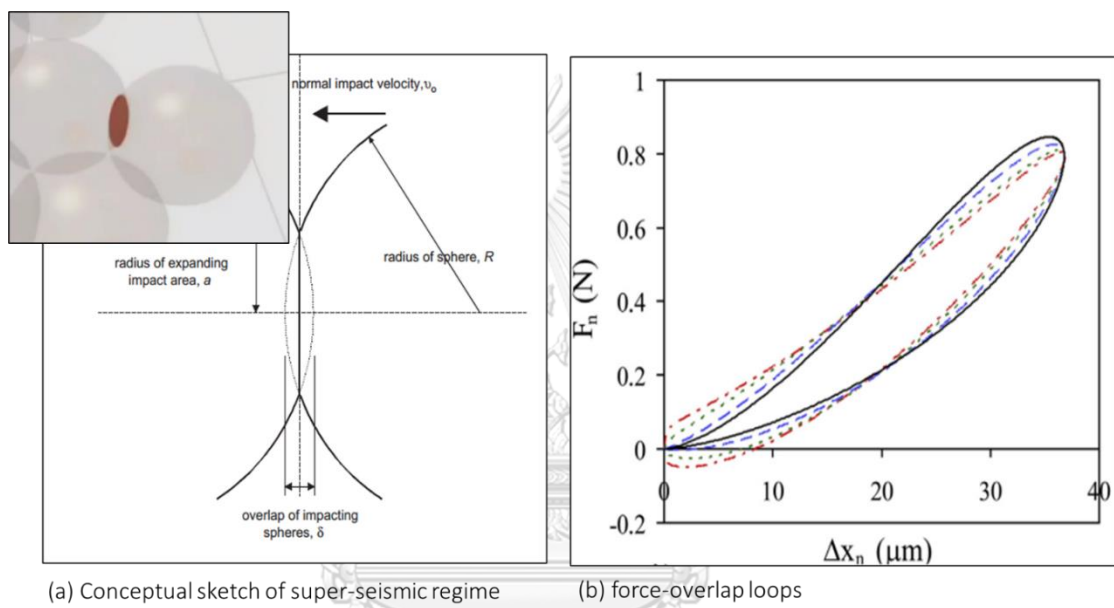


Figure 2.9 a) The collision schematic (Weir & Tallon, 2005) and b) the contact force loop during the contact (Horabik et al., 2017)

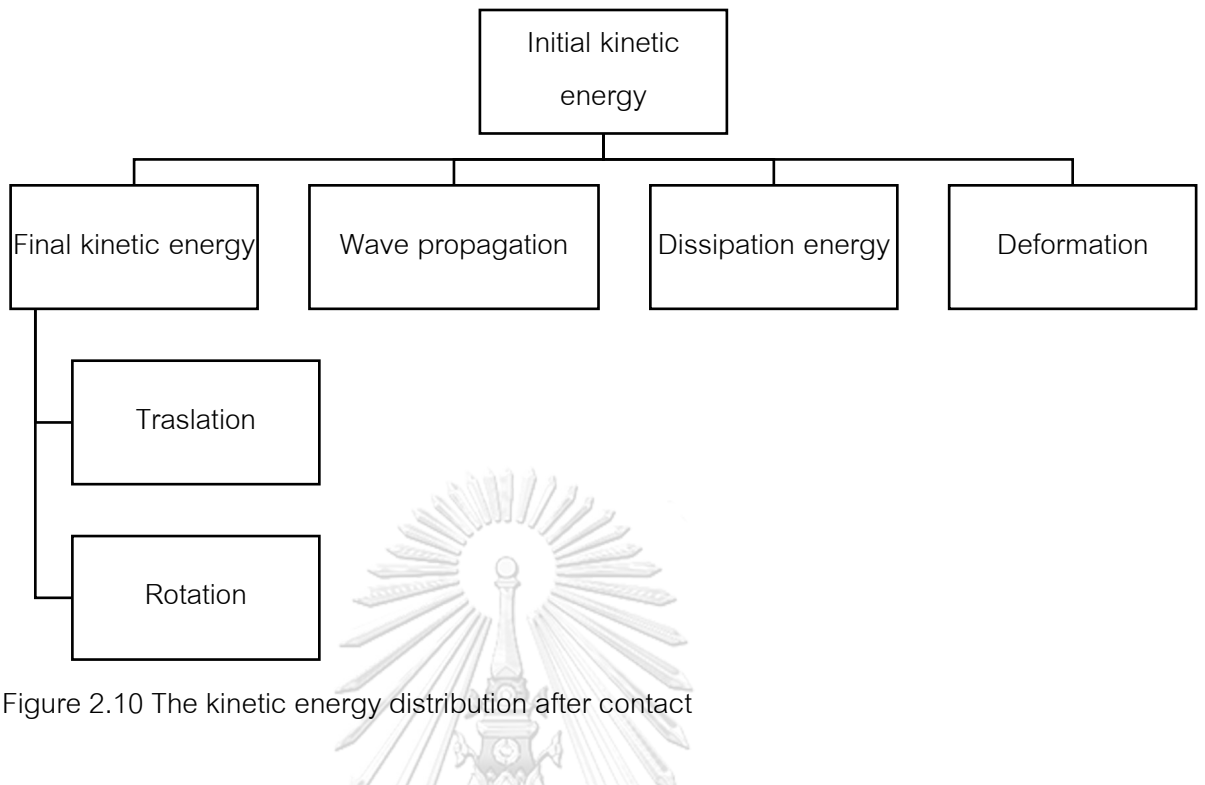


Figure 2.10 The kinetic energy distribution after contact

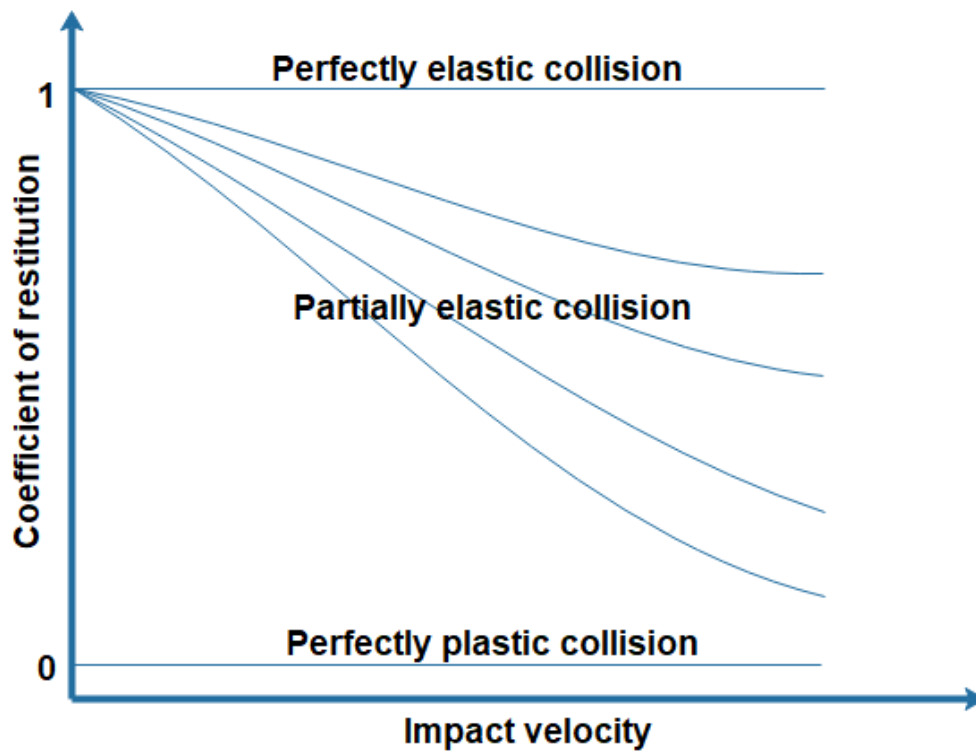


Figure 2.11 Coefficient of restitution as a function of impact velocity (Gilardi & Sharf, 2002)



## 2.5 The important of the coefficient of restitution on CFD simulation

The procedure to do the simulation is shown in Figure 2.12. The geometry is initially built for the computational domain. The operating conditions are defined in the model from the reference system or investigated model. The contact parameters such as coefficient of restitution require the assumption to complete the model before submitting the computational job. After the job is completed. The simulation result is compared with the experiment. In reality, it requires the iterative of the coefficient of restitution to obtain the simulation result which wastes of time to guess the appropriate value. This is because the microscale collision affects the interaction between the group of solid particles and then expands to the complex collision phenomena as shown in Figure 2.13. Thus, it is very important to apply the coefficient of restitution with the appropriate approach. It has many pieces of evidence demonstrated that the coefficient of restitution plays a role in the predicted phenomena.

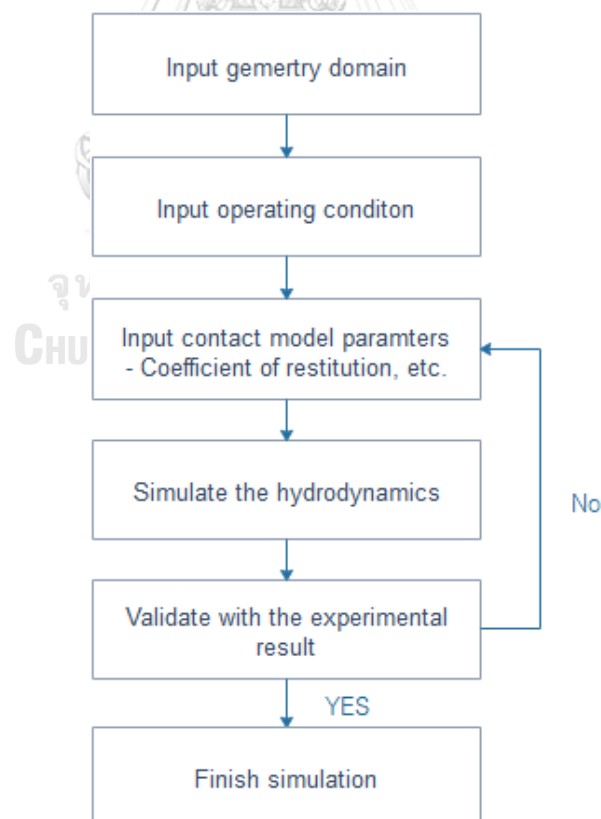


Figure 2.12 The procedure of traditional simulation with a constant coefficient of restitution

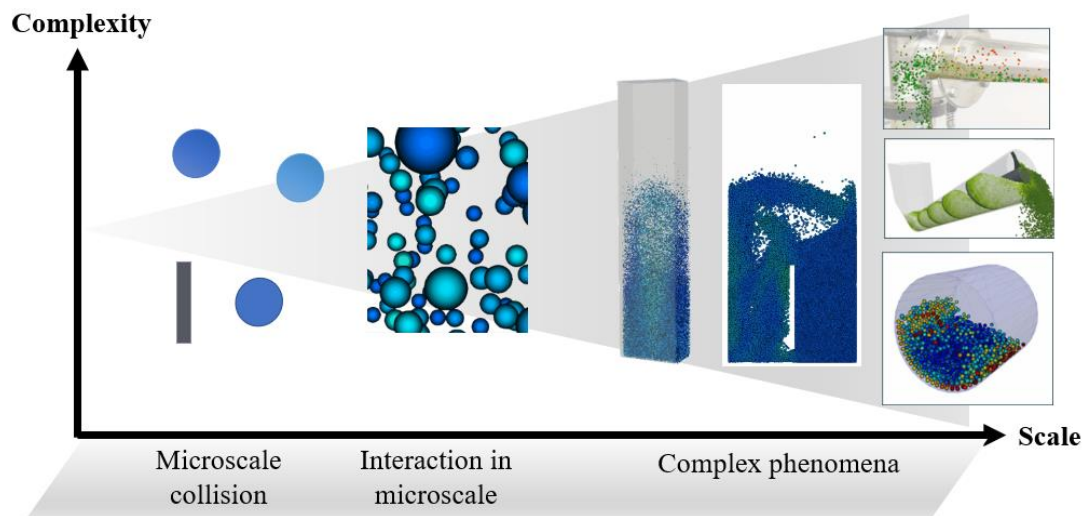


Figure 2.13 The scale metric effect of coefficient of restitution

## 2.6 Literature review

Garg, Galvin, Li, and Pannala (2012) used the open-source software to simulate the gas-solids flows by MFIX. The advantage of this software is open-source software which is available to edit the code for advanced simulation. This software used the Eulerian method to treat the fluid phase and Lagrangian method or discrete element method to treat the solid phase which based on Newton's laws of motion. The contact force model was the soft-sphere model that based on spring-dashpot. The spring-dashpot was the model to replace the collision phenomena inside the solid particle. The spring was replaced as the rebound energy after the collision happened, the dashpot was represented as the loss of kinetic energy during the collision. The program was verified with the experimental result by snapshot such as free falling of particle, simple gas-solids fluidization and repose angle of sphere particle.

Taghipour, Ellis, and Wong (2005) studied the experiment and simulation of gas-solid fluidization. This simulation was a two-dimensional column that contained glass beads diameter of 250-300  $\mu\text{m}$ . The Eulerian-Eulerian and the kinetic theory of solid were associated with simulating the multiphase between the gas-solid flow. Syamlal, Gidaspow and Wen-Yu drag models were used as the drag functions in this study. The coefficient of restitution was changed from 0.90 to 0.99. The simulation results were compared with the

experimental results by voidage and pressure drop comparison. The pressure drop profile using three drag models got similar results when the velocity was above the minimum fluidization velocity. The bed expansion ratio increased when the coefficient of restitution was changed from 0.90 to 0.99 as the perfect elastic energy when the collision between solids was occurring. Moreover, the voidage from the simulation of each drag model and experimental results was showed the similar flow pattern of bubble sizing and area of the bubble in the bed.

Aryaei, Hashemnia, and Jafarpur (2010) studied the effect of particle size on the coefficient of restitution by experimental and numerical analysis. The aluminium and steel balls were dropped to the aluminium and steel sheets. A high-speed camera was used to capture the collision profile. The experimental result was conducted to find the effect of the size of balls on the coefficient of restitution. Increasing in diameter of ball, the coefficient of restitution decreased. The relation of the coefficient of restitution was obtained by logarithm curve fitting in term of velocity. The result of the experiment was compared with the finite element analysis. The numerical simulation was performed by ANSYS using LS-DYNA module. Furthermore, the dynamic numerical study was applied to investigate the other parameter that experiment was unavailable to measure such as contact time and permanent deformation.

Y.-J. Zhang, Wang, Gu, Feng, and Wu (2016) studied the effects of the coefficient of restitution on an agitated gas fluidized bed hydrodynamics. The numerical analysis of hydrodynamics was calculated by ANSYS fluent software. The Eulerian-Eulerian, kinetic theory of granular flow and multiple reference frame was treated to the simulation. The three-dimensions geometry was constructed and varied to find the proper grid number. The grid was combined with three zones which were free fluidized zone, agitated zone and closed wall zone, respectively. This literature was focused on the effect of particle-particle coefficient of restitution and agitation speed on pressure fluctuation and solid volume fraction distribution. The time-averaged homogenous fluidization degree was the parameter that represented the standard deviation of averaged solid volume fraction. The range of homogenous fluidization degree was 0 to 1. Higher in homogenous fluidization

degree showed lower homogeneous fluidized regime that caused from the bubble inside the bed. The results also showed that the bubble inside the bed was formed bigger and the trend of homogenous fluidization degree was slightly increased when decreasing in the coefficient of restitution between particle and particle. Moreover, the bubble that occurred inside the bed was broken by increasing agitation speed. All of the results contributed to the operation diagram that illustrated the relation of the coefficient of restitution between particle and particle, agitation speed and homogenous fluidization degree which had the advantage for design and operation.

Deza, Battaglia, and Heindel (2008) validated the hydrodynamics of biomass in a fluidized bed from the simulation with x-ray radiograph. This literature used MFIx as numerical analysis software. The Eulerian-Eulerian was a multiphase flow model used in this simulation. Gidaspow model was associated as the drag force model. The bed-chamber was two dimensions which 40 cm height and 9.5 cm width. The bed was 10 cm height from the chamber bottom. The walnut shells were used as the solid particles that represented as the biomass in this study. The coefficient of restitution from 0.75 to 0.95 was selected to focus their hydrodynamics. Furthermore, the sphericity was varied from 0.5 to 0.7. The void fraction from simulation results was compared with x-ray radiograph images. Moreover, the pressure drop was also verified. The results showed that there was no significant difference between the obtained results. Thus, using the averaged value both of sphericity and coefficient of restitution had the ability to represent the properties of walnut shells.

Weir and Tallon (2005) studied the method to approximate the normal coefficient of restitution at low impact velocity. The coefficient of restitution was applied by Hertz's contact theory to approximate the coefficient of restitution in term of impact velocity, compressional wave speed, the ratio of yield pressure to Young's modulus and the number of impact repeating. The result was compared with the experiment of Goldsmith (1960) and Johnson (1985) that used aluminium sphere and brass sphere with the diameter equalled to 50 mm as the sample materials. The collision behaviour was examined for both the collision between sphere and sphere and the collision between

sphere and plate. It was illustrated that when increasing the impact repeating at the same point, the coefficient of restitution then exponentially increased and reached the constant value. This is because the decreasing in Poisson's ratio and the permanent deformation at the collision area occurred when repeating the collisions.

Ansari, Ahmad, Singh, and Singh (2015) studied the correlation between Schmidt hardness and coefficient of restitution of rocks. Basalt, granite, sandstone, limestone, marble, phyllite, quartzite and steel balls of diameter 1.5 – 5.0 cm were used as samples. The samples collided on the 5-cm thickness of slabs which materials were as same as ball material. All of the sample both slab and ball were measured the Schmidt hardness values. The result showed that both normal and tangential coefficients of restitution were increased when the slope angle increased from the horizontal. Furthermore, the result was validated with the model of Chau and Lee (1998). The scatter of result happened when lower in Schmidt hardness such as sandstone. The coefficient of restitution was then fitted to the linearly empirical equation in terms of Schmidt hardness values of samples and slabs that were validated with the experiment result.

Crüger et al. (2016) studied the coefficient of restitution of particle on the wet surface. The experiments were investigated via drop test on wet surface approach and the three dimensions collision behaviour were captured using two high-speed cameras. One camera was located at the top and the other was located in front of the object. The stokes number used to link the result between the wet coefficient of restitution and the dry coefficient of restitution. This experiment varied the layer liquid thickness (100-500  $\mu\text{m}$ ), the impact velocity and size of the glass particle. In addition, the result was compared with three models of the wet coefficient of restitution. The result showed that using three dimensions of observation via two high-speed cameras led to the smaller standard derivation than the result from 2 dimensions. The result was also validated with Ma et al. (2013) model at high impact velocity (1-2 m/s) and small layer thicknesses (100  $\mu\text{m}$ ). The liquid layer could decrease the fluctuation of data. The coefficient of restitution has been reduced with the increasing the liquid thickness because the adhesive forces resisted the bouncing force until it was stuck on the liquid film at critical thickness. The coefficient of

restitution slightly increased when the impact velocity was raised up from 1 to 2 m/s. The lower in the coefficient of restitution was obtained with the bigger size of the glass bead.

Hastie (2013) studied the coefficient of restitution of irregularly shaped particles on the horizontal plate. The high-density polyethylene pellet was used as the samples. The sphericity of the sample was 0.87 and the averaged diameter was 3.79 mm. The target materials were stainless steel and a conveyor belt. The drop test was the method to generate the kinetic energy to the particle. The mirror located as a background was at 45 degrees from the frontal of the camera. The reflection of the mirror was associated with capturing three dimensions of collision profiles by a single high-speed camera. In this literature, the coefficient of restitution was the ratio of kinetic energy output to kinetic energy input. The linear and angular kinetic energies were balanced to approximate the coefficient of restitution in term of bouncing velocity, impact velocity and reflection angle. The result showed that the coefficient of restitution between high-density polyethylene pellet and stainless-steel plate was higher than using the conveyor belt as the target material. Besides, increasing in angular velocity after impact caused in the coefficient of restitution to be lower. However, the results from the experiment still were contained some error because the collisions were manually tracked both of picture from the mirror and the actual evidence.

Bharadwaj, Smith, and Hancock (2010) studied the coefficient of restitution of pharmaceutical particles which was necessary to apply in tablets manufacturing and packaging. Many types of tablets were used as samples. The solid fraction was about 0.45-0.94. The drop test was the method to generate the kinetic energy to the sample. Plexiglas, Steel and PTFE plate was used as the target materials. The collisions were captured by a desktop camera which then was used to calculate the actual rebound velocity and impact velocity. Consequently, the coefficient of restitution was proven from the ratio of rebound velocity and impact velocity as the terms of initial drop and rebound heights. The result showed that increasing in solid fraction, the coefficient of restitution was slightly increased. The coefficient of restitution of Plexiglas was highest. In contrast, PTFE was the softer material that had more ability to absorb energy. Moreover, this



literature was compared the results with the theoretical coefficient of restitution of fully plastic and elastic-plastic predictions. The result showed that the fully plastic and elastic-plastic model was fitted with low and high solid fraction tablets, respectively.

Gibson, Gopalan, Pisupati, and Shadle (2013) studied the normal and tangential coefficients of restitution of particle. The effects of impact velocity, type of particle, type of surface and impact angle were investigated on this experiment. The kinetic energy of the particle was generated by free fall in the close chamber. The particles were dropped to the surface and captured the collision behaviour by the high-speed camera at 1000 FPS. The analysis of variance illustrated that particle modulus of elasticity, surface modulus of elasticity, normal velocity and angle of impact were the important factors. The normal coefficient of restitution reached a maximum value when the particle collided on the rigid plate at the normal angle. In the opposite, the normal coefficient of restitution was at minimum when the particle collided on the soft plate such as the soft silicone at a normal angle but the tangential coefficient of restitution increased when the angle of the plate was changed. In addition, the equation of coefficient of restitution was fitted using regression analysis.

Dong, Li, Xie, and Han (2013) studied the effect of fly ash impact velocity on the normal coefficient of restitution. The experiment was varied the impact velocity of 0.1 to 16.0 m/s. The movement of fly ash particles was generated via fluidized bed and the fly ash particles were carried to collide with the stainless plate. The collision phenomena were recorded by a high-speed camera. They found that the impact velocity gave a significant effect on the coefficient of restitution. The coefficient of restitution rapidly increased with increasing impact velocity until critical velocity. This is because of the loss from adhesive energy between particles and plate that occur at low impact velocity. On the other hand, the coefficient of restitution rapidly decreased when the impact velocity was further increased because the plastic energy loss was dominant at high impact velocity.

G. Liu et al. (2016) studied the simulation of liquid-solid fluidized bed by using the dynamics coefficient of restitution instead using the constant coefficient of restitution. The

coefficient of restitution was performed by the semi-empirical formula to evaluate the wet coefficient of restitution from the dry coefficient of restitution. The fluidized bed grid was constructed with two dimensions coordinate, 0.0512 m in width and 2.04 m in height. The simulation was run with 60 s at a time step of 0.001 s. The granular pressure as the function of the solid fraction between the simulation result and the experimental result were compared to validate the accuracy of the result. The result showed that using the constant coefficient of restitution at 0.90 was not satisfy to validated result with the experimental result. The solid fluctuation comparison showed that when using the dynamics coefficient of restitution, the amplitude and standard deviation was higher than the constant coefficient of restitution. Therefore, the dynamics coefficient of restitution was in good agreement with the experimental result than the constant one.

Horabik et al. (2017) studied the coefficient of restitution of seeds and coefficient of the visco-elastic of Hertz contact model for DEM simulation. Pea, soybean, and rapeseed with varied moisture content at velocity range 0.17 to 0.88 m/s were the study parameters for the experiment by drop test. Two high-speed cameras used to capture the collision behaviour. To decrease the variation of the result, the rebound angle from the vertical less than  $15^\circ$  was selected to analyze the coefficient of restitution. The visco-elastic Hertz contact model was applied for the collision phenomena of solid. From this model, the overlap due to the collision in the compressed phase and reform phase were hysteresis loop. The least-square method was used to evaluate the involving parameter from the Hertz contact model such as stiffness, damping parameter and exponents parameters., the contact time and impact force was measured by a piezoelectric ceramic pressure sensor to complete the model. The results showed that the coefficient of restitution value was depended on the moisture content of the seed. The increasing the moisture content of seed decreased coefficient of restitution. The result from pressure sensor illustrated that the decreasing in the coefficient of restitution, the contact time during the collision was increased. In addition, the viscoelastic model was fitted with the experimental very well.



## CHAPTER 3

### Methodology

The effect of coefficient of restitution on CFD simulation was demonstrated through various models such as three interconnected fluidized bed reactors, spouted bed reactor, internal circulating fluidized bed (ICFB) and rotating drum. The one-factor-at-a-time (OFAT) was firstly used to study the sensitivity analysis of the coefficient of restitution at each operating condition and system. In addition, the effect of contact parameters was studied using  $2^k$  factorial design through the simulation of the spouted bed reactor. The spouted bed system was selected due to the simplicity and commonly system to investigate the fundamental hydrodynamics profile of the gas-solid system. The coefficient of restitution was studied via experiment. The drop test apparatus was used to investigate the effect of material, sizing, impact velocity and temperature on the coefficient of restitution. Then, the experimental results and the results from other literature results were combined to develop the correlation of coefficient of restitution. Finally, the CFD-DEM simulations with the dynamics coefficient of restitution were performed in various model and the discussion and suggestion were obtained. The procedure of this study is illustrated below.

1. Study the effect of coefficient of restitution and contact parameters on CFD simulation
2. Develop the correlation of coefficient of restitution from experimental results and other literature results
3. Explore the CFD-DEM with the dynamics coefficient of restitution

#### 3.1 Study the effect of coefficient of restitution and contact parameters on CFD simulation

There are four simulation models in this study, three interconnected fluidized bed reactors, internal circulating fluidized bed (ICFB), rotating drum and spouted bed reactor. Each system has its own characteristic including geometry, configuration, numerical

approach and operating condition. The model configuration for all models is described below:

### 3.1.1 CFD simulation of three interconnected fluidized bed reactors using TFM approach

The three interconnected fluidized bed reactors are the fascinated model designed for hydrogen production. It is a good example model due to the variety of the fluidization regime. It consists of three fluidized bed reactors which were air reactor (AR), fuel reactor (FR) and steam reactor (SR). This system can also call chemical looping hydrogen production (CLHP) process. The system concept is illustrated in Figure 3.1. This metal oxide is used as a media to circulate in this system. In the FR, the metal oxide is reduced by a fuel gas and produces  $\text{CO}_2$  and  $\text{H}_2\text{O}$ . The reduced metal oxide is flowed to the SR and is oxidized by steam to produces  $\text{H}_2$ . The unreacted steam in the exiting gas from SR is then condensed and high purity of  $\text{H}_2$  is obtained. After that, the partially oxidized metal oxide is fully oxidized with oxygen ( $\text{O}_2$ ) in the air in AR, which sustains the heat balance of the whole system. The advantage of this process is the easy to separate  $\text{H}_2$  and steam which is the process by product (Yurata et al., 2019). Here, the simulation was simulated with cold flow CFD simulation or simulation without reaction to study the hydrodynamics profile of this complex system. The effect of coefficient of restitution on the hydrodynamics behaviour including solid velocity, solid volume fraction and solid flux was illustrated and discussed.

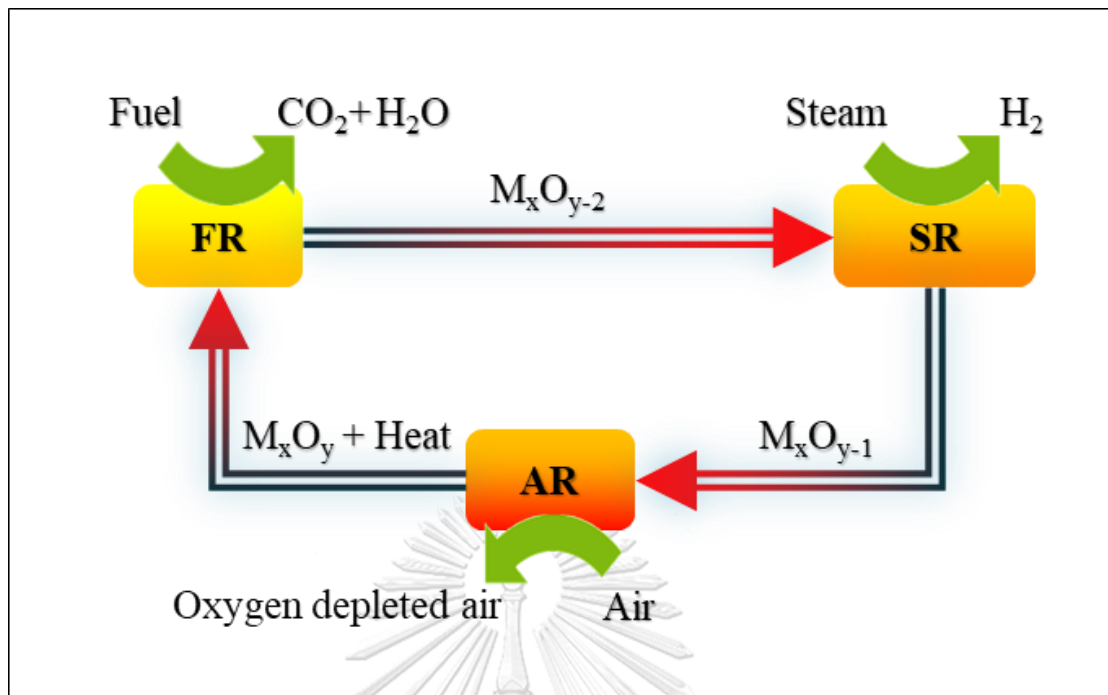


Figure 3.1 The concept of three interconnected fluidized bed reactors for chemical looping hydrogen production

### 3.1.2 Geometry and initial and boundary conditions

The geometry was based on the experimental configuration reported by Xue, Chen, Wang, and Xiang (2012) with minor modification. The experimental was scaled down from a 50 kW CLHP hot rig according to Glicksman (1984) approach. The simulation was conducted in MFIX open-source code using two-dimensional geometry to reduce the computational resource. The two-dimension geometry is shown in Figure 3.2. A ball valve and L-type loop seal at the connected between FR and SR was modified to U-type loop seal (LP). Each reactor had two zones including lower-reactor-zone and upper-reactor-zone. The diameter at upper-reactor-zone was reduced from the lower-reactor-zone to increase the solid velocity which had advantage for the circulation. The diameter of the lower-reactor-zone of AR and SR were 8 cm. The diameter of the lower-reactor-zone of FR was 13 cm. The diameters of the upper-reactor-zone of all reactors were 4 cm.

The boundary condition was set to mass inflow (MI) at the bottom of AR, SR, FR and LPs to enter the uniform superficial gas velocity. The outlet at cyclones was defined by the pressure outlet (PO) boundary condition at atmospheric pressure. The wall was

configured by the no-slip boundary for the gas phase and partial-slip boundary for solid phase except for the wall between the AR riser exit and cyclone. Free slip wall was set instead for both gas and solid phases to analogous the arrangement of experimental which arranged with the short distance between each reactor comparing to the two-dimensional geometry.

Glass bead with 200  $\mu\text{m}$  diameter at 2,500  $\text{kg/m}^3$  density was applied as the circulating media. It was categorized as Geldart's group B particles. The calculated minimum fluidization velocity ( $U_{mf}$ ) and terminal velocity ( $U_t$ ) were 5 cm/s and 158.7 cm/s, respectively (Fogler, 2010; Wen & Yu, 1966). 6 kg of solid inventory was patched at initial solid volume fraction of 0.45. The initial bed heights at AR and SR were 8 cm from the bottom. The rest of the solid inventory was in FR. The gas inlet was pure  $\text{N}_2$  which referred to the physical properties from the database of source code.



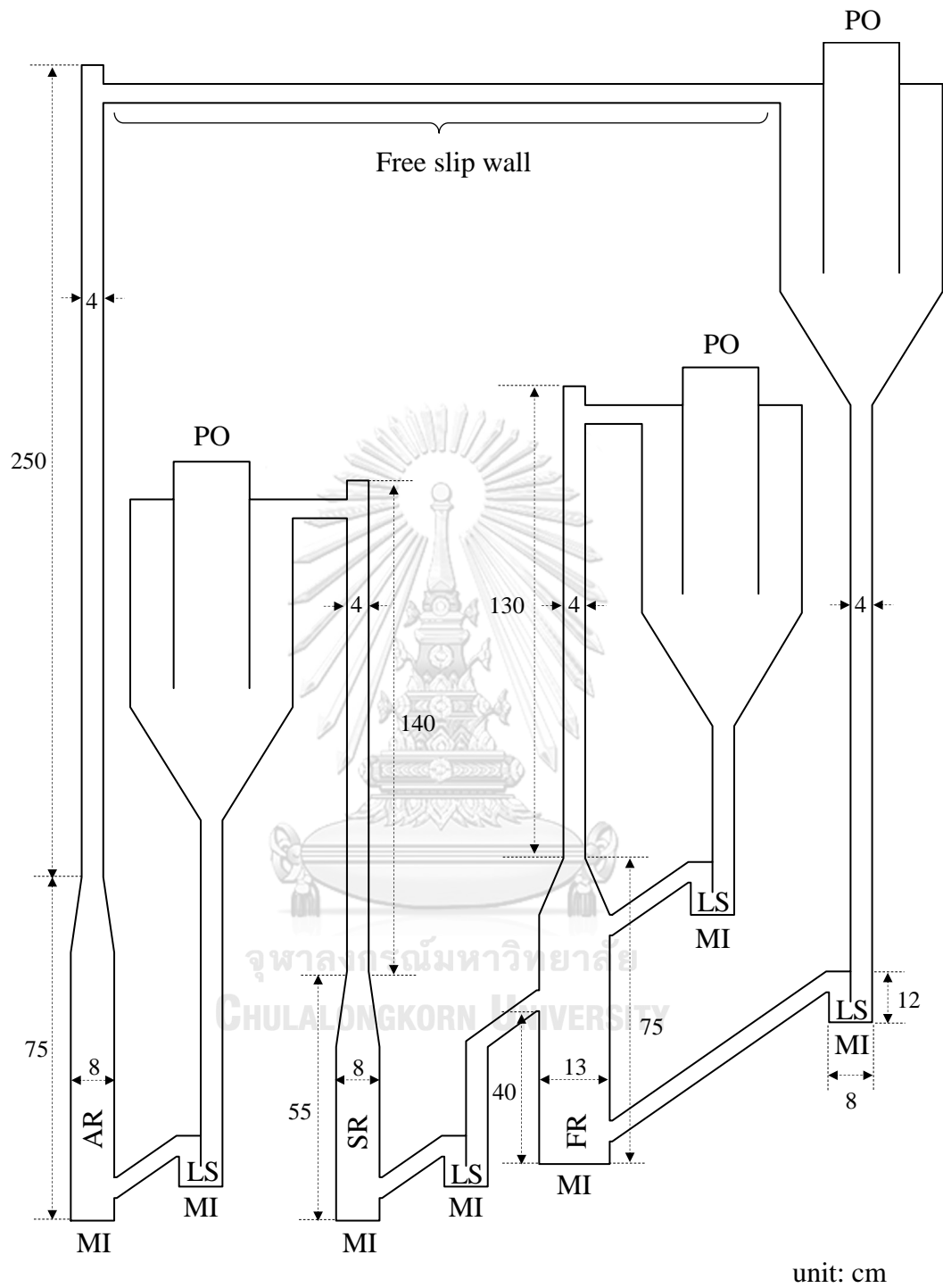


Figure 3.2 The geometry of the CLHP reactor with boundary conditions. (AR: air reactor; SR: steam reactor; FR: fuel reactor; LS: loop seal; MI: mass inflow boundary condition; PO: pressure outlet boundary condition)

### 3.1.3 Numerical configuration

The system consisted of the micron-scale of the solid particle at the high volume of solid inventory. Thus, the TFM approach was selected to reduce the computation resource. The semi-implicit method for pressure linked equations (SIMPLE) scheme deals pressure–velocity coupling on the staggered grid arrangement. The convection terms were discretized based on the first-order upwind scheme. The model conducted at an initial time step of  $1.0 \times 10^{-4}$  s with 0.8 factor adjusting time step. The restitution coefficient between the solid particles was varied at 0.70, 0.85 and 0.99. The total simulation time was 60 s. Table 3.1 summarizes the model parameter of three interconnected fluidized bed reactors for hydrogen production. The grid-independent was studied to choose a suitable grid size for this study. Three grid size such as coarse grid, medium grid and fine grid size is shown in Table 3.2

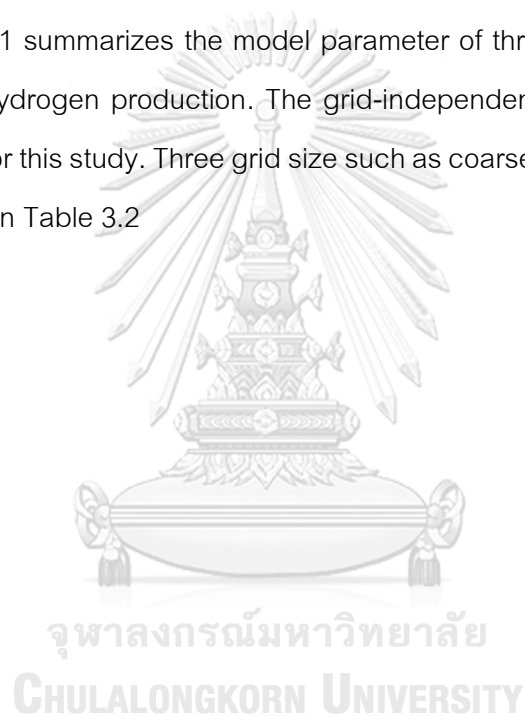


Table 3.1 Parameters for three interconnected fluidized bed reactors for chemical looping hydrogen production simulation

Parameter	Unit	Value
Solid inventory	kg	5
Solid density	kg/m <sup>3</sup>	2500
Solid diameter	μm	200
Grid size	mm	2.5
Initial time step	s	1 x 10 <sup>-4</sup>
Time step adjusting factor		0.8
Simulation time	s	60
Drag model		Adjusted Syamlal O'Brien (Esmaili & Mahinpey, 2011)
Restitution coefficient		0.70, 0.85, 0.99
Solids phase stress model		Lun et al. (Lun, Savage, Jeffrey, & Chepuruiy, 1984)
Minimum fluidized velocity	cm/s	5
AR Inlet velocity	cm/s	170
SR Inlet velocity	cm/s	170
FR Inlet velocity	cm/s	50
LSs Inlet velocity	cm/s	5

Table 3.2 Grid-independent study for three interconnected fluidized bed reactors for chemical looping hydrogen production simulation

Comparison list	Description		
Grid size (mm)	1.25	2.50	4.00
Grid size/Particle diameter	6.25	12.5	20
Number of grids	900737	228007	91072

### 3.2 CFD simulation of internal circulating fluidized bed (ICFB) using DEM approach

The internally circulating fluidized bed (ICFB) is the fluidized bed which divides by a plate at the center of the reactor as shown in Figure 3.3. It separates two sections in which the solid can circulate between two sections. It widely uses in many application such as energy production, desulfurization, incineration of solid wastes and etc. (Feng et al., 2012) due to the reduction of heat loss and compact size (X. Yang, Wang, Li, Liu, & He, 2020). The typical ICFB has separated two sides such as high-velocity chamber (HV) and low-velocity chamber (LV). The solid particles are moved upward and overflow from the HV chamber to the LV chamber. The solid particles are accumulated and pushed the solid in LV downward and re-circulated to HV chamber at the bottom. In this section, the effect of material type and coefficient of restitution on the hydrodynamics profile including solid vertical velocity and solid flux are investigated.

#### 3.2.1 Geometry and initial and boundary conditions

The configuration was set up as shown in Figure 3.3. The geometry was similar to the study of Q. Zhang et al. (2018). Their study set the ICFB model to illustrate the improvement of CFD with the dynamics coefficient of restitution using coupled Eulerian fluid phase-Eulerian solid phase-Lagrangian discrete particle phase (CEEL). The HV chamber was at the left side which had 24 mm width. The LV chamber was at the right side which had 24 mm width. The total height of ICFB was 250 mm. Two chambers were separated by vertical baffle at the center of the vessel. The height of baffle was 75 mm which located above the bottom 15 mm. 20,000 discrete solid particles were loaded in the chamber. The solid diameter was 1.0 mm. Two material types were studied such as glass bead and polypropylene.



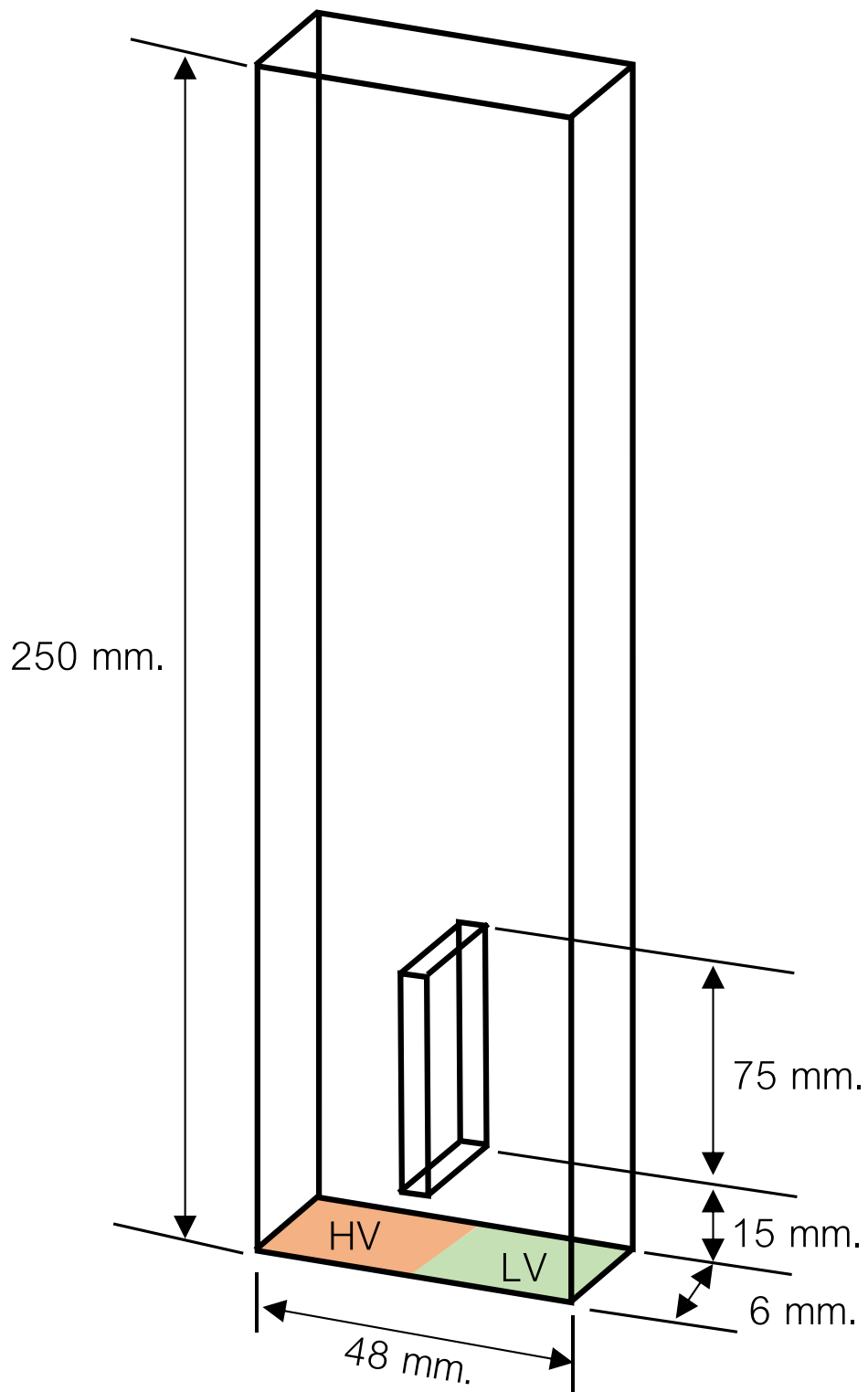


Figure 3.3 Internal circulating fluidized bed geometry configuration

### 3.2.2 Numerical configuration

The simulation of ICFB was conducted in MFIX using DEM approach. The 20,000 solid particles can be handled by discrete phase at reasonable computational resource requirement. The realistic collision was obtained. Firstly, the grid-independent was studied. Three grid size including coarse grid, medium grid and fine grid was studied as shown in Table 3.3. The grid-independent was required because the DEM simulation of ICFB had to compute the hydrodynamics of the gas phase. The sizing of control volume was significant to predict the momentum transfer between gas and solid phases. There were two cases of ICFB. The model configuration is summarized in Table 3.4. The first case was operated using glass bead circulating in the ICFB. The other case was operated using polypropylene. The minimum fluidization velocity of the glass bead was 0.53 m/s. The minimum fluidization velocity of polypropylene was 0.26 m/s. In HV case, the superficial gas velocity was introduced as two times of minimum fluidization velocity while in in LV case, the superficial gas velocity was introduced as 1.2 times of minimum fluidization velocity. The predicted minimum fluidization velocity was calculated from the Wen and Yu (1966) correlation. The linear spring-dashpot (LSD) was selected to compute the contact force inside the system. The coefficient of restitution was varied from 0.75, 0.85 and 0.99 to study the effect of this value to the hydrodynamics behaviour. In addition, the model was simulated using time step adjustment with an initial time step of  $1.0 \times 10^{-5}$  s, maximum time step of  $1.0 \times 10^{-3}$  s and factor adjustment of 0.8.

Table 3.3 Grid-independent study for Internal circulating fluidized bed

Comparison list	Description		
	Coarse	Medium	Fine
Cells in width-direction	8	12	15
Cells in height-direction	40	50	60
Cells in thickness-direction	4	4	6

Table 3.4 Simulation parameters of ICFB model

Geometry	Unit	Value	
Width of HV chamber	mm.	24	
Width of LV chamber	mm.	24	
Height of reactor	mm.	250	
Thickness of reactor	mm.	6	
Height of slot	mm.	15	
Height of baffle	mm.	75	
Parameter	Unit	Value	
Particle material		Glass bead	Polypropylene
HV air inlet velocity	m/s		
LV air inlet velocity	m/s		
Number of particles		20,000	
Particle density	kg/m <sup>3</sup>	2,600	900
Particle diameter	mm	1	1
Spring constant	N/m	800	800
Particle - Particle restitution coefficient		0.80, 0.90, 0.99	
Particle - Wall restitution coefficient		0.80, 0.90, 0.99	
Particle - Particle friction coefficient		0.10	0.10
Particle - Wall friction coefficient		0.10	0.10
Gas viscosity	Pa.s	$1.8 \times 10^{-5}$	
Gas density		Ideal gas law	
Drag model		Beetstra-van der Hoef-Kuipers	
Initial time step	s	$1.0 \times 10^{-5}$	
Time step factor adjustment		0.8	
Maximum time step	s	$1.0 \times 10^{-3}$	
Simulation time	s	10	

### 3.3 CFD simulation of rotating drum using DEM approach

The rotating drum is widely used in a variety of applications such as food, mineral, energy production, etc. It operates by rotating the drum from the external force. The friction force and gravity force are major force acting at the solid particles. The efficiency of the rotating drum depends on its design and operating condition. The used drum diameter was similar to the study of Rong et al. (2020) as shown in Figure 3.4.

#### 3.3.1 Geometry and initial and boundary conditions

The rotating drum with 0.05 m diameter and 0.1 m depth was simulated. The three-dimensional geometry is illustrated in Figure 3.4. The boundary condition at the wall was set to partial slip condition with the defining friction coefficient. The lids of the drum were defined as free slip condition. Twenty thousand glass bead particles with 1 mm diameter were loaded at the center of the drum.

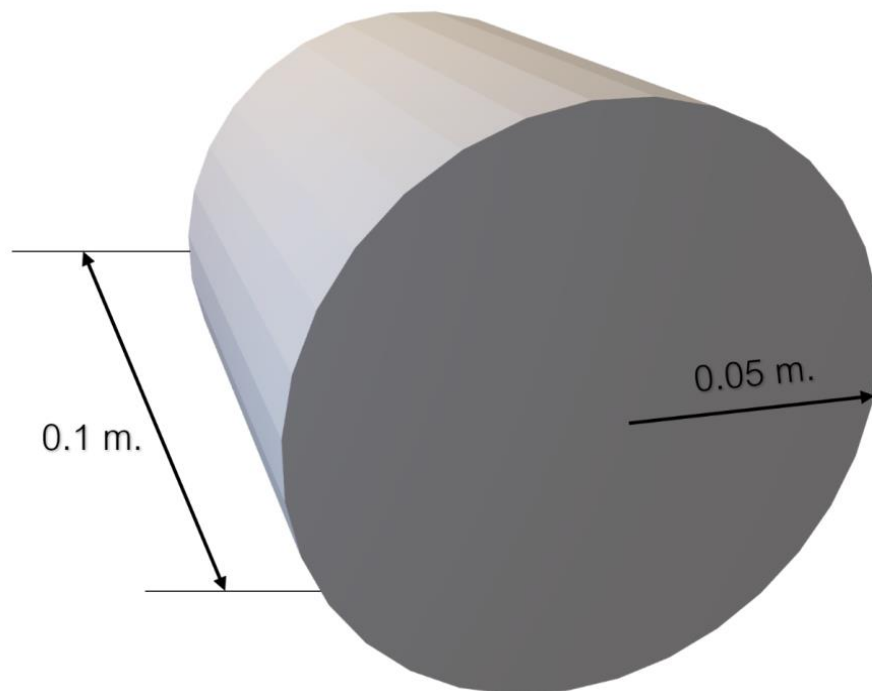


Figure 3.4 Rotating drum geometry

### 3.3.2 Numerical configuration

Table 3.5 shows the simulation parameter of the rotating drum. The rotating speed was defined at 15 RPM and 35 RPM. Three constants of the coefficient of restitution such as 0.8, 0.9 and 0.99 were defined in the model. The angle of repose by snapshot and power draw were selected to compare. The angle of repose was the primary hydrodynamics profile to determine the solid movement and avalanche of the solid particle. The power draw was significant parameter which represented the energy requirement to rotate the drum at each operating condition. It referred to the energy consumption per unit time in causing motion of the solid. It was calculated by the multiplication of mass of the solid particle, gravitational acceleration, and vertical velocity (Bbosa, Govender, & Mainza, 2016). The simulation time was 10 second. The adaptive time was applied with an initial time step of  $1.0 \times 10^{-5}$  s, a maximum time step of  $1.0 \times 10^{-3}$  s and a factor adjustment of 0.8.

Table 3.5 The simulation parameters of the rotating drum

Geometry	Unit	Value
Drum diameter	m.	0.10
Drum length	m.	0.10
Parameter	Unit	Value
Number of particles		20,000
Particle density	kg/m <sup>3</sup>	2,600
Particle diameter	mm	1
Spring constant	N/m	800
Particle - Particle restitution coefficient		0.80, 0.90, 0.99, dynamics
Particle - Wall restitution coefficient		0.80, 0.90, 0.99, dynamics
Particle - Particle friction coefficient		0.10
Particle - Wall friction coefficient		0.10

### 3.4 CFD simulation of the spouted bed using DEM approach

The spouted bed was chosen due to the utilization of the coarse particles (Mathur & Gishler, 1955). It is widely used in various industry such as petrochemical (Wolff, Salikov, Antonyuk, Heinrich, & Schneider, 2014), food (Pohndorf et al., 2016), wastewater treatment (Darwish, Zewail, Yousef, & El-Tawail, 2015), pharmaceutical (Suresh, Sreedhar, Vaidhiswaran, & Venugopal, 2017), and energy industries (Jeremiáš et al., 2017). The significant of contact parameters both individual effect and interaction effect was studied by  $2^k$  factorial design. The studied contact model parameters consisted of the particle-particle friction coefficient (A), spring constant (B), the ratio of the tangential spring constant to normal spring constant (C), normal restitution coefficient (D), and tangential restitution coefficient (E). The linear spring-dashpot (LSD) contact model was employed in this study due to the simplification of the model. The LSD contact force was the combination of elastic term and dissipation term. The three-dimensional base case transient simulation of the spouted bed reactor was validated with the experimental result from Link et al. (2008). The translation of the kinetic energy of the particles, the rotational kinetic energy of the particles, the expansion of the bed, and the standard deviation of the pressure drop were the response parameters related to the influence of the contact force modeling parameters the hydrodynamics profile. These data will improve our understanding of system phenomena as a result of changing modeling contact parameters including main effect and interaction effect. In addition, it will be used as a guideline for CFD-DEM simulation in the other gas-solid multi-phase flow simulation.

#### 3.4.1 Geometry and initial and boundary conditions

The model consisted of 44,800 spherical glass beads with a 4.04 mm diameter and  $2,526 \text{ kg/m}^3$  density. The geometry of spouted bed was shown in Figure 3.5. The spouting inlet was fed at the center of the bottom of the reactor. The background inlet was supplied around spouting inlet area to enhance the solid hold up. The model parameters were summarized in Table 3.6. The pressure of spouting inlet and background inlet was

1.5 atm and 1 atm, respectively. The top of the model was defined to be the pressure outlet at ambient.

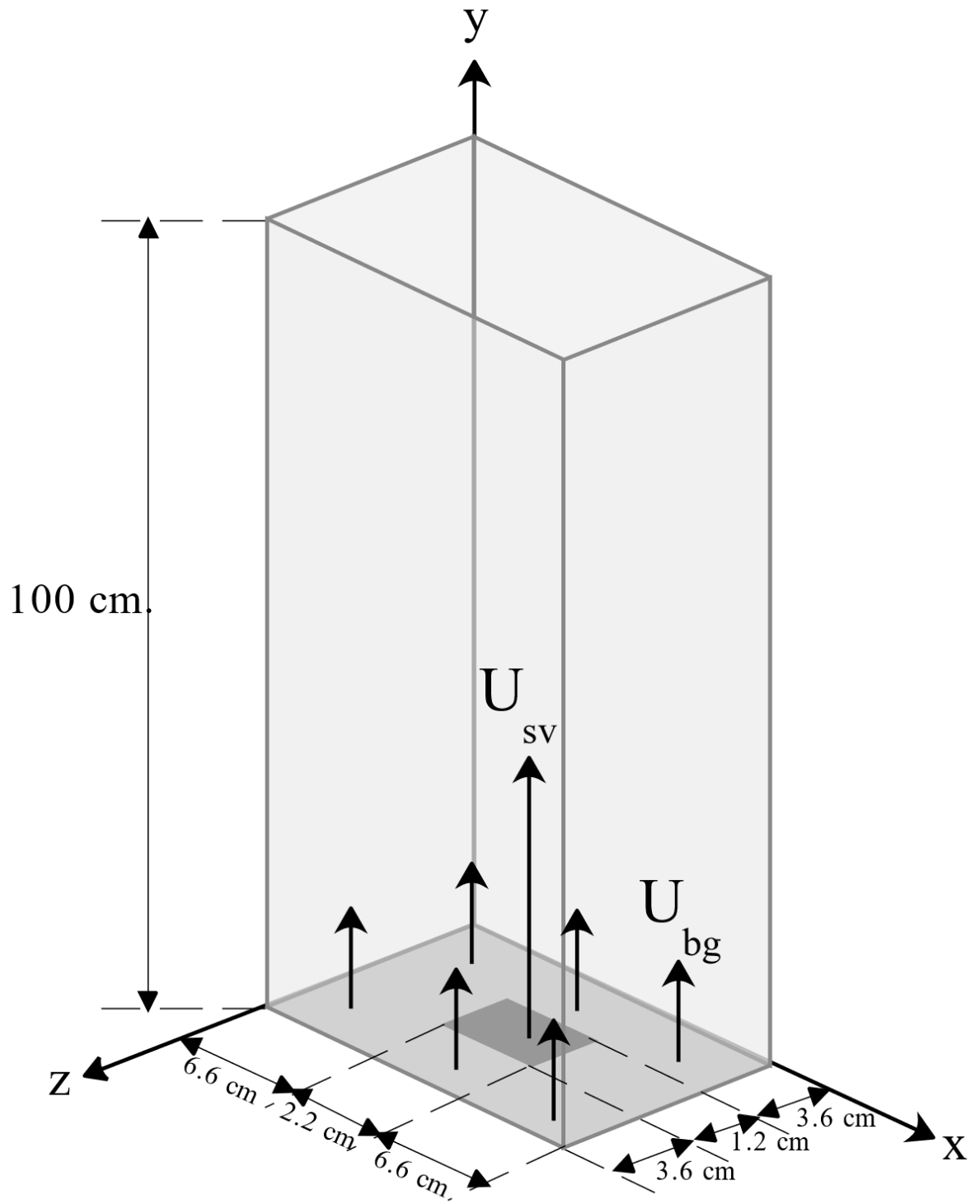


Figure 3.5 Schematic of the three-dimensional spouted bed reactor

Table 3.6 Geometries and parameters for the base case numerical simulations

Geometry	Unit	Value
Width	m.	0.154
Height	m.	1.000
Depth	m.	0.084
Cells in x-direction		26
Cells in y-direction		167
Cells in z-direction		14
Parameter	Unit	Value
Initial bed height	m	0.19
Initial solid fraction		0.63
Diameter	mm	4.04
Density	kg/m <sup>3</sup>	2526
Spring constant	N/m	800
Particle - Particle restitution coefficient		0.97
Particle - Wall restitution coefficient		0.97
Particle - Particle friction coefficient		0.10
Particle - Wall friction coefficient		0.10
Gas		
Temperature	K	298
Background velocity	m/s	2.50
Spout gas velocity	m/s	60.00
Viscosity	Pa.s	$1.8 \times 10^{-5}$
Density	Ideal gas law	
Drag model	Beetstra-van der Hoef-Kuipers	

### 3.4.2 Numerical configuration

The employed equations were solved by the Semi-Implicit Method for Pressure Linked Equation (SIMPLE) algorithm with the Bi-Conjugate Gradients Stabilized method



(BICGSTAB) and the diagonal scaling precondition. The discretization scheme was the first-order upwind. The drag model was the Beetstra - Van der Hoef - Kuipers (BVK) (Beetstra, van der Hoef, & Kuipers, 2007) similar to the previous study from Link et al. (2008). The contact model was employed by linear spring-dashpot model (LSD) which required many parameters such as the spring constant, restitution coefficient, and friction coefficient. The contact parameters were chosen from the reference literature and previously studied of this model. The model was simulated on Cartesian coordinate with the cut-cell technique. The adaptive time step was set to the model to control the stabilized of solver and reduce the computational resources. The initial time step was  $10^{-4}$  s. The minimum time step was  $10^{-6}$  s. The maximum time step was  $10^{-3}$  s. The model was adjusted the time step automatically using the adjusting time step factor 0.9. The grid independence was studied to explore the appropriate sizing of the grid as shown in Table 3.7. Although the grid size did not have an effect on the hydrodynamics profile for DEM without fluid calculation. Because the neighbour search algorithm manipulated the collision when two particles were closed at least 1.2 times of radius. The simulation with two operating conditions was shown in Table 3.8. Both case B1 and case B2 were validated with the experimental result from Link et al. (2008).

Table 3.7 Grid independency test studies

Comparison list	Grid characteristic		
	Coarse	Medium	Fine
Cells in x-direction	19	26	32
Cells in y-direction	125	167	208
Cells in z-direction	11	14	18
Total	26125	60788	119808

Table 3.8 Operating conditions for model validation

Case	Flow regime	Background velocity $V_{bg}$ (m/s)	Spout gas velocity $V_{sp}$ (m/s)	Simulation time (s)
B1	Intermediate/ Spout fluidization	2.5	60	7.5
B2	Spouting with aeration	2.5	90	7.5

#### 3.4.3 Numerical configuration: Experimental design

OFAT method is the commonly experimental design approach. One factor or independent factor is sequential changed while the other variables are fixed at constant. It is suitable for the study which aims to focus only on the trend at the specific circumstance. It is widely used because it is required less cost but it requires the number of cases to deal with high fluctuation experiment. The trouble has happened if the response does not depend on only the selected variable.

The design of experiments (DOE) is an analysis technique which deals with the statistical method. It allows the researcher to evaluate the testing, screening, analyzing, and interpreting of the interesting factors including the interaction between factors.  $2^k$  factorial design is a popular experimental design among DOE approaches. In  $2^k$  factorial design, "2" represents the two levels of each factor, low level denoted by (-1) and high

level denoted by (+1). “k” denotes the factor in the experiment. It was most suitable in the early stages of the experiment to investigate the importance of individual factor and interaction factor in which is mandatory of this study. The example case with two factors (A and B) is used to elaborate the procedure to interpret the results via  $2^k$  factorial design. In Figure 3.6, A obtains the positive response while B obtains the negative response. Besides, the interaction between A and B or AB is not clarifying as same as the main effect of A and B. The procedure of  $2^k$  factor design is summarized in Figure 3.7.

There are many statistical methods such as the simplex-centroid design (Dias et al., 2014), the extreme vertices design (J.-T. Ding, Yan, Liu, & Zhu, 1999), and the  $2^k$  factorial experimental design (Lazic, 2006). It depends on the objective to select the experimental design approach.  $2^k$  factorial design was selected in this study which aims to screen the significant of individual factor and interaction between factors. It was received attention to study the complicated behaviour of gas-solid systems.

The significant of individual factors and interaction between factors was analyzed the hypothesis by an analysis of variance (ANOVA) analysis. In ANOVA analysis, the probability value (p-value) with p-values less than 0.05 was the judgement criteria the important factors. In this part, the effect of contact parameters such as the particle-particle friction coefficient (A), spring constant (B), the ratio of the tangential spring constant to normal spring constant (C), normal restitution coefficient (D), and tangential restitution coefficient (E) was investigated by  $2^k$  experimental method. Firstly, the minimum and maximum of each parameter are summarized in Table 3.9. The experimental range and denoted level are shown in Table 3.10. The simulation was run only operating condition B1 due to the overflow flow operating condition B2. The simulation case corresponding to  $2^k$  factorial design with 5 effects can be generated 32 cases as shown in Table 3.11. The main effect, the interaction and hypothesis testing by ANOVA analysis were discussed the impact and significance. The response parameters were total translation kinetic energy, rotational kinetic energy, bed expansion ratio and standard deviation of pressure drop. The total kinetic energy of motion ( $KE_{Total}$ ) consists of translational kinetic energy

( $KE_{\text{Translation}}$ ) and rotational kinetic energy ( $KE_{\text{Rotational}}$ ), which can be expressed in the formulas below.

$$KE_{\text{Total}} = KE_{\text{Translation}} + KE_{\text{Rotational}} \quad (58)$$

$$KE_{\text{Translation}} = \frac{1}{2}mv^2 \quad (59)$$

$$KE_{\text{Rotational}} = \frac{1}{2}I\omega^2 \quad (60)$$

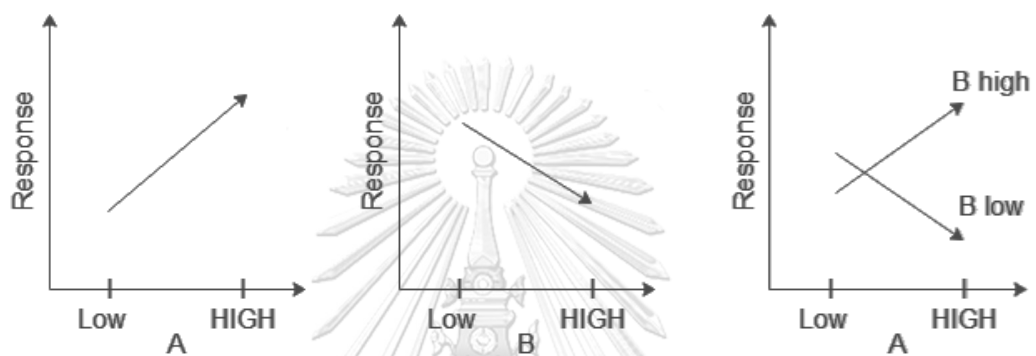


Figure 3.6 The example of main effect and interaction effect

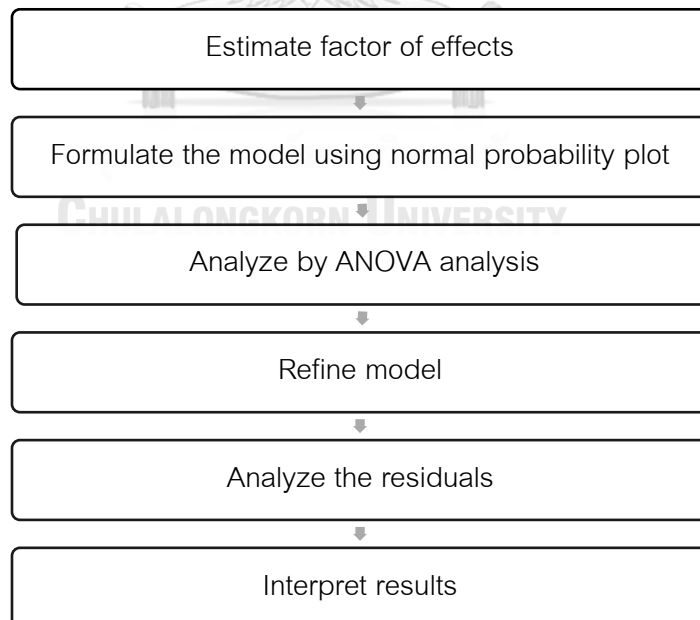


Figure 3.7 The procedure of  $2^k$  factorial experimental design

Table 3.9 The reference information

Author	Friction coefficient ( $\mu$ ) (-)	Spring constant, $k_n$ (N/m)	$k_t/k_n$ (-)	$e_n$ (-)	$e_t$ (-)
Abbasfard, Evans, and Moreno-Atanasio (2016)		1000	0.10-0.50		
Asegehegn, Schreiber, and Krautz (2012)				0.95	
Deb and Tafti (2014)	0.10	800		0.9	
Kawaguchi, Tanaka, and Tsuji (1998)	0.10-0.30	800		0.9	
T. Li, Zhang, and Hernández-Jiménez (2016)	0.60	2000	0.29	0.95	
M. Liu, Wen, Liu, Liu, and Shao (2015)	1.00E-05			0.50	0.50
P. Liu and Hrenya (2014)	0.40	200		0.90	
Navarro and de Souza Braun (2013)		800		0.98	0.10
Qiu et al. (2016)	0.30	800		0.90	
S. Yang, Luo, Fang, and Fan (2013)	0.27	420		0.71	
S. Yang, Luo, Fang, Zhang, and Fan (2014)	0.30	800		0.97	
S. Yang, Luo, Zhang, Qiu, and Fan (2015)	0.30	800		0.97	
S. Yang, Sun, Zhang, Zhao, and Chew (2016)	0.10			0.97	
Zhao, Xu, and Zheng (2017)	0.10	210		0.9	0.10
L. Zhou et al. (2017)	0.33	410		0.97	

Table 3.10 Level of modeling parameters

Parameter	Symbol	Unit	Code level	
			-1	1
Particle – particle friction coefficient ( $\mu$ )	A	-	0.00001	0.60
Spring constant ( $k_n$ )	B	N/m	200	2000
Ratio of the tangential spring constant ( $k_t/k_n$ ) to normal spring constant	C	-	0.10	0.50
Normal restitution coefficient ( $e_n$ )	D	-	0.50	0.98
Tangential restitution coefficient ( $e_t$ )	E	-	0.10	0.50

Table 3.11 Simulation case in  $2^k$  factorial experimental design

CASE	CODE				
	A	B	C	D	E
1	-1	-1	-1	-1	-1
2	1	-1	-1	-1	-1
3	-1	1	-1	-1	-1
4	1	1	-1	-1	-1
5	-1	-1	1	-1	-1
6	1	-1	1	-1	-1
7	-1	1	1	-1	-1
8	1	1	1	-1	-1
9	-1	-1	-1	1	-1
10	1	-1	-1	1	-1
11	-1	1	-1	1	-1
12	1	1	-1	1	-1
13	-1	-1	1	1	-1
14	1	-1	1	1	-1
15	-1	1	1	1	-1
16	1	1	1	1	-1
17	-1	-1	-1	-1	1
18	1	-1	-1	-1	1
19	-1	1	-1	-1	1
20	1	1	-1	-1	1
21	-1	-1	1	-1	1
22	1	-1	1	-1	1
23	-1	1	1	-1	1
24	1	1	1	-1	1
25	-1	-1	-1	1	1
26	1	-1	-1	1	1
27	-1	1	-1	1	1
28	1	1	-1	1	1
29	-1	-1	1	1	1
30	1	-1	1	1	1
31	-1	1	1	1	1
32	1	1	1	1	1

### 3.5 Develop the correlation of coefficient of restitution from experimental results and other literature results

#### 3.5.1 COR measurement

According to the definition of COR, the final relative velocity after contact and initial relative velocity before contact are the essential collision parameters. Capturing the collision is the fundamental method which uses to investigate the COR. Basically, the COR is measured by the drop test apparatus as shown in Figure 3.8. The experimental setup consists of background, plate holder, high-speed camera, continuous light source, particle motorized releaser and heating unit. The motorized particle releaser is attached to the electric height adjustment for changing the drop height level. The drop height can be changed up to 1.5 m which generates the maximum impact velocity of 5.4 m/s. The motorized particle releaser is the key to this experiment. It controls the drop quality which releases the particle from the rest state. The particle releaser made from the drill chuck. The tommy bar key attached to the low round per minute motor which can keep the releasing quality for all experimental cases. The experimental supporter is made from an aluminum profile with foot adjustable to set the balance. Moreover, the base of supporter is loaded with a gallon of water and sand to minimize the effect of vibration during the contact. A high-speed camera with accessories is used to capture the impact velocity and rebound velocity during the contact. NAC Memrecam HX-7S is employed as a high-speed camera in this study. It configures monochrome type at 4000 frames per second (fps) and 1152x864 pixels of resolution to record the particle trajectory.

The case studies are summarized in Table 3.12. Case 1 and 2 aim to study the effect of impact velocity on the coefficient of restitution. The other cases aim to study the effect of temperature on the coefficient of restitution at each impact velocity. The glass bead and polypropylene are selected due to the famous in CFD modelling as same as the material of the wall such as acrylic and steel. The materials and operating temperature are selected from the famous fluidization system simulation and experiment (Jung, Gidaspow, & Gamwo, 2005; F.-R. Liu, Chen, Li, & Wang, 2017; Mansourpour, Karimi, Zarghami, Mostoufi, & Sotudeh-Gharebagh, 2010). At the final stage, the results from the



experiment are combined with the results from the other references in Table 3.13 to ensure the variety of data for correlation development.

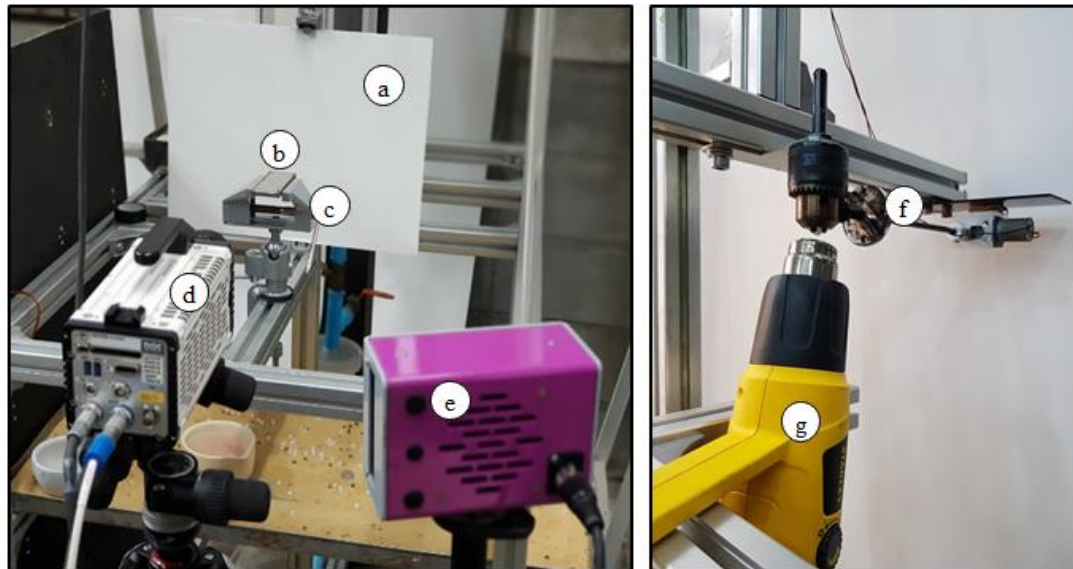


Figure 3.8 Drop test apparatus where a) background, b) plate, c) plate holder, d) high speed camera, e) continuous light source, f) motorized releaser and g) heat gun with temperature controller

Table 3.12 Drop test experimental cases

No	Solid particle	Plate	Temperature (°C)	Melting temperature (°C)
1	Glass bead	Acrylic	30	704
2	Polypropylene	Acrylic	30	160
3	Glass bead	Steel	30	704
4	Glass bead	Steel	100	704
5	Glass bead	Steel	170	704
6	Glass bead	Steel	240	704
7	Glass bead	Steel	310	704
8	Polypropylene	Steel	30	160
9	Polypropylene	Steel	60	160
10	Polypropylene	Steel	90	160
11	Polypropylene	Steel	120	160
12	Polypropylene	Steel	150	160

\*Solid particle diameter (3-6 mm.)

Table 3.13 Drop test experimental results from reference literatures

Reference	Material		Impact velocity (m/s)
	Solid particle	Plate	
Marinack Jr, Musgrave, and Higgs III (2013)	Glass, Brass, Low carbon steel, Chrome steel, S2 tool steel, Tungsten carbide, Stainless steel	Steel, Glass, Stainless steel	2.15-3.10
Aman et al. (2016)	Chrome, Steel, Glass	Steel, Glass	0.09-0.13
Minamoto, Seifried, Eberhard, and Kawamura (2008)	Suj2 steel	Suj2 steel	0.19-0.19
Gorham and Kharaz (2000)	Steel, Aluminum	Steel	0.38-1.89
J. Coaplen, W. Stronge, and B. Ravani (2004)	Chrome steel	Aluminum, bronze	0.59-3.02
This study	Glass bead, Polypropylene	Acrylic steel	1.40-5.52

\*Testing particle diameter (1-6 mm)

### 3.5.2 Image analysis

To investigate the COR at any condition, the high-speed camera is used to record the collision behaviour. The image analysis is a technique which is widely used to interpret the result from the captured image. In this study, the image analysis is applied to collect the particle trajectory from a high-speed camera at 4000 frames per second (FPS). The particle tracking is accomplished by MATLAB with image processing library as shown in Figure 3.9a. The grayscale record is preferred due to high contrast and light sensitivity.

Firstly, grayscale particle trajectories are converted from grayscale to black and white to normalize the noise in each frame as shown in Figure 3.9b. The pixel of grayscale consists of the number presenting the brightness of the pixel by 0 to 255. "0" is carried black color, and "255" is carried white color. The middle value is carried grey color. After changing greyscale to black and white, each pixel is normalized to the integer 0 and 1 in which "0" is carried black color and "1" is carried white color. After that, the blank frame, or the frame before doing the experiment is set as the reference frame. The position of the solid particle is detected by the subtraction between the  $i^{\text{th}}$  frame and reference frame as shown in Figure 3.9c. The position of the solid particle is identified by the centroid of the solid particle as shown in Figure 3.9d. The velocity is derived from the position and time duration between the frame at 1/4000 second.

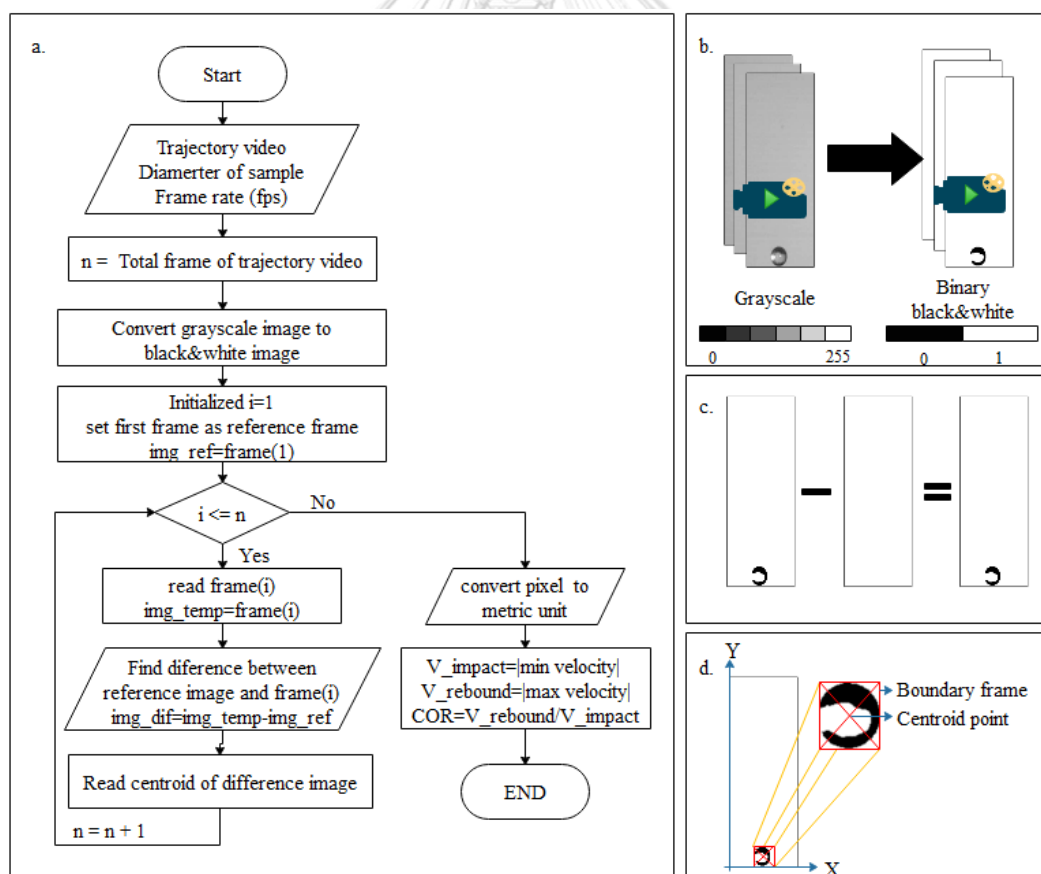


Figure 3.9 a) The algorithm of image analysis for particle tracking, b) grayscale to binary image conversion, c) image subtraction and d) particle tracking analysis

### 3.5.3 Correlation of coefficient of restitution

The effect of diameter, impact velocity, material type and temperature on the coefficient of restitution was plotted to investigate the trend using for developing the coefficient of restitution function. The individual effect was plotted to diminish the unnecessary parameter in the correlation of coefficient of restitution. In each case, the coefficient of restitution was fitted with the function of impact velocity. This is because the impact velocity has the most resolution data comparing to other results. After that, the coefficient from the fitting function of impact velocity was compared and find the correlation of each factor in the function of physical properties. The effective elastic modulus ( $E^*$ ) was used to represent the combination of physical properties of the material which proposed by Hertz (1896). It combined the Poisson ratio and elastic modulus together in one term. The effective elastic modulus is shown below.

$$\frac{1}{E^*} = \frac{1-\nu_1^2}{E_1} + \frac{1-\nu_2^2}{E_2} \quad (61)$$

The temperature was included in the correlation as the correction factor function. Finally, the predicted coefficient of restitution was compared with the experimental results and the traditional coefficient of restitution model from Thornton (1997) as shown below.

$$e_{th} = \left\{ \left( \frac{6\sqrt{3}}{5} \right) \left[ 1 - \frac{1}{6} \left( \frac{v_Y}{v_{imp}} \right)^2 \right] \right\}^{\frac{1}{2}} \left\{ \left( \frac{v_Y}{v_{imp}} \right) \left[ \left( \frac{v_Y}{v_{imp}} \right) + 2\sqrt{1.2 - 0.2 \left( \frac{v_Y}{v_{imp}} \right)^2} \right]^{-1} \right\}^{\frac{1}{4}} \quad (62)$$

$$v_Y = 3.194 \left( \frac{(\sigma_Y)_{Th} (R^*)^3}{(E^*)^4 m^*} \right)^{\frac{1}{2}} \quad (63)$$

### 3.6 Develop the CFD-DEM with the dynamics coefficient of restitution

This section aimed to present the comparison between the simulation using the constant coefficient of restitution and the dynamics coefficient of restitution. The correlation of coefficient of restitution was applied to the contact subroutine in MFIx open source code. There were 2 modules, "Calc\_force\_wall dem.f" and "Calc\_force\_dem.f" involving the contact force calculation. The module "Calc\_force\_wall dem.f" computed the contact between solid particle and wall. The module "Calc\_force\_dem.f" calculated the contact force between the solid particle and solid particle. The modified "Calc\_force\_wall dem.f" and "Calc\_force\_dem.f" were developed. The constant coefficient of restitution was replaced with the correlation of coefficient of restitution to develop the CFD-DEM simulation with the dynamics coefficient of restitution.

The feasibility of applying the dynamics coefficient of restitution was performed with four cases of the solid system among the various processes. Free fall simulation, internal circulating fluidized bed and rotating drum and spouted bed reactor were the simulation cases which aimed to show the comparison of typical DEM simulation and this novel DEM simulation. Only DEM simulation was performed due to the correlation was developed on the individual particle kinetic data. The free fall of single-particle was validated with the experimental results. The simulation configuration is shown in **Figure 3.10**. The particle was released from rest at different initial height. The rebound height from the simulation was compared with the experimental results. The solid velocity and solid flux were compared for internal circulating fluidized bed. For rotating drum, the snapshot of the angle of repose and power draw was illustrated. For the spouted bed reactor model, the configuration was similar to the previous study as shown in **Table 3.6** Geometries and parameters for the base case numerical simulations **Table 3.6** and **Figure 3.5**. In this apparatus, the vertical velocity was compared with the study of from Link et al. (2008) .

In the final part, the suggestion to develop the CFD simulation with TFM approach using the dynamics coefficient restitution was analyzed.

## Free fall simulation

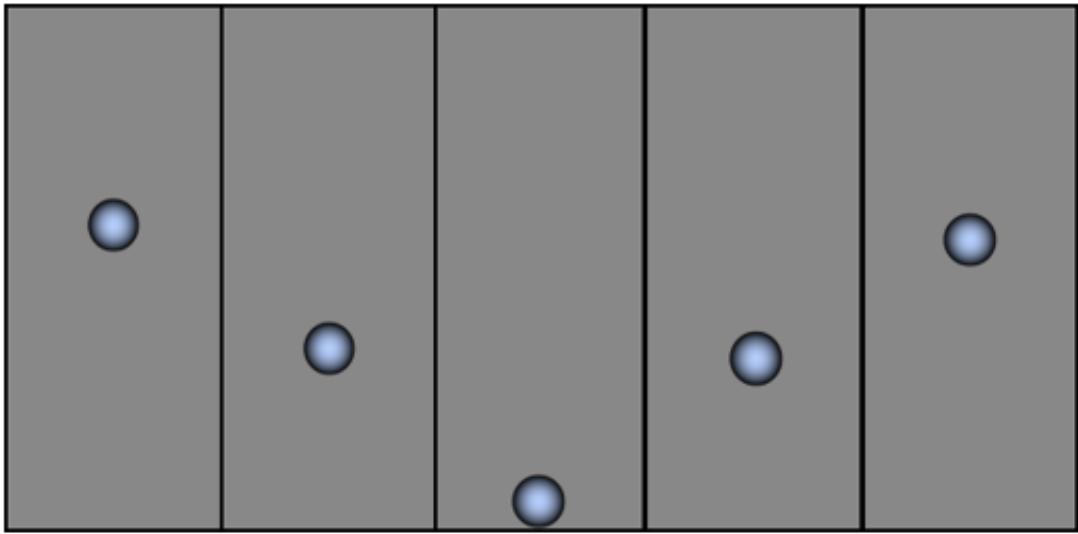


Figure 3.10 Free fall simulation



## CHAPTER 4

### Sensitivity analysis of the coefficient of restitution in a various computational fluid dynamics (CFD) simulation models using one-factor-at-a-time (OFAT) methodology

The collision is a fundamental phenomenon that occurs in various multiphase flow gas-solid systems. It plays an essential role in the characteristic of hydrodynamics profile which results from the operating condition. This chapter aims to demonstrate the sensitivity analysis of the coefficient of restitution on the CFD simulation for both TFM approach and DEM approach.

#### 4.1 CFD simulation of three interconnected fluidized bed reactors using TFM approach

The chemical looping for hydrogen production using three interconnected fluidized bed reactors was selected. This process is a novel process which receives more attention for hydrogen production. The system consists of three reactors, three cyclones and four-loop seals. Xue et al. (2012) developed the experimental prototype for this process. However, the CFD simulation is still needed to paid attention for investigating the phenomena in which experimental can not measure.

##### 4.1.1 Grid independency

The multi-scale characteristics (macro, meso, micro) had a major impact on the predicted hydrodynamics (Agrawal, Loezos, Syamlal, & Sundaresan, 2001). For the effect of grid size on the predicted hydrodynamics, three unified grid sizes of 1.25 mm, 2.5 mm and 4.0 mm representing 6.25, 12.5 and 20 particle diameters were investigated. It is known as a fine grid, medium grid and coarse grid, respectively. Figure 4.1 demonstrates the influence of the grid size on the solid volume fraction along with the AR height. The medium grid and the fine grid predicted a comparable pattern of the solid volume fraction, whereas the coarse grid obtained the overestimate of solid volume fraction. The similarity was observed by percentage difference of solid volume fraction in AR. The results showed that the medium grid and the fine grid had 3.7 % difference, while the coarse grid had 48.6 % difference from the medium grid. However, the medium grid size decreased the



computational time from 250 hours for the fine grid to 30 hours. The justification of accuracy and computational cost was concluded that the medium grid size was suitable for this study. Moreover, the used medium grid size was corresponded to the suggestion size around ten times of solid particle diameter by Andrews, Loezos, and Sundaresan (2005).

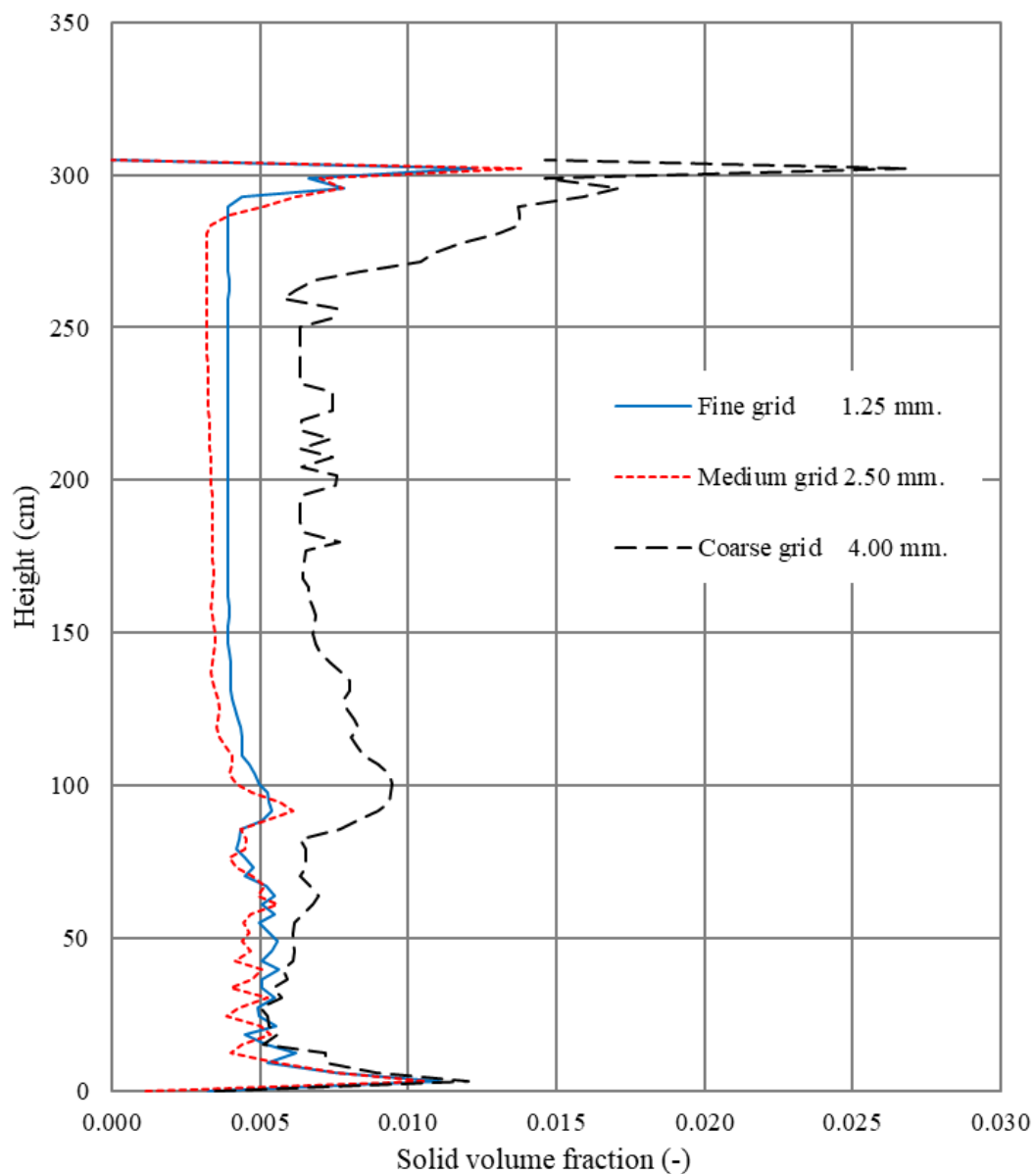
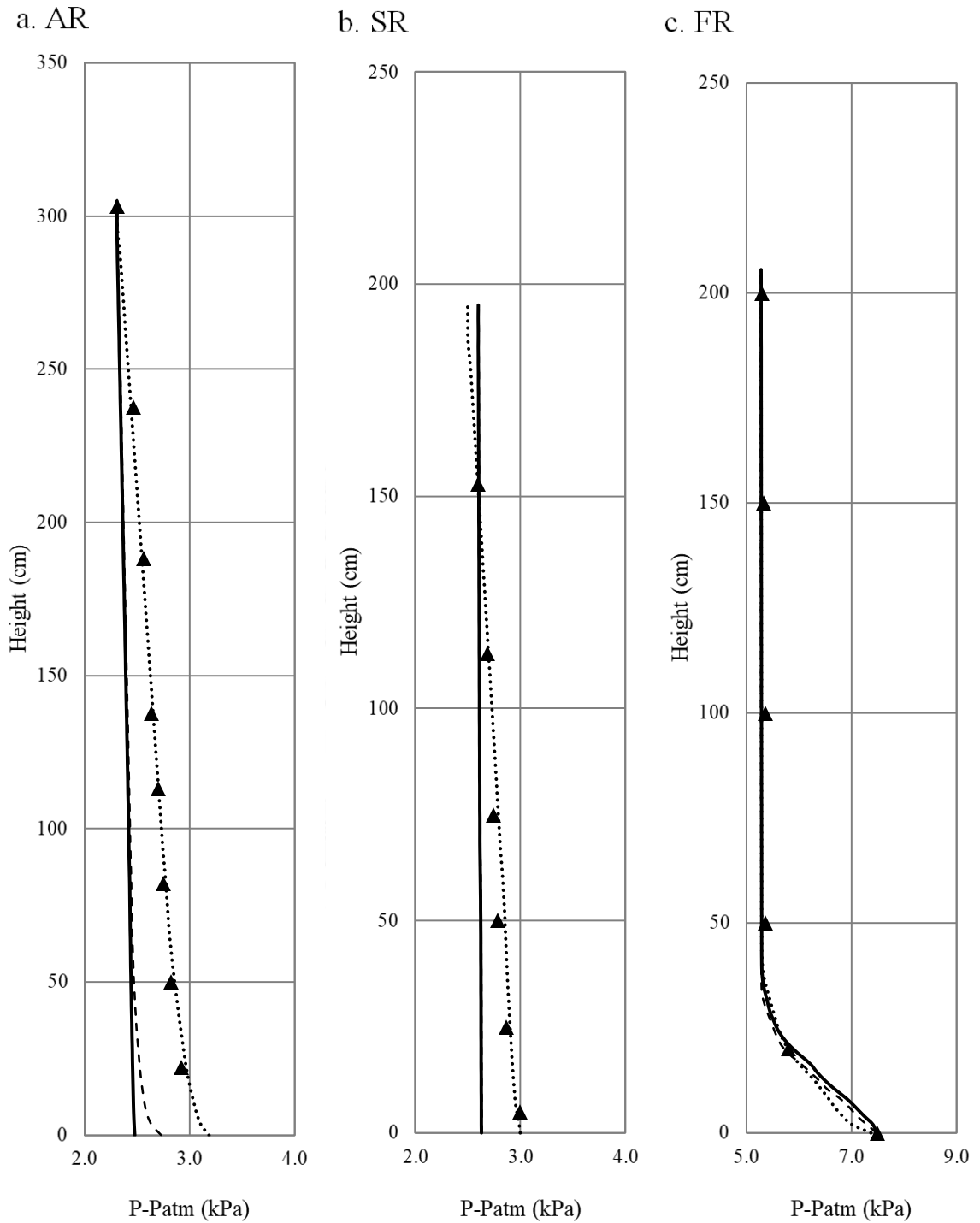


Figure 4.1 The solid volume fraction profile of AR with various grid sizes. (Solid inventory: 5 kg, where  $V_{AR} = 170$  cm/s,  $V_{SR} = 170$  cm/s,  $V_{FR} = 50$  cm/s and  $V_{LS} = 5$  cm/s)

#### 4.1.2 Model validation

The pressure drop profile along the height of each reactor for comparing between simulation result and the experimental results (Xue et al., 2012) is shown in Figure 4.2. The drag model played an important role in this simulation. It typically determines from the experimented pressure gradient and it relates to the momentum exchange between gas and solid particle. In this study, the Gidaspow drag model (Gidaspow, 1994), original Syamlal–O'Brien drag model (Syamlal & O'Brien, 1989) and modified Syamlal–O'Brien drag model (Esmaili & Mahinpey, 2011) were employed. In the modified Syamlal–O'Brien drag model, adjusting the parameters,  $C_1$  and  $C_2$  were modified to 11.772 and 0.182 respectively (Esmaili & Mahinpey, 2011). The drag model was studied with the coefficient of restitution of 0.99 to ensure the solid transfer through the cycle. The results showed the good agreement of pressure profile from all drag model in FR. In contrast, the underestimated pressure profile was obtained on AR and SR for Gidaspow drag model and original Syamlal–O'Brien drag model. This is because the Gidaspow drag model and original Syamlal–O'Brien drag model is developed from the bubbling regime which corresponds to the regime in FR (Mahinpey, Vejahati, & Ellis, 2007). Due to the CLHP process consisted of two regimes, the fast fluidization regime in AR and SR and the bubbling regime on FR. The suitable drag model should handle the variety of regime in the system. The modified Syamlal–O'Brien drag model based on Esmaili and Mahinpey (2011) was introduced for this study. The good agreement of pressure profile in AR, SR and FR were obtained for the model with the modified Syamlal–O'Brien drag model as shown in Figure 4.2.



--- Gidaspow — Original Syamlal O'Brien ..... Adjusted Syamlal O'Brien (Esmaili & Mahinpey, 2011) ▲ Experiment (Xue et al., 2012)

Figure 4.2 The pressure profiles of cold flow model simulation for a) AR, b) SR and c) FR

(solid inventory = 5 kg,  $V_{AR} = 170$  cm/s,  $V_{SR} = 170$  cm/s,  $V_{FR} = 50$  cm/s and  $V_{LS} = 5$  cm/s)

#### 4.1.3 The effect of coefficient of restitution on the hydrodynamics profile

The snapshots of the void fraction at different simulation times including coefficient of restitution of 0.70, 0.85 and 0.99 are shown in Figure 4.3. The fundamental behaviour of solid circulation was similar for all the cases. After the gas was feed to the system. The bed was initially expanded and transformed the packed bed to fluidization stages. The small bubbles were formed near the inlet (0.2 s) and moved upward to the surface of the bed. Smaller bubbles merged to larger bubble. At 2.0 s, the bubbles broke at the bed surface. After 2.0 s, the bed in FR was expanded and initially overflown to the LS. Besides, the bed expansion of AR and SR were increased rapidly due to the high inlet gas velocity. After that, the mixed gas-solid particle was separated at the cyclone. The gas was separated from the atmosphere at the top of the cyclone. The kinetic energy of solid was loss after the collision to the wall of the cyclone. After that, the solid was fallen to the LS and fed to the next reactor. The hydrodynamics profile was similar for AR and SR. However, the snapshot observed the difference in FR. The bubble formation was related to the coefficient of restitution. The decreasing of the coefficient of restitution inferred more loss of momentum from the collision. Moreover, it increased the bubble due to the dissipation energy after contact which lead to the particle attaching and the void formation. The solid flux along the simulation time is plotted in Figure 4.4. The solid flux had large oscillation and unstable state at the beginning. The simulation was taken approximately 25.0 s to reach a pseudo steady state. The oscillation was high for the simulation using a low coefficient of restitution. As stated above, this is because the decreasing of the coefficient of restitution inferred more loss of momentum from the collision. Figure 4.5 shows the average solid flux in the pseudo-steady-state with simulation time of 40-60 s. The result showed that the coefficient of restitution of 0.99 obtained the highest solid flux due to the highest ability to conserve the kinetic energy of solid.

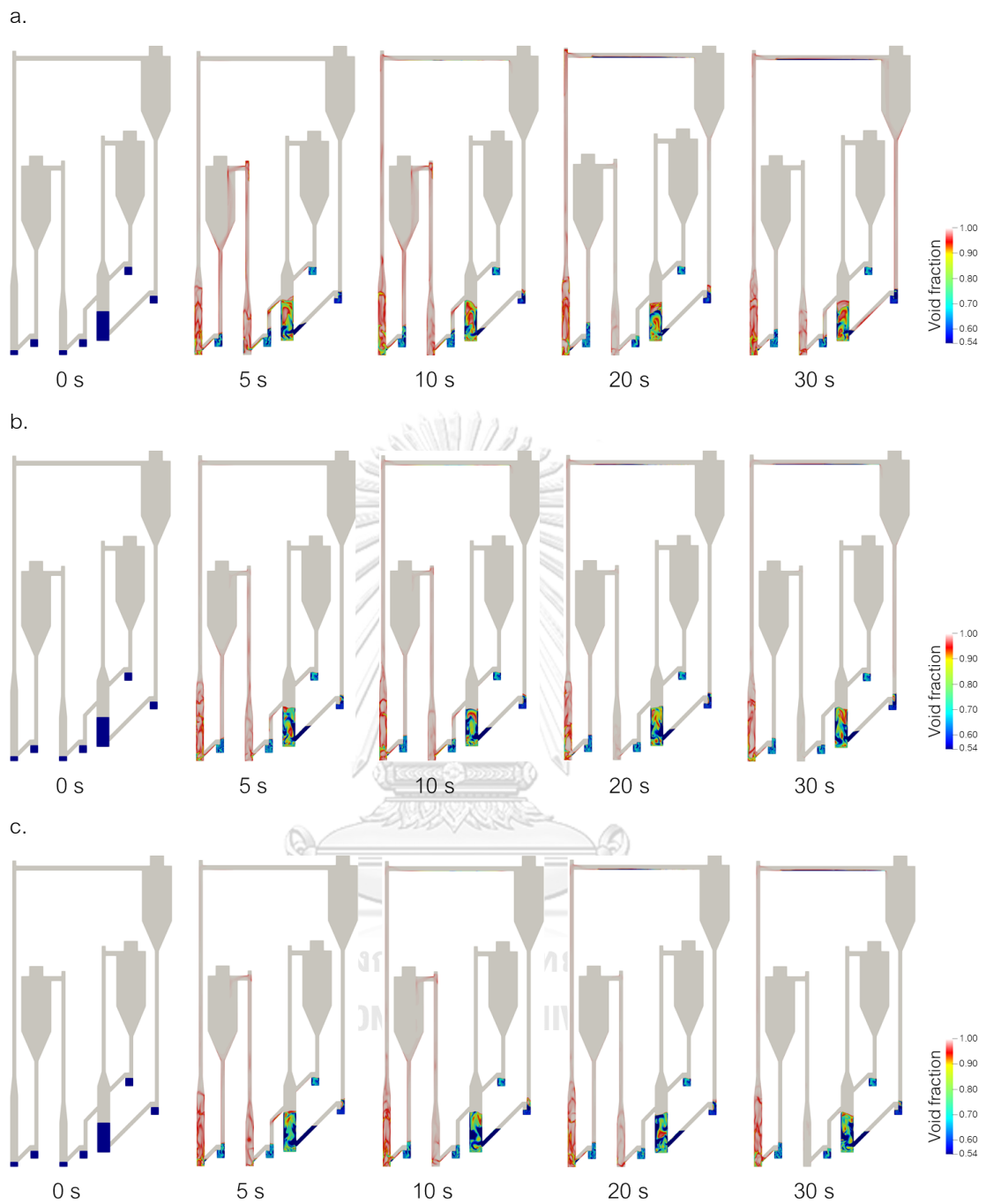


Figure 4.3 Void fraction snapshot of three interconnected fluidized bed reactors at difference coefficient of restitution (COR) a) COR 0.70, b) COR 0.85 and c) COR 0.99

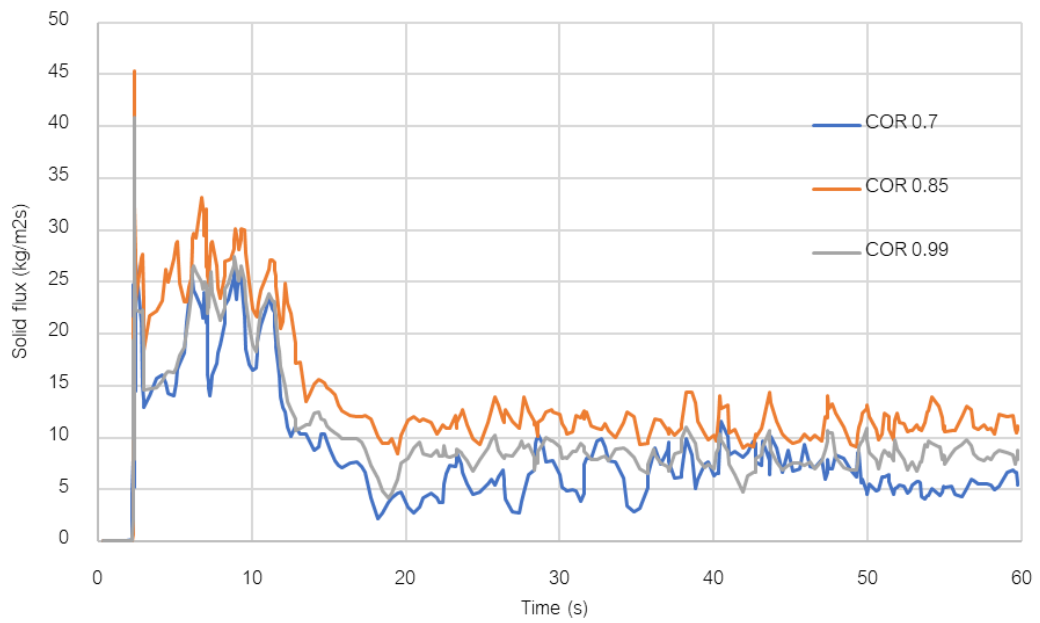


Figure 4.4 Solid flux over simulation time at each coefficient of restitution

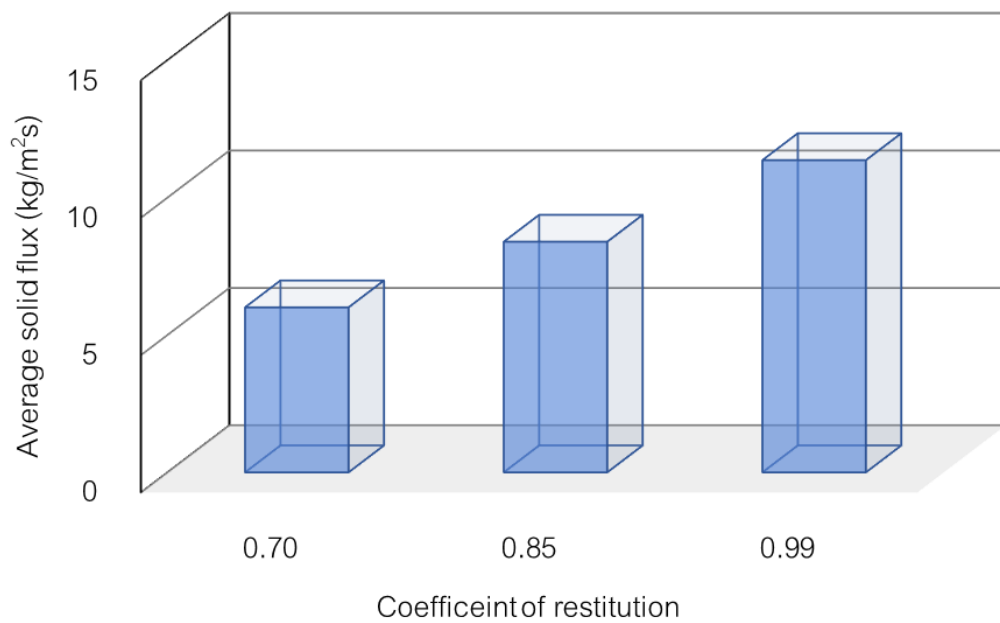


Figure 4.5 The average solid flux of each coefficient of restitution

## 4.2 CFD simulation of internal circulating fluidized bed (ICFB) using DEM approach

### 4.2.1 Grid independency

Three grid size such as coarse, medium and fine was studied according to Table 3.3. The solid volume fraction along the X-axis above the bottom 30 mm is compared in Figure 4.6. The simulation of internal circulating fluidized bed was constructed to demonstrate the effect of coefficient of restitution. Thus, the validation with the experimental result was neglected in this study. The solid volume fraction of the medium grid and the fine grid obtained the consistency of the predicted result. Thus, the medium grid size was selected as the base case for further study.

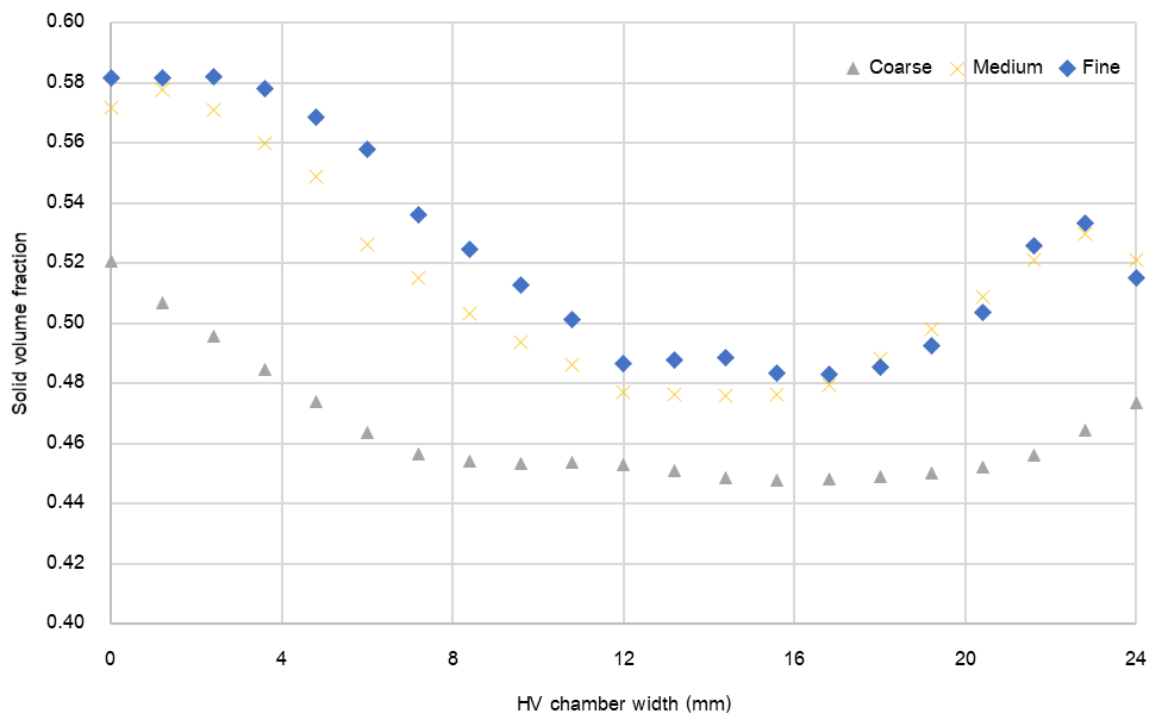


Figure 4.6 The solid volume fraction profile of high velocity (HV) chamber with various grid sizes

#### 4.2.2 The effect of coefficient of restitution on the hydrodynamics profile of internal circulating fluidized bed (ICFB)

The snapshots with the simulation time are displayed in Figure 4.7 and Figure 4.8. Figure 4.7 shows the snapshot of the ICFB with glass bead. Figure 4.8 shows the snapshot of the ICFB with polypropylene. The obtained behaviour was similar. Typically, the solid was initiated to flow up after introducing the gas inlet velocity. The solid particles in HV were moved upward due to the higher gas inlet velocity and overflowed to the LV chamber. After that, the solid particles were accumulated in the LV chamber and pushed the solid particles resulting from the hydrostatic pressure. The solid particle in the LV chamber was moved to the bottom and circulated for the next cycle.

The coefficient of restitution had an effect on the predicted hydrodynamics profile in ICFB simulation. For both cases, more bubble was observed for the ICFB with low coefficient of restitution. The decreasing of the coefficient of restitution enhanced the group of attaching particle and bubble formation which decreased the solid flux as shown in Figure 4.9. The trend was similar to the study from (Luo, Fang, Yang, Zhang, & Fan, 2013). The coefficient of restitution then had the significant for ICFB system which needed to pay attention for choosing the proper coefficient of restitution value.



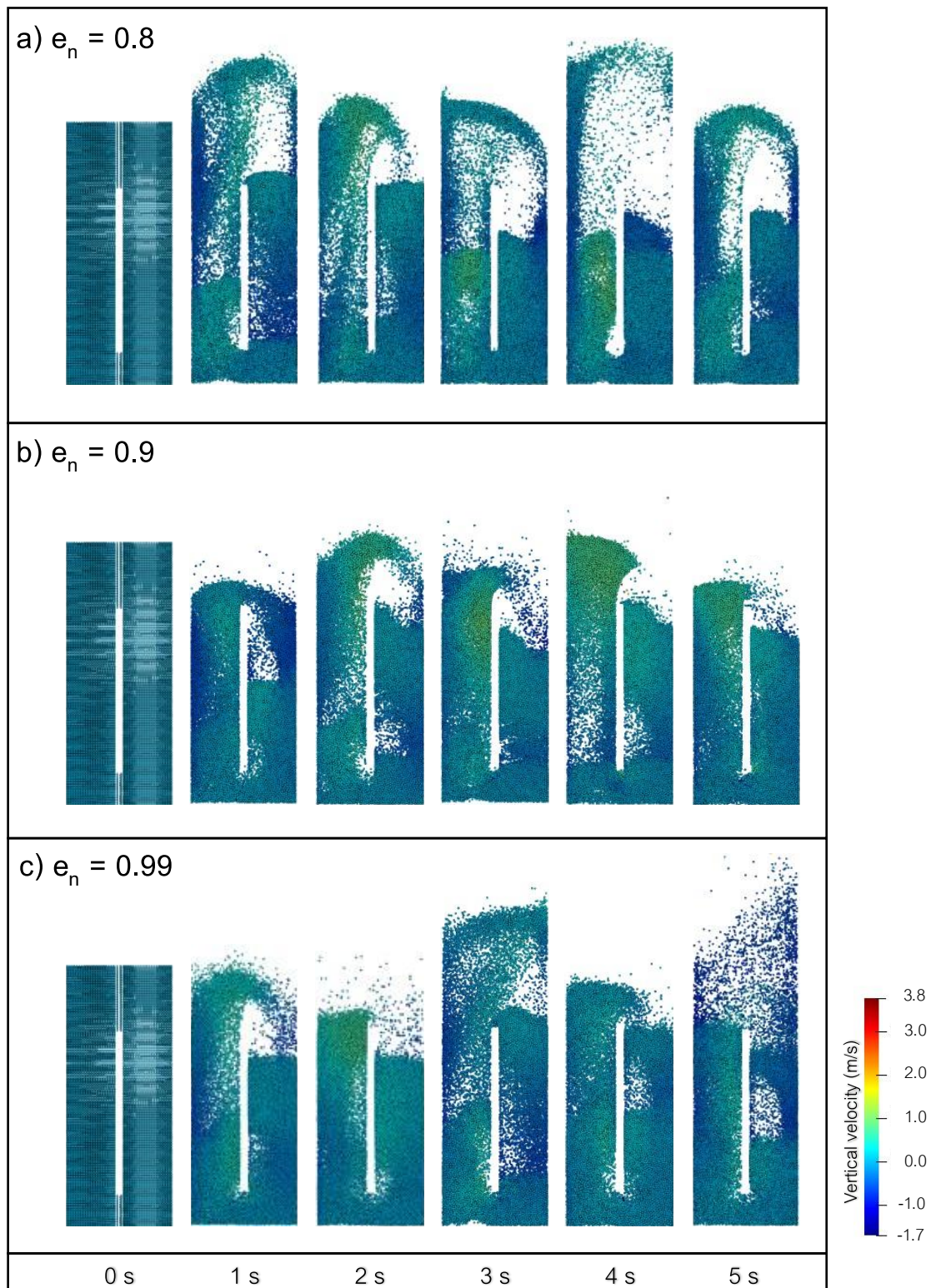


Figure 4.7 The snapshot of glass bead in ICFB model with constant coefficient of restitution ( $e_n$ ): a)  $e_n = 0.8$ , b)  $e_n = 0.9$  and c)  $e_n = 0.99$

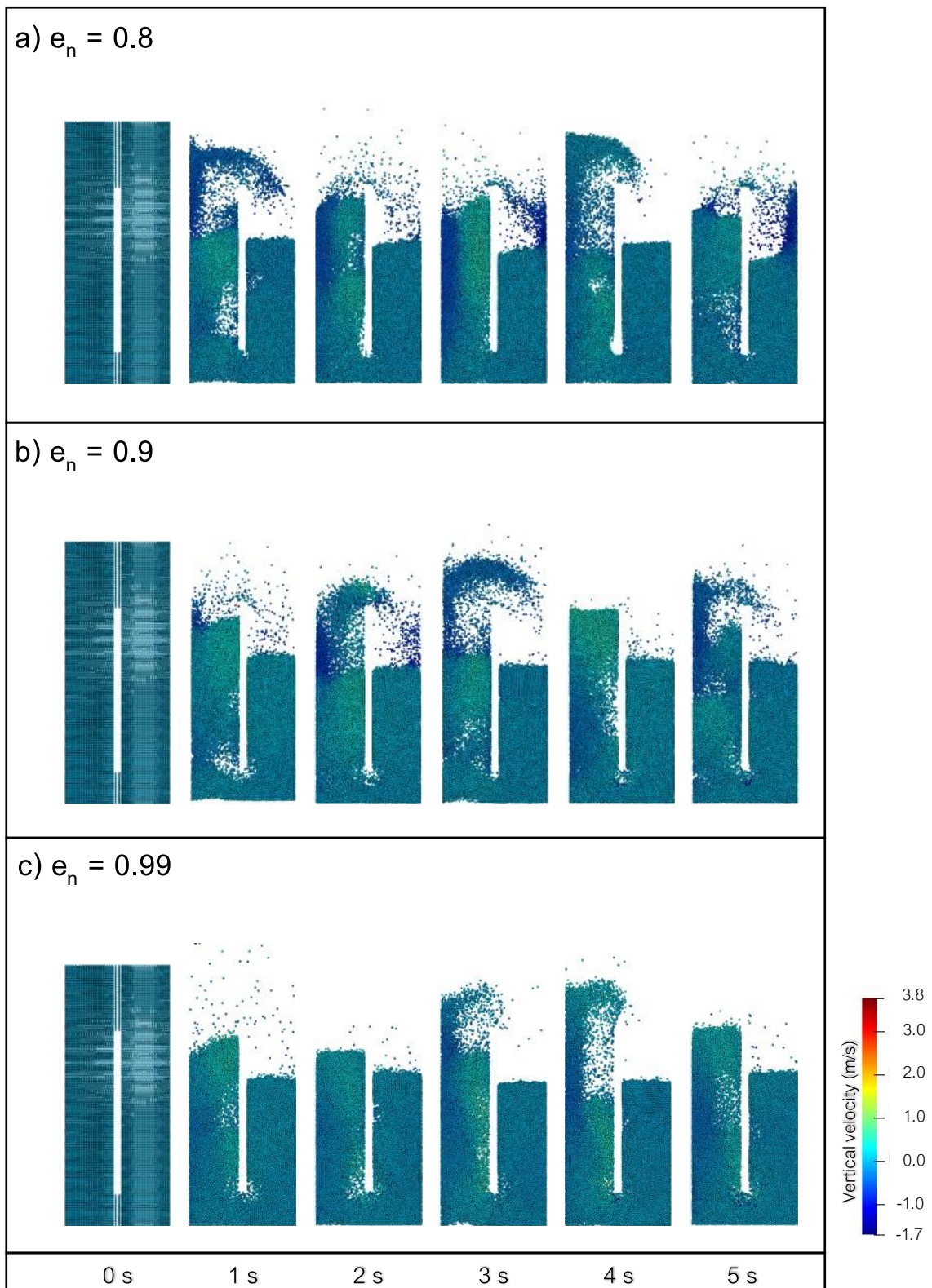


Figure 4.8 The snapshot of polypropylene in ICFB model with constant coefficient of restitution ( $e_n$ ) : a)  $e_n = 0.8$ , b)  $e_n = 0.9$  and c)  $e_n = 0.99$

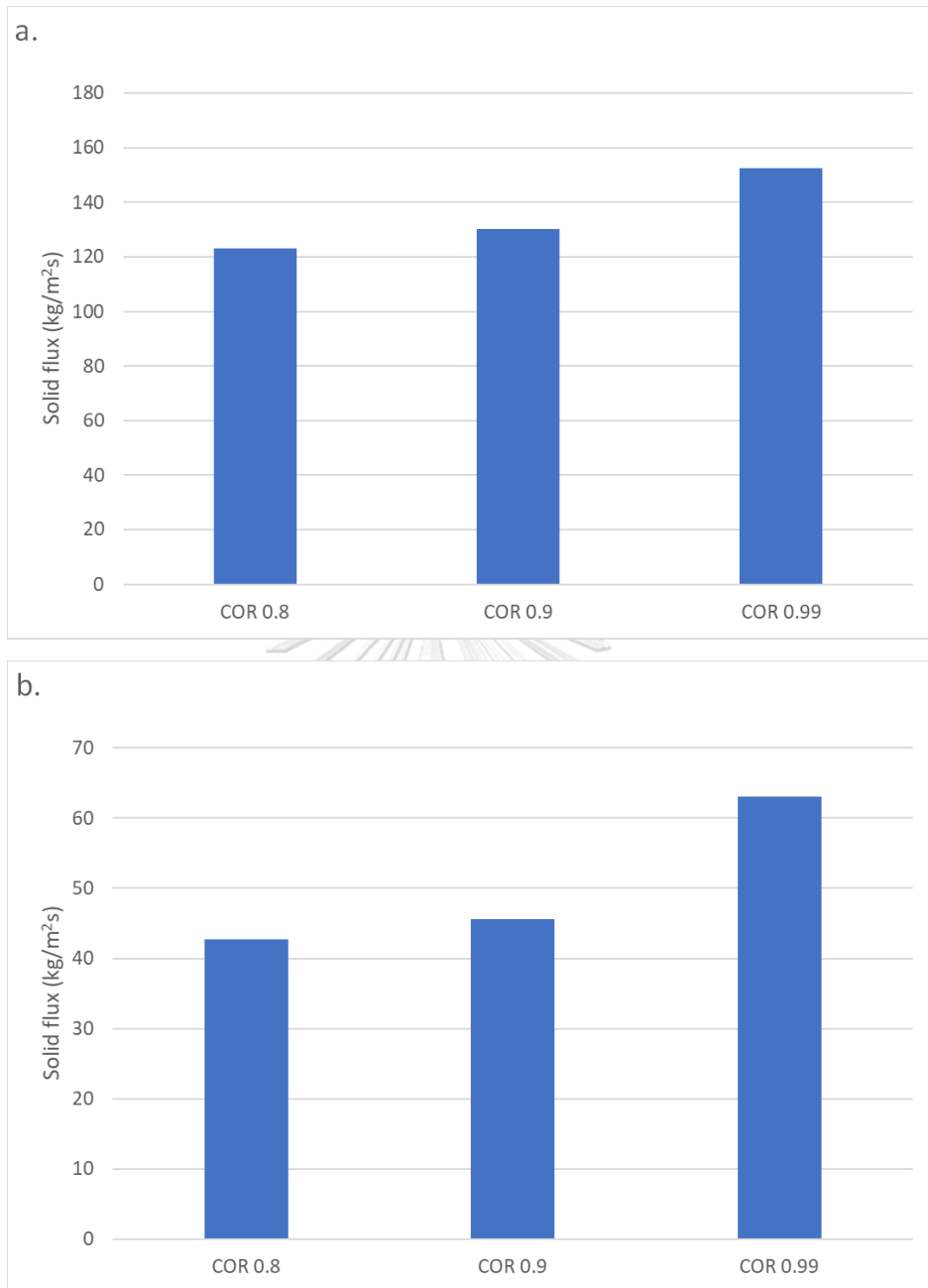


Figure 4.9 The solid flux of ICFB with difference solid materials: a) glass bead and b) polypropylene

### 4.3 CFD simulation of rotating drum using DEM approach

#### 4.3.1 The effect of coefficient of restitution on the hydrodynamics profile of rotating drum

For rotating drum, the DEM simulation was computed only solid phases by the Lagrangian approach. The particle neighbour search algorithm was employed to detect the collision of solid particles. The snapshot contour of the rotating drum at each operating condition is shown in Figure 4.10. It shows the angle of repose and vertical velocity. The results showed that all cases rotated in cascading regime. The evaluation of power draw was used to compare the lifting power in a vertical direction. Figure 4.11 shows that the power draw was increased with the increasing of rotating speed. The increase of rotating speed increased the overall kinetic energy of the system. Moreover, the increase of the coefficient of restitution increased the power draw. The predicted power draw at rotating speed 15 RPM was slightly increased as shown in Figure 4.11a. For 35 RPM, the power draw was sensitive to the coefficient of restitution more than rotating speed 15 RPM as shown in Figure 4.11b and Figure 4.11c, respectively. This is because the high intensity of collision from the particle avalanche is occurred.





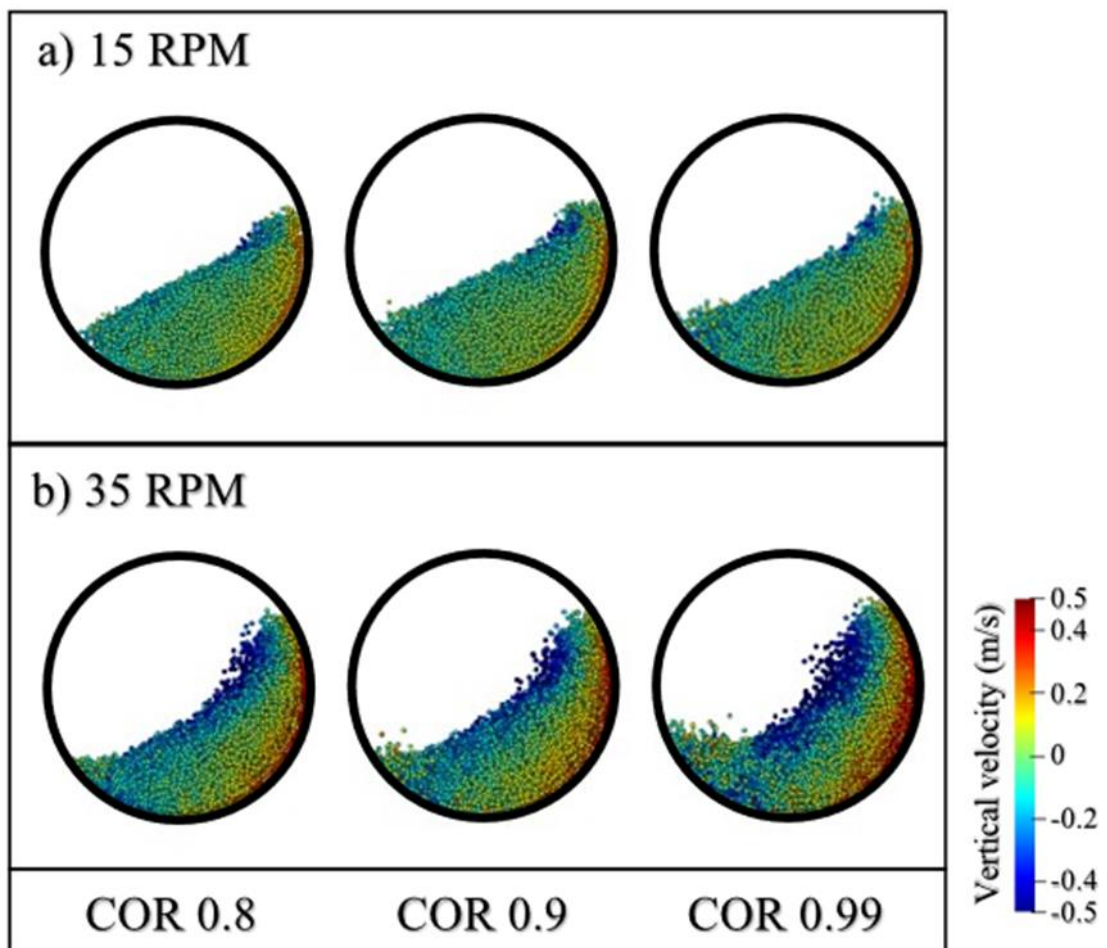
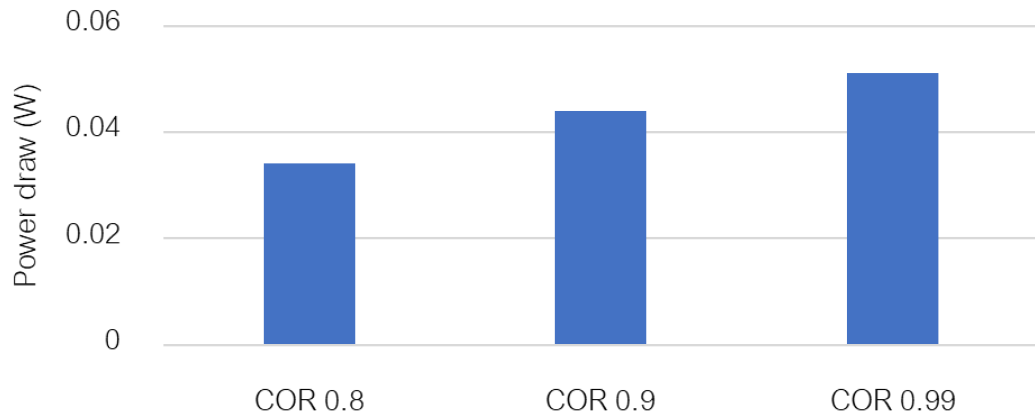


Figure 4.10 The snapshot at 15 s of rotating drum simulation at difference rotating speed and coefficient of restitution approaches with a) 15 RPM and b) 35 RPM

a) 15 RPM



b) 35 RPM

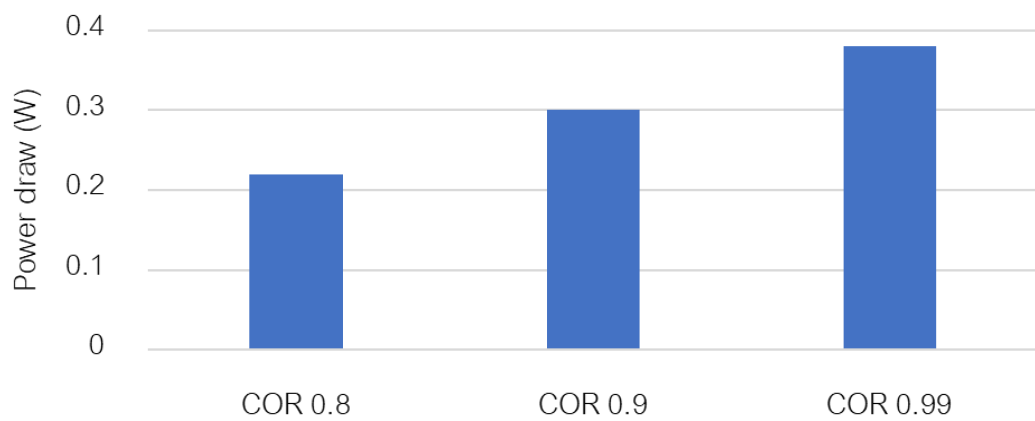


Figure 4.11 The predicted power draw of rotating drum at each operating condition and coefficient of restitution approach with a) 15 RPM and b) 35 RPM

#### 4.4 CFD simulation of the spouted bed using DEM approach

##### 4.4.1 Grid independency test

The spouted bed model was simulated with three different grid quality. There were coarse grid, medium grid and fine grid which contained 26125, 60788 and 119808 cell domains, respectively. The operating condition for grid independency study corresponded to B1 operating condition. For Case B1, the superficial spout velocity was 60 m/s. The background velocity was 2.5 m/s. The solid volume fraction along the reactor height was shown in Figure 4.12. The coarse grid was not sufficient to handle the fluctuation at the bottom which predicted the overestimate of solid volume fraction in contrast with medium grid and fine grid. The medium grid type and fine grid type performed the consistency prediction. Even though the fine grid could be obtained more accurate and fluctuation handleability. But the medium grid was selected in this study due to the sufficient consistency and computational resource.

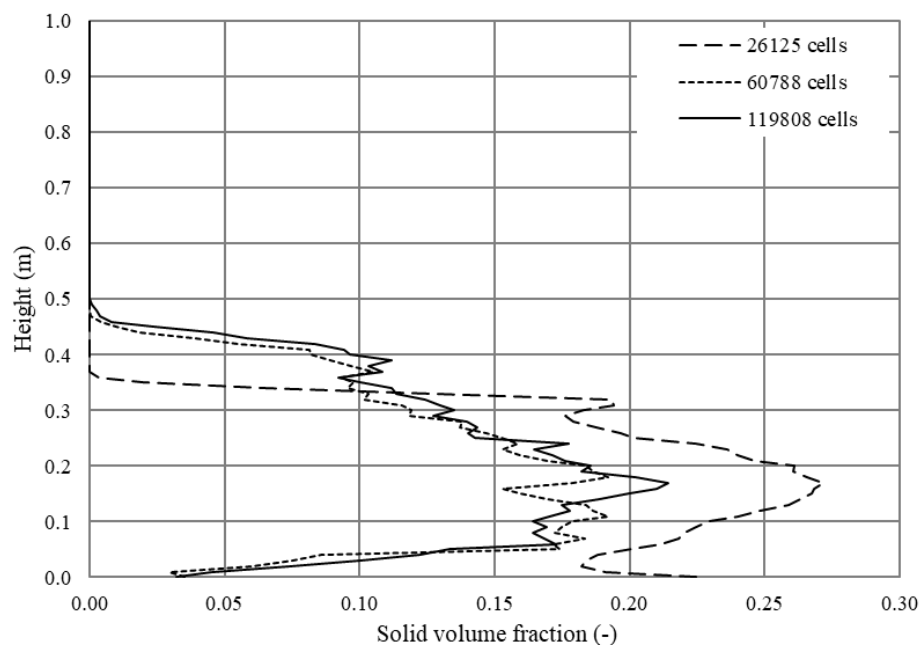


Figure 4.12 The solid volume fraction profile (EPs) along the axial direction with various grid sizes

#### 4.4.2 The effect of coefficient of restitution on the hydrodynamics profile of the spouted bed

The various DEM simulation of spouted bed at difference coefficient of restitution was compared the vertical velocity from the experimental result (Link et al., 2008). The results performed a similar trend as same as the experiment. The snapshot of solid particle movement shows in Figure 4.13. The vertical velocity was high at the center of the chamber due to the major effect from drag force. After the kinetic energy was fully converted to potential energy, the solid particles were fallen to the wall in which the kinetic energy was lost from the collision with a wall and work from friction. The result showed that using low coefficient of restitution decreased bed expansion and higher spout height. The decreasing of the coefficient of restitution was enhanced the attaching of particles in which formulated the void. The bubble accumulation was increased the drag force at the surface while it broke. Thus, it could be observed that the pervading of solid particle was enhanced from the decreasing of the coefficient of restitution. The higher solid vertical velocity was obtained for the simulation using a low coefficient of restitution as shown in Figure 4.14.

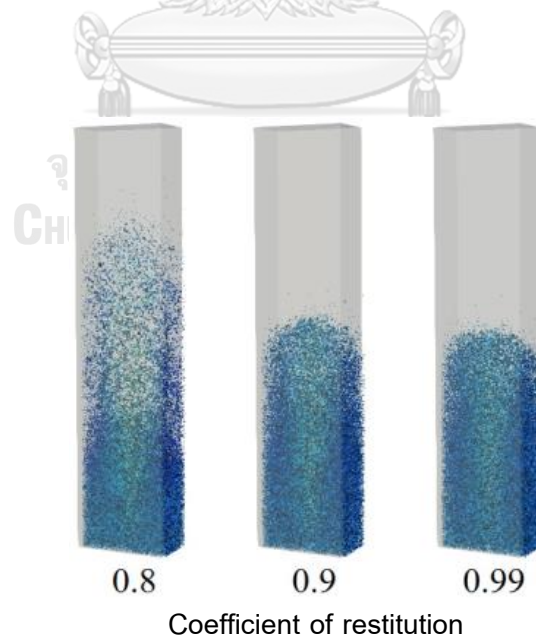


Figure 4.13 Discrete solid particles movement at each coefficient of restitution condition



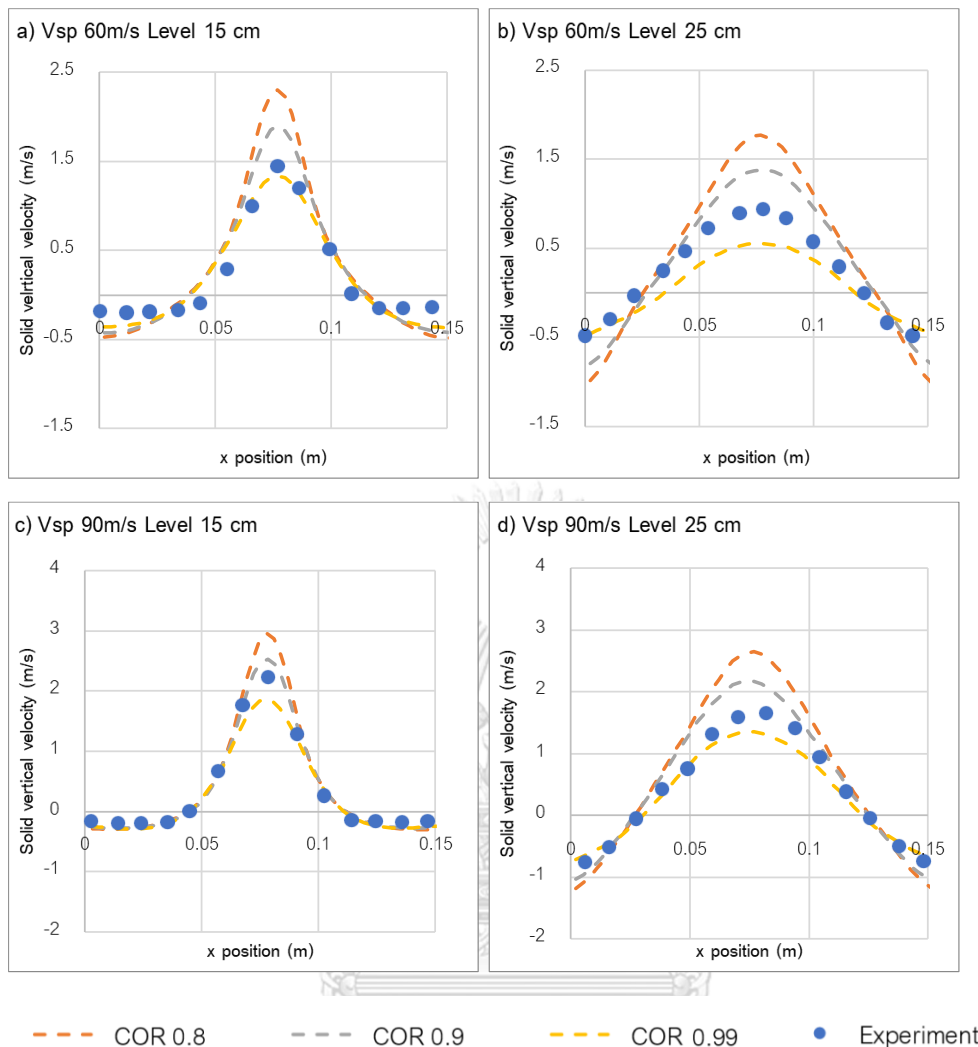


Figure 4.14 The comparison of average solid vertical velocity at each coefficient of restitution approach and experimental results a)  $V_{sp} = 60$  m/s at 15 cm above the bottom, b)  $V_{sp} = 60$  m/s at 25 cm above the bottom, c)  $V_{sp} = 90$  m/s at 15 cm above the bottom and d)  $V_{sp} = 90$  m/s at 25 cm above the bottom

#### 4.5 Conclusion

This section concluded that the coefficient of restitution was played an important role in CFD simulation for both TFM approach and DEM approach. The significant coefficient of restitution became from the ability to maintain the kinetic energy after the collision between solid phase. The decreasing of the coefficient of restitution increased the bubble formation due to the particle attaching and cluster after the collision. The decreasing of the coefficient of restitution was decreased the solid circulation rate for the circulating system such as three interconnected fluidized bed reactors and internal circulating fluidized bed. The local solid accumulation was occurred and packed beside the bubble formation area in which disturbed the solid movement in the system. In addition, the coefficient of restitution had an effect on the individual system such as a rotating drum and spouted bed. The power draw or the energy lifting the solid particle per time was increased with the increasing of the coefficient of restitution. Furthermore, the increase in the coefficient of restitution enhanced the homogenous. It affected the increase of bed expansion and decrease of spout formation in spouted bed simulation. However, the coefficient of restitution was studied by one-factor-at-a-time (OFAT) in this chapter in which limited to discussion the interaction with other contact parameters.

## CHAPTER 5

### Study the effect of contact parameters on CFD-DEM simulation on spouted bed reactor

#### 5.1 Model validation

The simulation results were prior validated with the experimental results from Link et al. (2008) which measured by positron emission particle tracking (PEPT) technique using grid size from the grid independence studied in Chapter 4. The pressure drop across the reactor was plotted to determine the quasi-steady state of the system as shown in Figure 5.1. The high fluctuation happened at first 2.5 s before the system was reaching the quasi-steady state. Thus, the simulation result was the average in the range of 2.5 s to 7.5 s to discard the developing period. The time-averaged vertical velocities of particles of the central XY-plane at 0.15 m and 0.25 m above the bottom were compared with the experimental results as shown in Figure 5.2. A good agreement for both operating condition cases including case B1 and case B2 were obtained. The particles moved upward at high velocity and moved downward at the wall with negative velocity.

The contour plot of the void fraction of the center XY plane is shown in Figure 5.3. In this plot, the void volume fraction is presented by the color bar. Red presents the void area while blue presents the dense solid particle. Figure 5.4 demonstrates the particle flow behaviour by a discrete particle. At the beginning, the solid particles were set the order before moving upward from drag force. The bed was expanded with the void area at the center of the reactor at 0.2 s. The solid particles moved upward and collided with the falling solid particles. After the spouted bed reactor reached the quasi-steady state. The particles were dilute at the center and dense at the wall. The time-averaging of the lateral vertical particle velocity and contour plot void fraction was confirmed the typical hydrodynamics in spouted bed reactor.

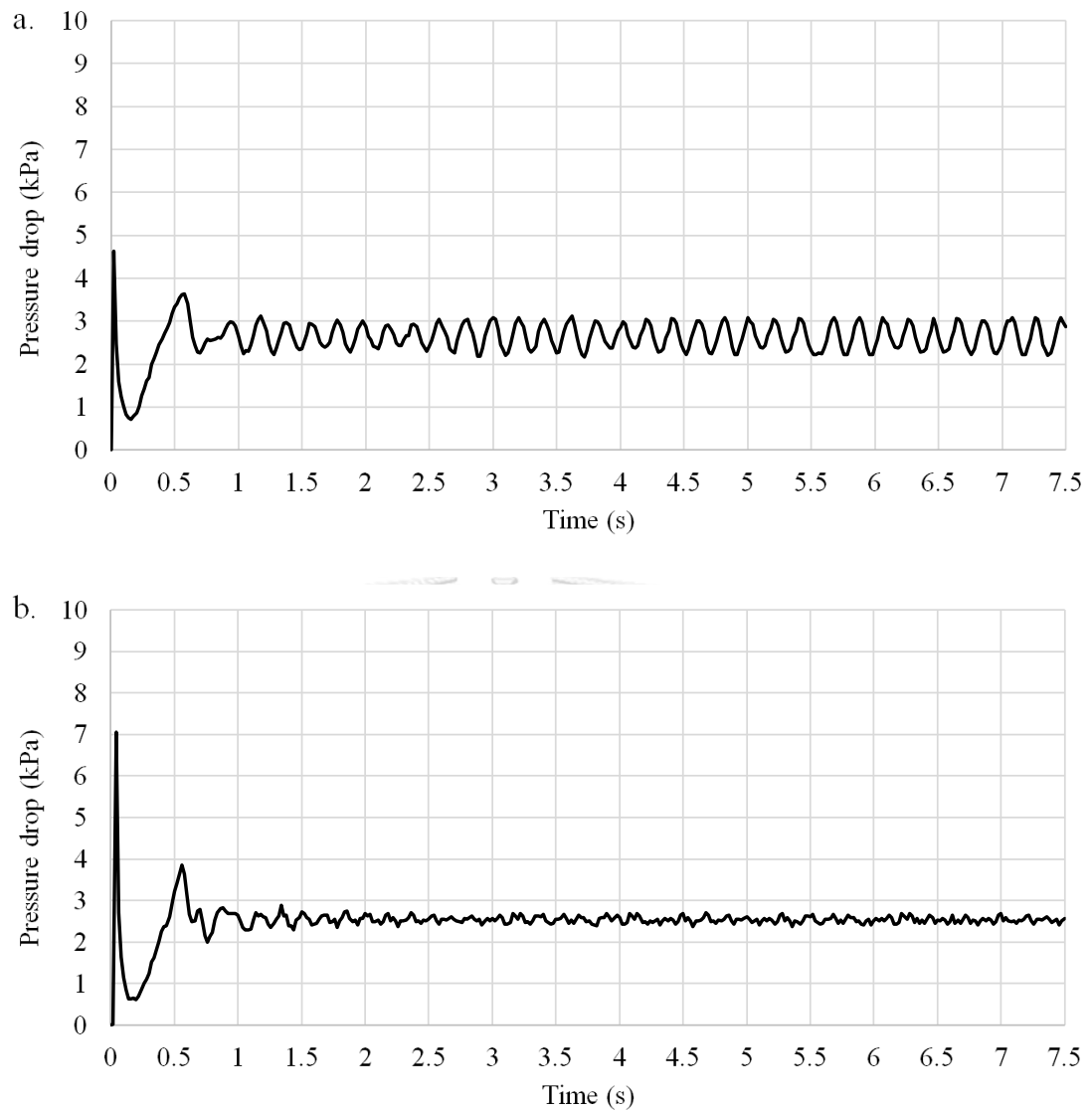


Figure 5.1 a) The pressure drop of the spouted bed reactor for case B1 ( $V_{sp} = 60 \text{ m/s}$ ) and b) the pressure drop of spouted bed reactor for case B2 ( $V_{sp} = 90 \text{ m/s}$ )

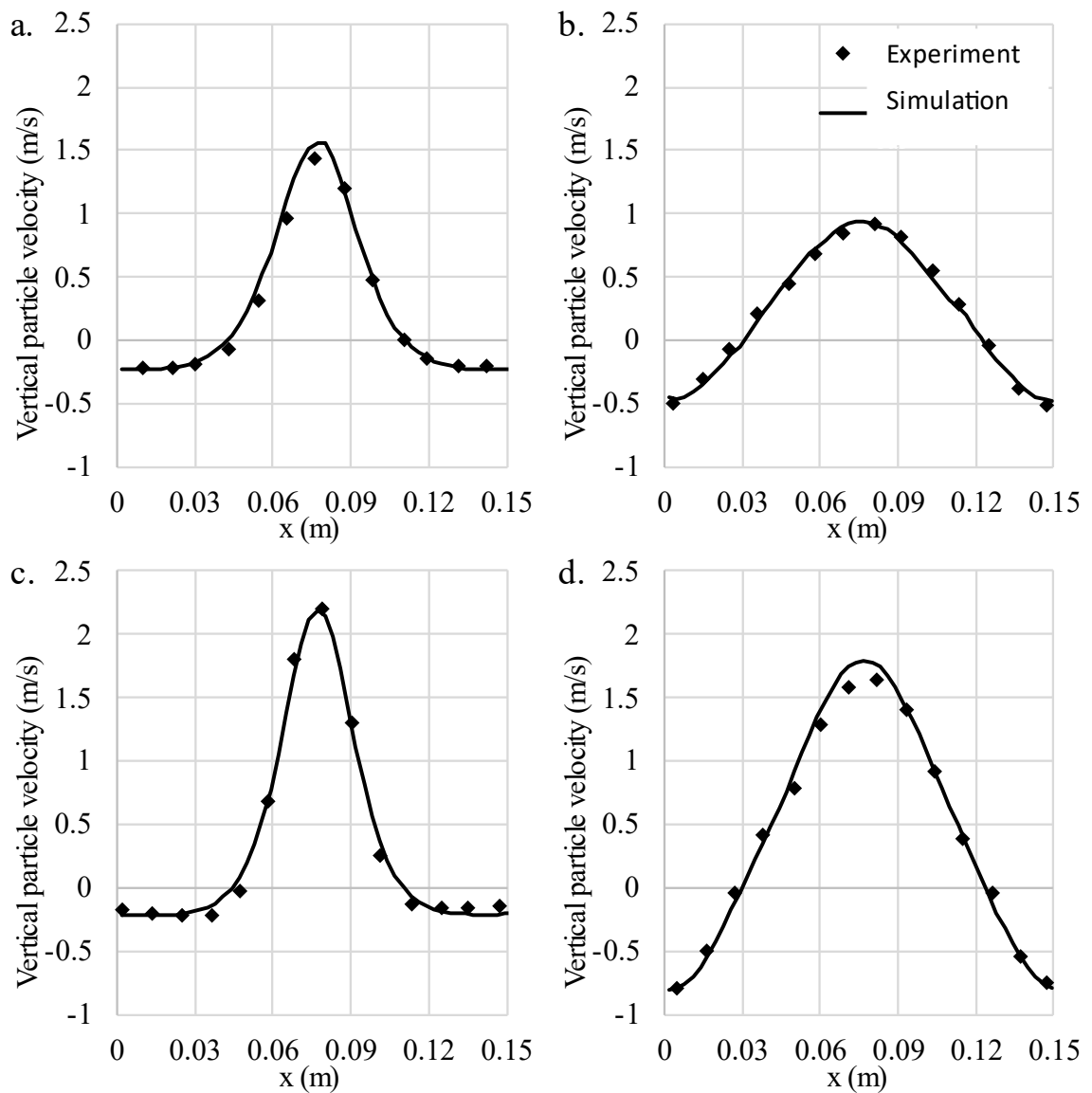


Figure 5.2 Simulation and experimental time-averaging of the lateral vertical particle velocity profile on the central xy-plane at different heights: a)  $V_{sp} = 60$  m/s,  $y = 0.15$  m; b)  $V_{sp} = 60$  m/s,  $y = 0.25$  m; c)  $V_{sp} = 90$  m/s,  $y = 0.15$  m; and d)  $V_{sp} = 90$  m/s,  $y = 0.25$  m

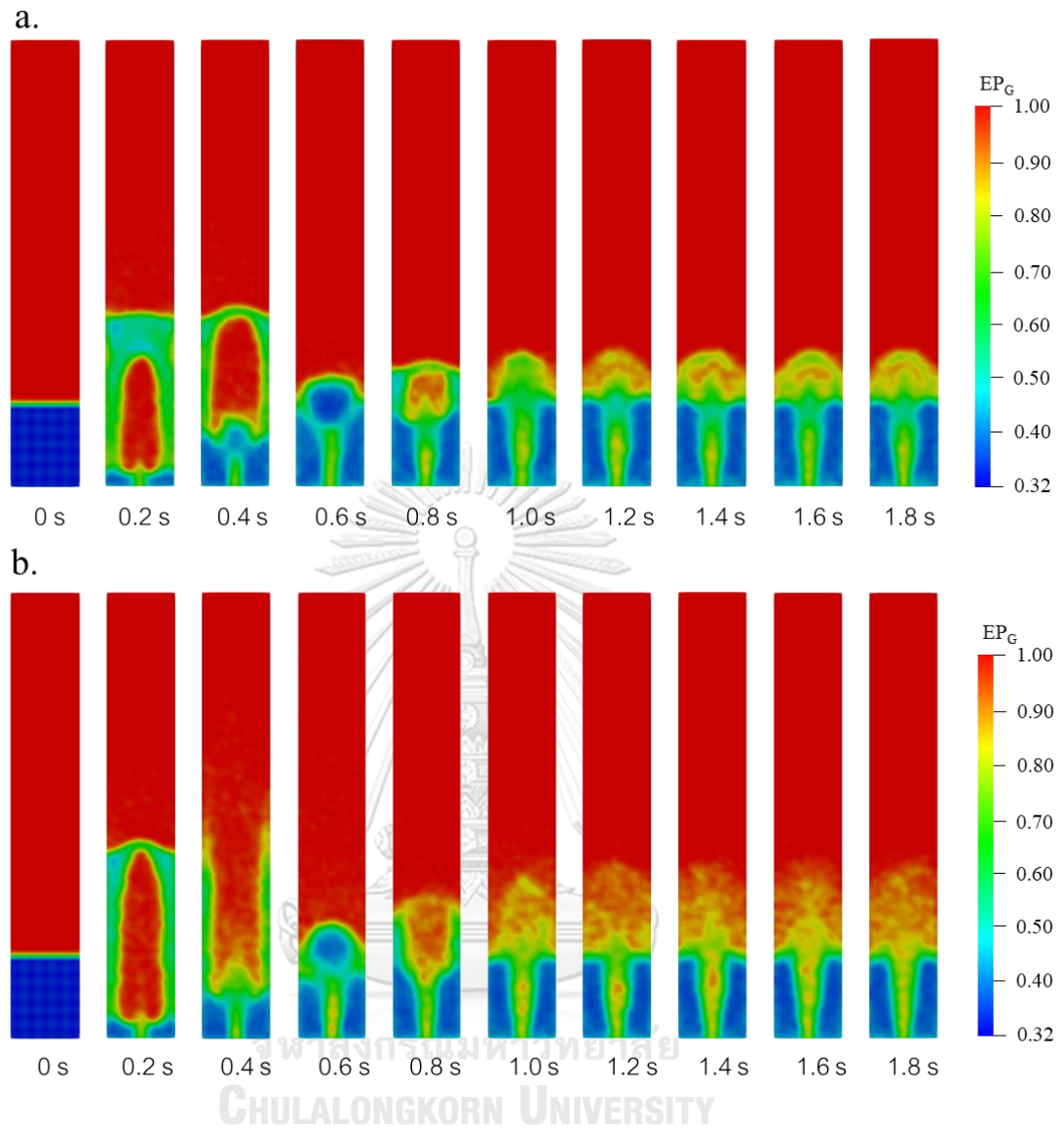


Figure 5.3 Instantaneous contour plots of void fraction on the central xy-plane of the spouted bed reactor of a)  $V_{sp} = 60\text{m/s}$  and b)  $V_{sp} = 90\text{m/s}$

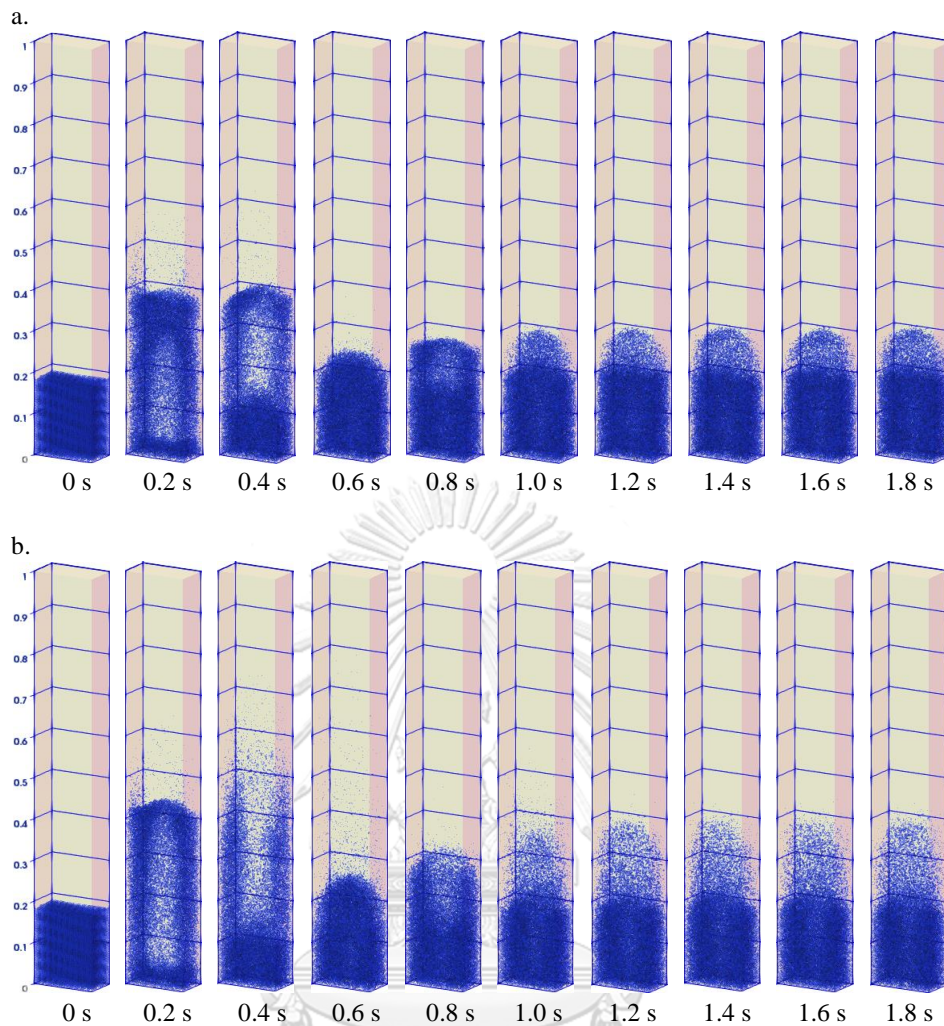


Figure 5.4 The instantaneous particle patterns in the spouted bed reactor of a)  $V_{sp} = 60$  m/s and b)  $V_{sp} = 90$  m/s

## 5.2 The $2^k$ factorial experimental design

The response results are shown in Table 5.1. Only operating condition case B1 was focused in this study. This is because some solid particle was flown out from the boundary in case of B2 with higher spout gas velocity. The similar trend of response parameters between case B1 and case B2 are identified as shown in Table 5.2. Thus, case B1 was selected as a base case simulation in this study which covered all cases of  $2^k$  factorial experimental design.

Table 5.1 Simulation results of case B1 in  $2^k$  factorial experimental design

CASE	CODE					Kinetic energy (J) $\times 10^6$		Bed expansion ratio	Standard deviation of pressure drop (Pa)
	A	B	C	D	E	Translation	Rotational		
1	-1	-1	-1	-1	-1	64.8	0.017	1.37	292.7
2	1	-1	-1	-1	-1	30.2	0.023	1.32	216.4
3	-1	1	-1	-1	-1	37.8	0.017	1.37	322.5
4	1	1	-1	-1	-1	26.0	0.032	1.37	115.8
5	-1	-1	1	-1	-1	64.4	0.017	1.37	214.3
6	1	-1	1	-1	-1	30.3	0.019	1.32	161.0
7	-1	1	1	-1	-1	37.9	0.017	1.37	415.1
8	1	1	1	-1	-1	27.4	0.027	1.32	131.6
9	-1	-1	-1	1	-1	104.4	0.017	1.47	4.9
10	1	-1	-1	1	-1	27.2	0.037	1.32	150.7
11	-1	1	-1	1	-1	729.5	0.017	1.84	3.6
12	1	1	-1	1	-1	43.0	0.095	1.42	28.2
13	-1	-1	1	1	-1	104.4	0.017	1.47	9.4
14	1	-1	1	1	-1	30.0	0.026	1.32	192.2
15	-1	1	1	1	-1	731.2	0.016	1.84	4.5
16	1	1	1	1	-1	28.5	0.060	1.37	46.1
17	-1	-1	-1	-1	1	63.6	0.017	1.37	321.1
18	1	-1	-1	-1	1	32.3	0.021	1.32	243.8
19	-1	1	-1	-1	1	38.6	0.017	1.37	449.1
20	1	1	-1	-1	1	28.1	0.027	1.37	127.1
21	-1	-1	1	-1	1	64.4	0.017	1.37	245.0
22	1	-1	1	-1	1	30.6	0.020	1.32	245.6
23	-1	1	1	-1	1	37.9	0.017	1.37	430.0
24	1	1	1	-1	1	27.0	0.027	1.32	117.7
25	-1	-1	-1	1	1	104.2	0.017	1.47	6.3
26	1	-1	-1	1	1	22.8	0.059	1.37	94.7
27	-1	1	-1	1	1	731.4	0.018	1.84	3.4
28	1	1	-1	1	1	111.1	0.173	1.53	17.9
29	-1	-1	1	1	1	104.6	0.017	1.47	6.2
30	1	-1	1	1	1	29.2	0.027	1.32	213.9
31	-1	1	1	1	1	730.8	0.016	1.84	3.5
32	1	1	1	1	1	27.5	0.063	1.37	35.7



Table 5.2 The results using B2 operating condition

CASE	CODE					B2			
						Kinetic energy (J) $\times 10^{-6}$		Bed expansion ratio	Standard deviation of pressure drop (Pa)
	A	B	C	D	E	Translation	Rotational		
1	-1	-1	-1	-1	-1	83.24	0.013	1.56	239.4
2	1	-1	-1	-1	-1	41.43	0.024	1.52	170.3
3	-1	1	-1	-1	-1	38.44	0.012	1.57	260.7
5	-1	-1	1	-1	-1	82.02	0.013	1.56	163.8
9	-1	-1	-1	1	-1	128.47	0.012	1.69	5.1
17	-1	-1	-1	-1	1	81.00	0.013	1.55	280.1

### 5.2.1 Effect of contact force modeling parameters on kinetic energy

The kinetic energy is typically lost during the collision due to the inelasticity and friction in which effected to the hydrodynamics behaviour. The average translational kinetic energy ( $KE_{\text{Translation}}$ ) and rotational kinetic energy ( $KE_{\text{Rotational}}$ ) were computed. The ANOVA analysis of  $KE_{\text{Translation}}$  is shown in Table 5.3. It showed that the particle-particle friction coefficient (A), spring constant (B), and normal particle-particle restitution coefficient (D) were significant individual factors. Moreover, the significant interaction factors on  $KE_{\text{Translation}}$  were AB, AD, BD and ABD. The main effect plot of  $KE_{\text{Translation}}$  is shown in Figure 5.5. It supported that the significant order was  $A > D > B$ . The negative effect on  $KE_{\text{Translation}}$  was caused by the increasing of particle-particle friction coefficient (A). In contrast, the positive effect on  $KE_{\text{Translation}}$  was caused by the increasing of the spring constant (B) and normal particle-particle restitution coefficient (D). The increasing of the particle-particle friction coefficient (A) raised the  $KE_{\text{Rotational}}$  and reduced the  $KE_{\text{Translation}}$ . It enhanced the friction force acting at the contact point in the tangential direction. The

spring constant (B) and normal restitution coefficient (D) were the contact parameters which represented the elastic collision ability in a linear direction. The interaction of two-factor of  $KE_{\text{Translation}}$  is shown in Figure 5.6. The results showed that the AB and AD interaction obtained the same trends of considered (x-axis) factor for both low and high values of the other factors. However, the BD interaction obtained the opposite trend of considered (x-axis) factor for low and high levels the other factor. AD interaction was the most significant interaction term which obtained similar trend with their main effects as discussed above.

Table 5.3 ANOVA analysis of translation kinetic energy

Source	Sum of squares	df	Mean squares	F-value	p-value
Model	1.64E-06	7	2.35E-07	1182.6	7.11E-29
A-A	3.20E-07	1	3.20E-07	1609.7	1.64E-23
B-B	1.93E-07	1	1.93E-07	972.5	6.21E-21
D-D	2.85E-07	1	2.85E-07	1433.4	6.46E-23
AB	1.67E-07	1	1.67E-07	842.3	3.34E-20
AD	2.53E-07	1	2.53E-07	1272.5	2.63E-22
BD	2.32E-07	1	2.32E-07	1169.3	7.13E-22
ABD	1.94E-07	1	1.94E-07	978.8	5.75E-21
Residual	4.77E-09	24	1.99E-10		
Cor Total	1.65E-06	31			
$R^2$	0.997				

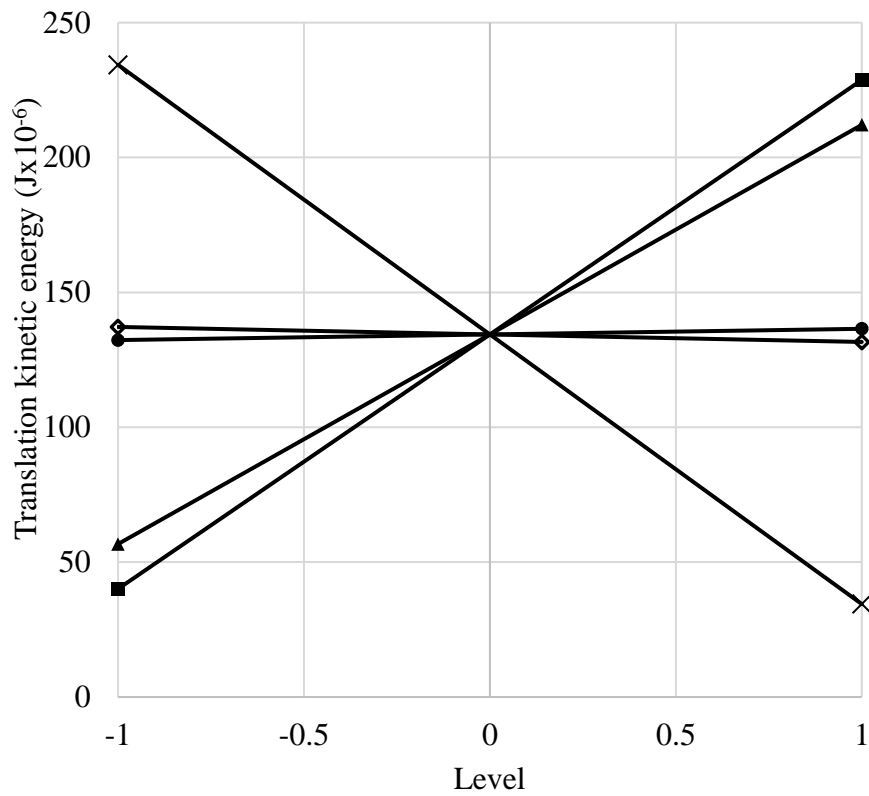


Figure 5.5 The main effect plot of translational kinetic energy

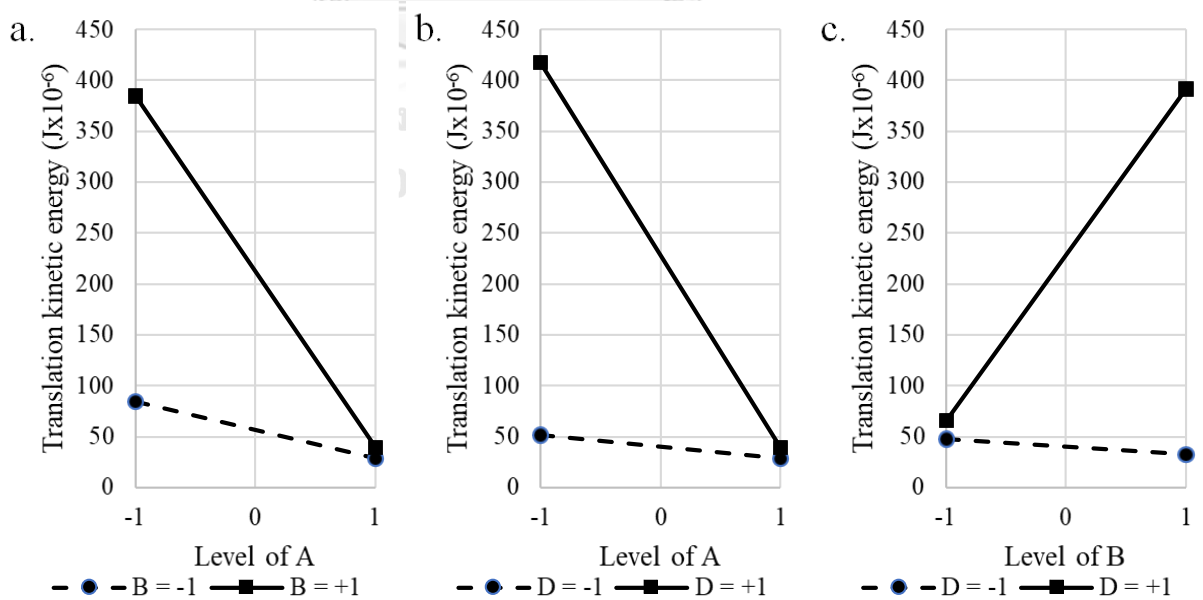


Figure 5.6 The interaction effect plot of the translational kinetic energy of a) AB, b) AD and c) BD

The ANOVA analysis of the  $KE_{\text{Rotational}}$  response is shown in Table 5.4. The result showed the significant main effects on  $KE_{\text{Rotational}}$  such as the particle-particle friction coefficient (A), spring constant (B), the ratio of the tangential spring constant to normal spring constant (C), normal particle-particle restitution coefficient (D), and tangential particle-particle restitution coefficient (E). The significant interaction parameters were AB, AC, AD, AE, BD, CD, CE, DE, ABD, ACD, ACE, ADE, CDE, and ACDE interactions. The significant order of the main effect was  $A > D > B > C > E$  as shown in Figure 5.7. The particle-particle friction coefficient (A), spring constant (B) and normal particle-particle restitution coefficient (D) achieved a positive effect on the  $KE_{\text{Rotational}}$ . In contrast, the normal spring constant (C) had a negative effect on the  $KE_{\text{Rotational}}$ . This is because the increase of elastic contact parameters such as the spring constant (B), normal particle-particle restitution coefficient (D), and tangential particle-particle restitution coefficient (E) were reduced the kinetic energy loss both direction after the contact (Jiménez & Bermúdez, 2011; Johnson, 1985b; O'Sullivan, 2014). The collision treating in stick region with the friction force was higher than the magnitude of tangential contact force (Ciavarella, 2015) resulting in the particle deformation. The remaining region was a slip collision that the collision followed by the perform of normal contact force and therefore the friction constant. It could be concluded that the deformation in the sticky region happened from the increasing of the particle-particle friction coefficient (A) and the decreasing of increasing the ratio of the tangential spring constant to the normal spring constant (C) which reduced the  $KE_{\text{Rotational}}$ . The interaction effect plots of  $KE_{\text{Rotational}}$  was shown in Figure 5.8. The similar trends of considered (x-axis) factor for both the low and high levels of the other factor was observed. The AD interaction also was the most significant interaction term in which achieved a similar trend as same as the main effect of A and D.

Table 5.4 ANOVA analysis of rotational kinetic energy

Source	Sum of squares	df	Mean squares	F-value	p-value
Model	10.60	19	5.58E-01	297.2	3.49E-13
A-A	4.74	1	4.74E+00	2522.1	2.55E-15
B-B	0.71	1	7.09E-01	377.8	1.95E-10
C-C	0.30	1	2.98E-01	158.6	2.82E-08
D-D	1.31	1	1.31E+00	697.9	5.30E-12
E-E	0.03	1	2.50E-02	13.3	3.32E-03
AB	0.79	1	7.87E-01	419.2	1.06E-10
AC	0.24	1	2.45E-01	130.4	8.38E-08
AD	1.50	1	1.50E+00	796.9	2.42E-12
AE	0.02	1	2.44E-02	13.0	3.60E-03
BD	0.19	1	1.93E-01	102.6	3.11E-07
CD	0.18	1	1.83E-01	97.6	4.08E-07
CE	0.02	1	1.81E-02	9.7	9.07E-03
DE	0.05	1	5.48E-02	29.2	1.60E-04
ABD	0.20	1	2.03E-01	108.3	2.32E-07
ACD	0.14	1	1.43E-01	75.9	1.56E-06
ACE	0.01	1	1.05E-02	5.6	3.57E-02
ADE	0.05	1	5.36E-02	28.5	1.76E-04
CDE	0.06	1	6.37E-02	33.9	8.15E-05
ACDE	0.05	1	4.85E-02	25.8	2.70E-04
Residual	0.02	12	1.88E-03		
Cor Total	10.63	31			
R <sup>2</sup>	0.998				

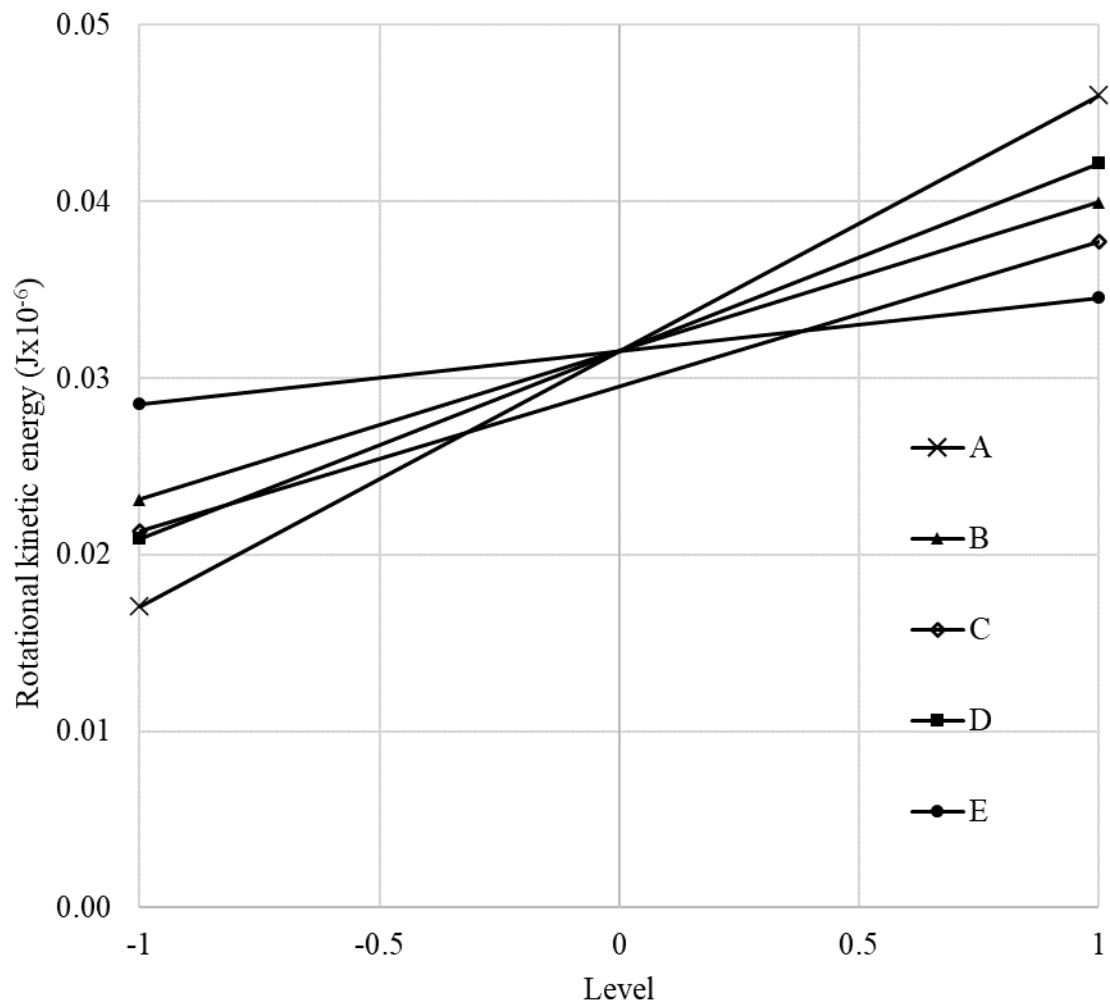


Figure 5.7 The main effect plot of rotational kinetic energy

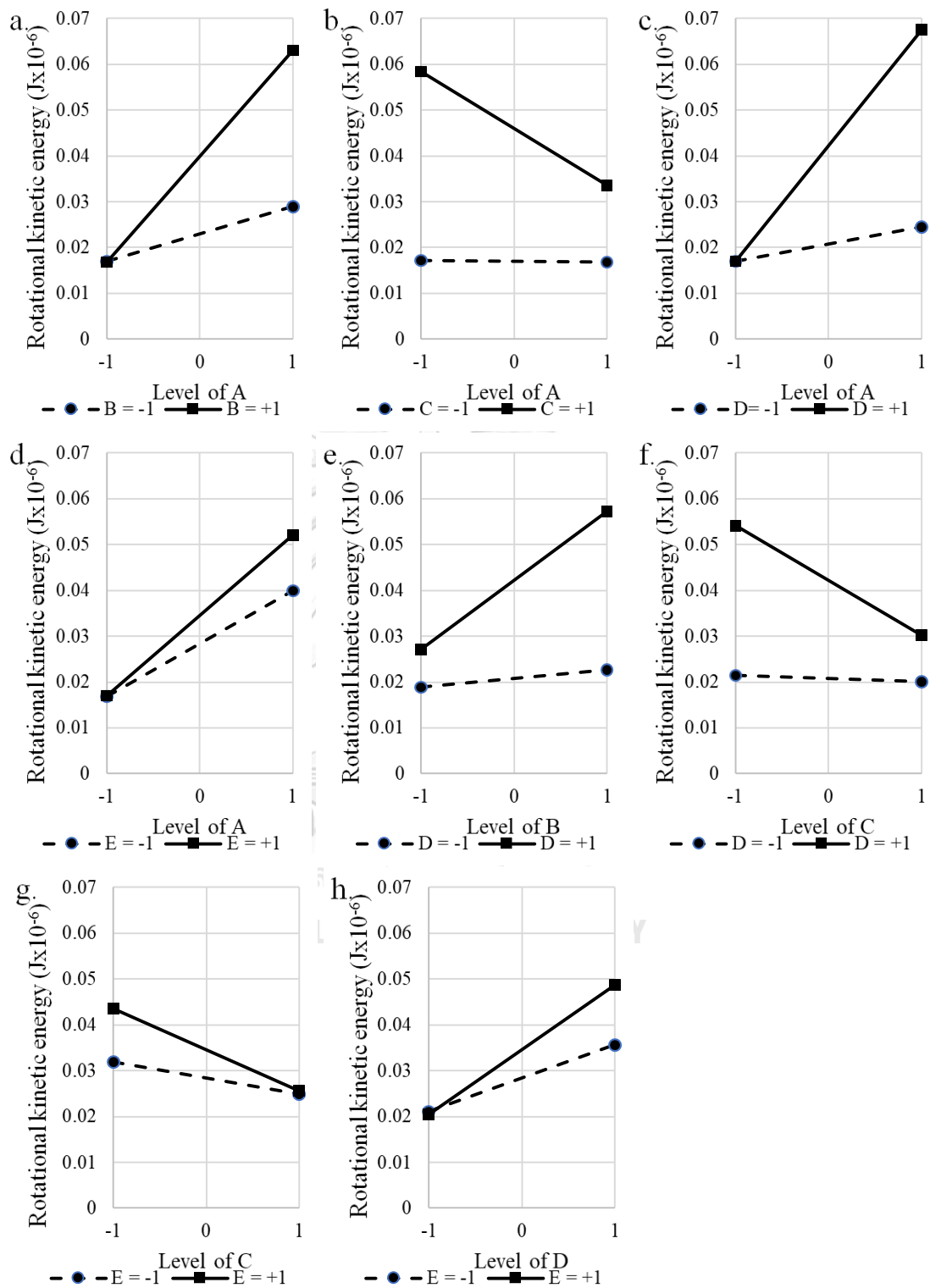


Figure 5.8 The interaction effect plot of the rotational kinetic energy of a) AB, b) AC, c) AD, d) AE, e) BD, f) CD, g) CE and h) DE

### 5.2.2 Effect of contact force modeling parameters on the bed expansion ratio

The hydrodynamics parameter for characterize the fluidization behaviour usually used the bed expansion ratio. Basically, the bed expansion ratio was increased with the increasing of superficial gas velocity (Y. Zhang et al., 2015). It was related to the kinetic energy of the particles. The ANOVA analysis of bed expansion ratio of the contact modeling parameters is shown in Table 5. 5. It justified that the particle–particle friction coefficient (A), spring constant (B), ratio of the tangential spring constant to the normal spring constant (C), and normal (particle–particle) restitution coefficient (D) had the significant on bed expansion ratio with an order  $D > A > B > C$ . The main effect plots are shown in Figure 5.9. The significant interaction effects were AB, AC, AD, BC, BD, ABC, and ABD. The positive effect on bed expansion ratio was resulted from the increasing of B and D. The increasing of A and C resulted the negative effect on bed expansion ratio. E had little influence on bed expansion ratio. The linear velocity was increased from the increasing of the spring constant (B) and normal (particle–particle) restitution coefficient (D). The vertical motion was the major direction of spouted bed system. In the opposite, the rotational kinetic energy was enhanced by the increasing of the particle–particle friction coefficient (A) and the ratio of the tangential spring constant to the normal spring constant (C). This is because the rotation kinetic energy reduced the linear kinetic energy from the conservative of kinetic energy which was the major main energy that resulted the higher bed expansion. Figure 5.10 shows the two-factor interaction effect plots of bed expansion ratio. The similar trend of considered (x-axis) factor demonstrated both low and high values of the other factors for all interaction factors. The AD interaction played an important role with had the same trend as their main effects.

The averaged solid volume fraction on the horizontal plane is shown in Figure 5.11. The dispersion profiles were classified into two groups, A and B, which are shown in



Figure 5.11a and Figure 5.11b, respectively. The x-axis is the height from the bottom (x-axis) and y-axis is the solid volume fraction. The S-curve pattern was obtained which was dense at bottom and dilute at the upper zone. For group A, the solid volume fraction at the bottom of reactor was higher than the solid volume fraction at the bottom of group B. The average solid volume fraction of group A was 0.5 while group B was 0.3. The slope between the solid volume fraction and height was differenced. Group A obtained sharply decreased of solid volume fraction at 15-25 cm from the bottom and reached the unity at about 35 cm from the bottom. The slope between solid volume fraction and height was dramatically decreased at 20-40 cm from the bottom. The solid volume was decreased to unity at the height above 65 cm from the bottom. The average solid volume fraction at the center xy plane of group A was presented by case 23 and group B was presented by case 27 as can be seen in the Figure 5.12. The spouted bubble was observed near as the bottom and the center of reactor for group A which is commonly phenomenon of spouted bed reactor. In the opposite, the non-conventional behaviour was happened for group B operating condition. The dispersion gradient without spouted bubble was obtained. The group B consisted of cases 11, 15, 27 and 35. The common operating conditions for those 4 cases were low level of solid particle-solid particle friction coefficient (A) at  $1.00e-5$ , the high level for the spring constant (B) at 2000 N/m and high level for normal solid particle-solid particle restitution coefficient (D) at 0.98. The overpredicted  $KE_{\text{Translation}}$  was obtained from the unrealistic elastic collision and free slip collision at the surface of the particles.

Table 5. 5 ANOVA analysis of bed expansion ratio

Source	Sum of squares	df	Mean squares	F-value	p-value
Model	0.85	11	7.76E-02	179.4	1.75E-17
A-A	0.21	1	2.08E-01	480.2	1.87E-15
B-B	0.12	1	1.19E-01	273.8	3.89E-13
C-C	0.00	1	4.24E-03	9.8	5.27E-03
D-D	0.23	1	2.25E-01	520.2	8.67E-16
AB	0.03	1	3.12E-02	72.2	4.54E-08
AC	0.00	1	4.24E-03	9.8	5.27E-03
AD	0.12	1	1.19E-01	273.8	3.89E-13
BC	0.00	1	2.16E-03	5	3.69E-02
BD	0.09	1	9.43E-02	217.8	3.25E-12
ABC	0.00	1	2.16E-03	5	3.69E-02
ABD	0.05	1	4.58E-02	105.8	1.97E-09
Residual	0.01	20	4.33E-04		
Cor Total	0.86	31			
R <sup>2</sup>	0.990				

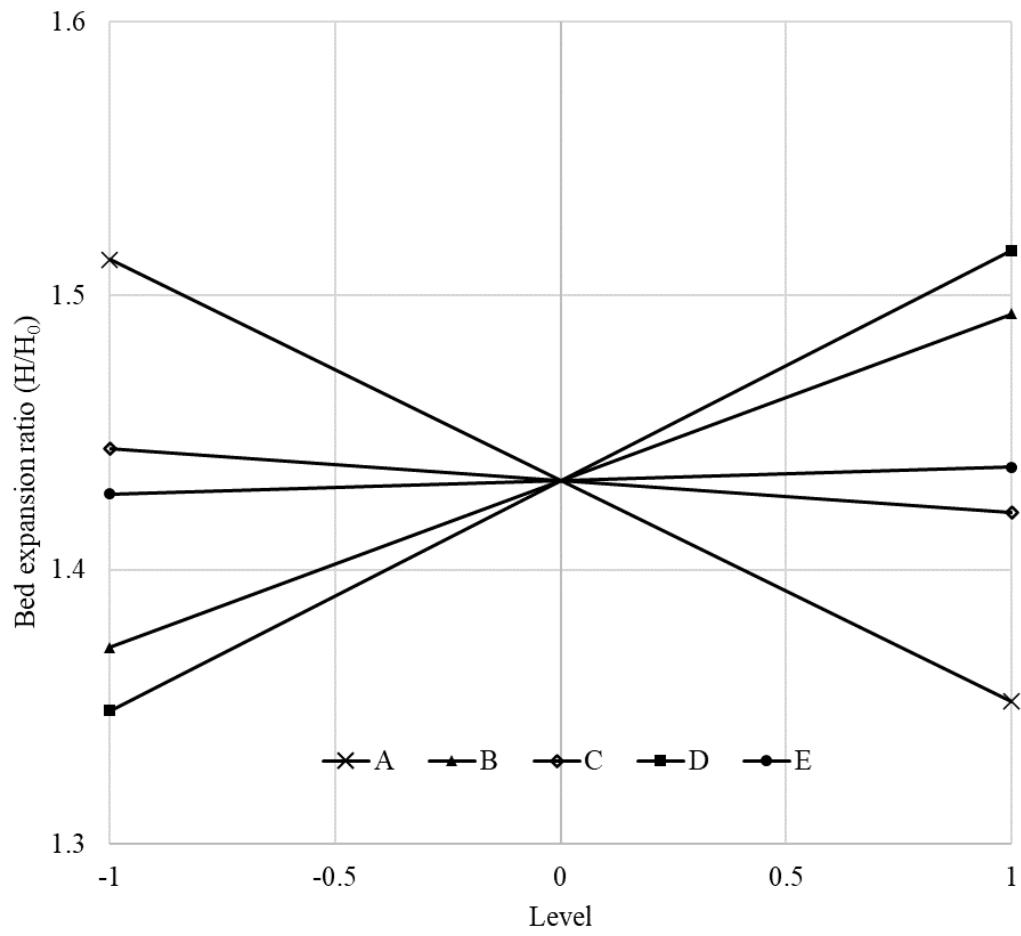


Figure 5.9 The main effect plot of bed expansion ratio

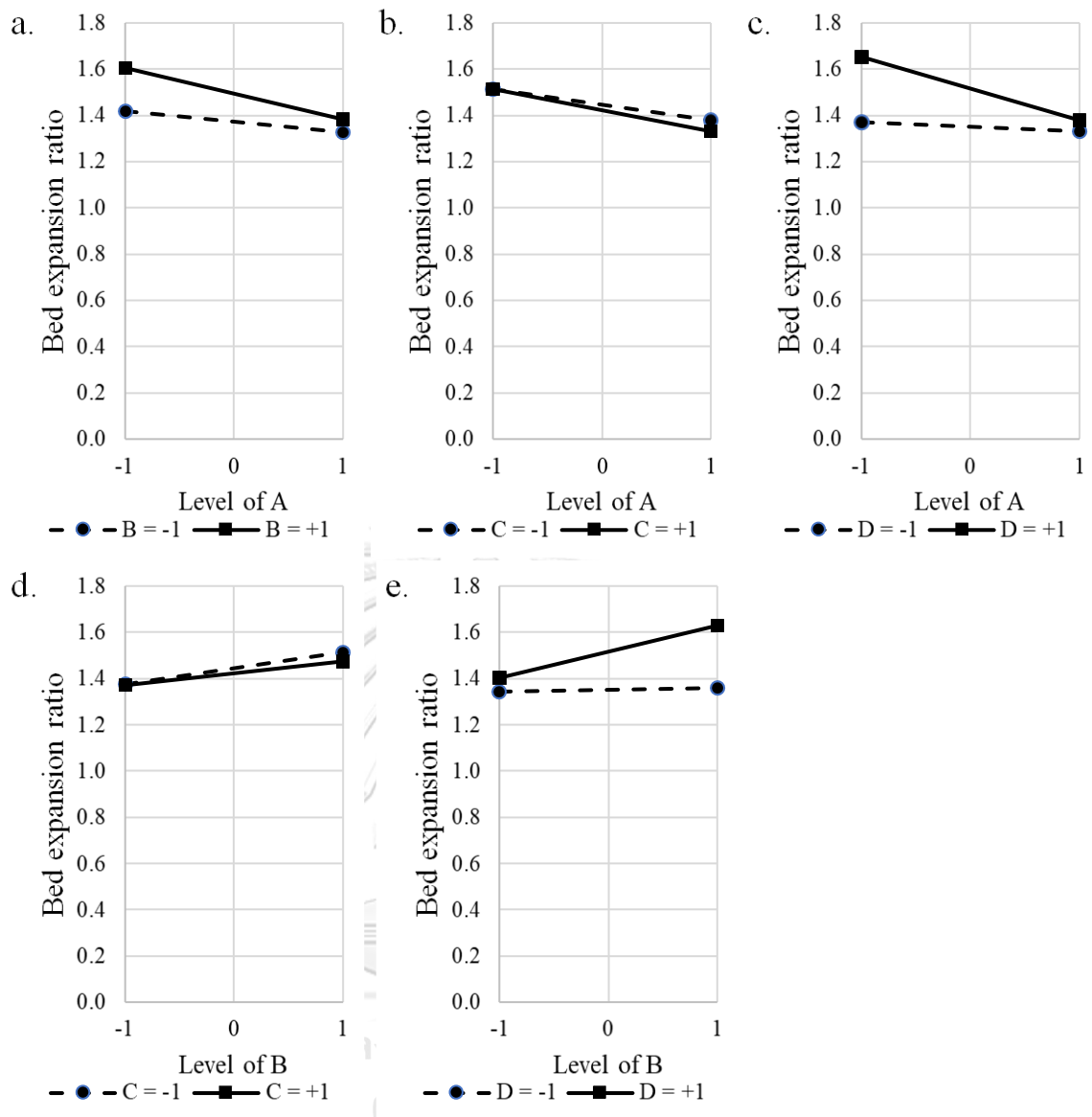


Figure 5.10 The interaction effect plot of the bed expansion ratio of a) AB, b) AC, c) AD, d) BC and e) BD

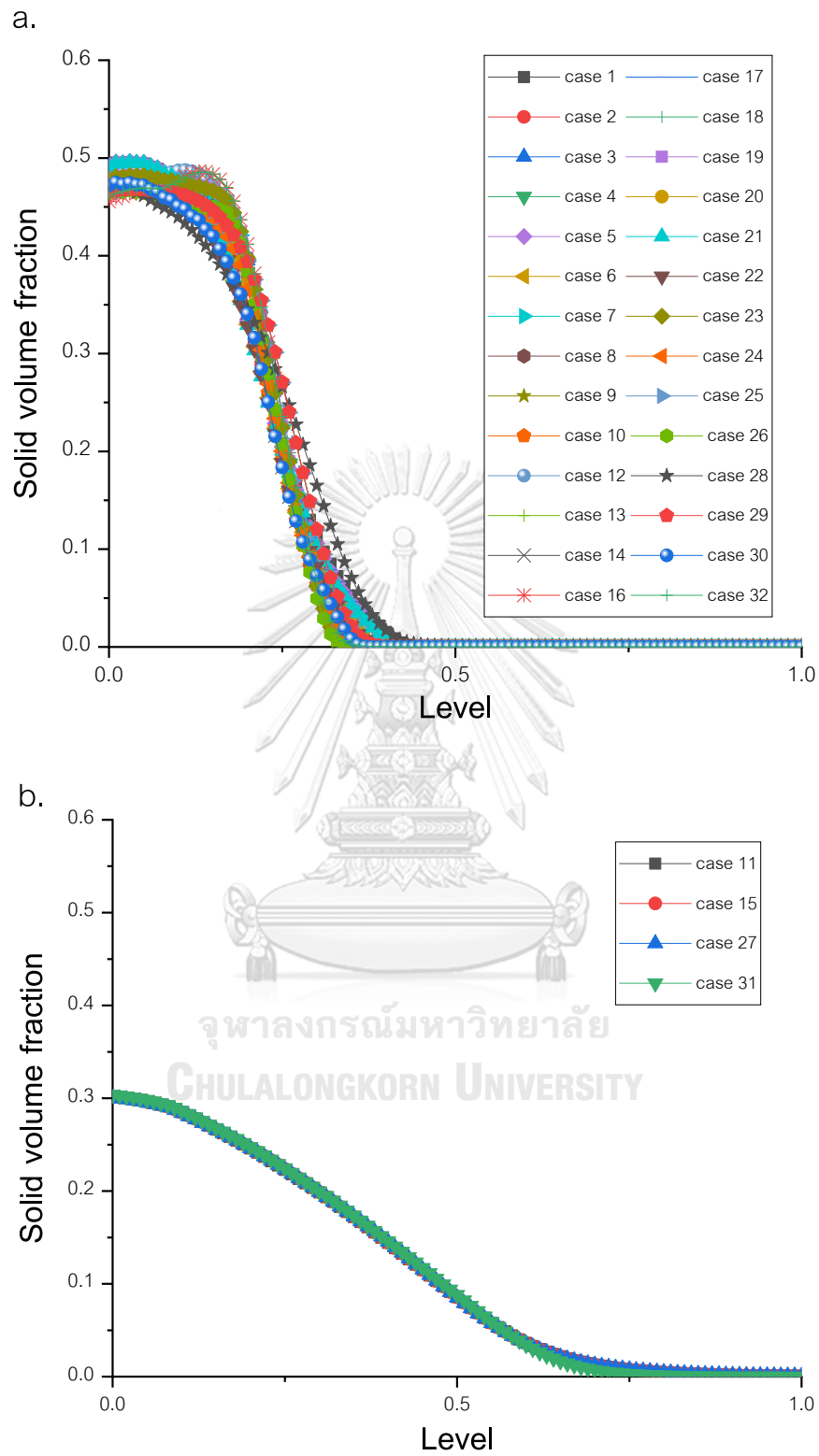


Figure 5.11 The average solid volume fraction classification for a) Group A, b) Group B

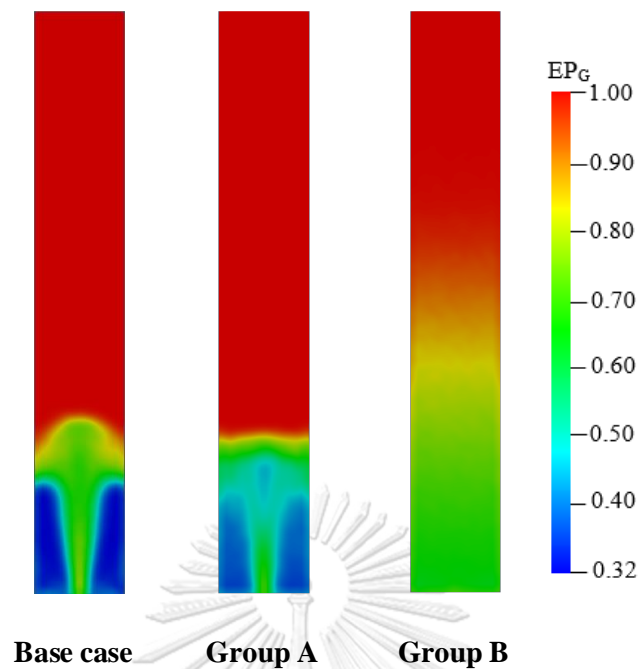


Figure 5.12 The average solid volume fraction classification for a) Group A, b) Group B and c) the contour plots of the averaged void fraction on the central XY-plane of the spouted bed reactor for the base case B1, Group A (case 23), and Group B (case 27)

### 5.2.3 Effect of contact force modeling parameters on the standard deviation of the pressure drop

The pressure fluctuation was one of the response parameters which characterized the hydrodynamics behaviour in the spouted bed reactor (Zhong & Zhang, 2005). The dissipation energy during collision enhanced the void area in which caused the bubble (Guo, Yue, Zhang, & Liu, 2001). The pressure was raised when the bubble moved upward and broken at the surface of the bed. In contrast, the pressure was decreased when the bubble accumulated in the system. Thus, the formation-coalescence of bubbles caused the pressure fluctuation of the system. The ANOVA analysis of the standard deviation of the pressure drop is demonstrated in Table 5.6. The result showed that the particle-particle friction coefficient (A), spring constant (B), and normal particle-particle restitution coefficient (D) had significant effects on the standard deviation of the pressure drop. The significant order was  $D > A > B$  which corresponded to the main effect plot from Figure 5.13. Furthermore, the interaction of AB, AD, BD, CD, DE, ABD, and BCD had a high

impact on the standard deviation of the pressure drop. The interaction plots of each combination are demonstrated in Figure 5.14.

From the results, the parameters with high impact on system hydrodynamics were the particle-particle friction coefficient (A), spring constant (B) and normal particle-particle restitution coefficient (D). These three contact parameters must be carefully defined simulation model including a spouted bed model or related gas-solid multiphase flow system such as a fluidized bed reactor. The  $KE_{\text{translation}}$  had an impact on the spout height which resulted from the designing and operating condition. The increasing of  $KE_{\text{translation}}$  reduced the spout height which observed the bed expansion ratio. The reducing of  $KE_{\text{Rotational}}$  increased the fluctuation of pressure drop presented by the standard deviation of pressure drop. The spouted bed with high spout height model should be obtained from the CFD-DEM with low particle-particle friction coefficient (A), high spring constant (B) and high normal restitution coefficient (D). The high fluctuation resulted from the CFD-DEM from low particle-particle friction coefficient (A), low spring constant (B) and low normal restitution coefficient (D). Moreover, the combined effect of AB, AD, BD and ABD performed an important role which should be received attention. However, the influence of each modeling parameter might differ due to the major force acting on the particle such as rotating drum (Chand, Khaskheli, Qadir, Ge, & Shi, 2012), cyclone (Chu, Chen, & Yu, 2016), and pneumatic conveyor (F. Zhou, Hu, Liu, Liu, & Xia, 2014). This study performed significant contact modelling parameters. It would be better for CFD-DEM simulation to apply the correlation from experiment instead of iterate the proper value to obtained more realistic hydrodynamics profile (Moyssey, Rao, & Baird, 2013; Wu, Thornton, & Li, 2003).

Table 5.6 ANOVA analysis of the standard deviation of pressure drop

Source	Sum of squares	df	Mean squares	F-value	p-value
Model	5.79E+05	15	3.86E+04	64.0	2.10E-11
A-A	1.10E+04	1	1.10E+04	18.2	5.90E-04
B-B	4.20E+03	1	4.20E+03	7.0	1.79E-02
C-C	1.70E+02	1	1.70E+02	0.3	6.03E-01
D-D	3.26E+05	1	3.26E+05	539.6	9.41E-14
E-E	1.99E+03	1	1.99E+03	3.3	8.85E-02
AB	6.39E+04	1	6.39E+04	105.9	1.84E-08
AC	1.58E+03	1	1.58E+03	2.6	1.25E-01
AD	1.34E+05	1	1.34E+05	221.7	8.55E-11
BC	7.98E+02	1	7.98E+02	1.3	2.67E-01
BD	1.55E+04	1	1.55E+04	25.7	1.14E-04
CD	3.40E+03	1	3.40E+03	5.6	3.05E-02
DE	4.23E+03	1	4.23E+03	7.0	1.75E-02
ABC	2.62E+03	1	2.62E+03	4.3	5.35E-02
ABD	5.16E+03	1	5.16E+03	8.6	9.91E-03
BCD	5.42E+03	1	5.42E+03	9.0	8.54E-03
Residual	9.65E+03	16	6.03E+02		
Cor Total	5.89E+05	31			
R <sup>2</sup>	0.984				



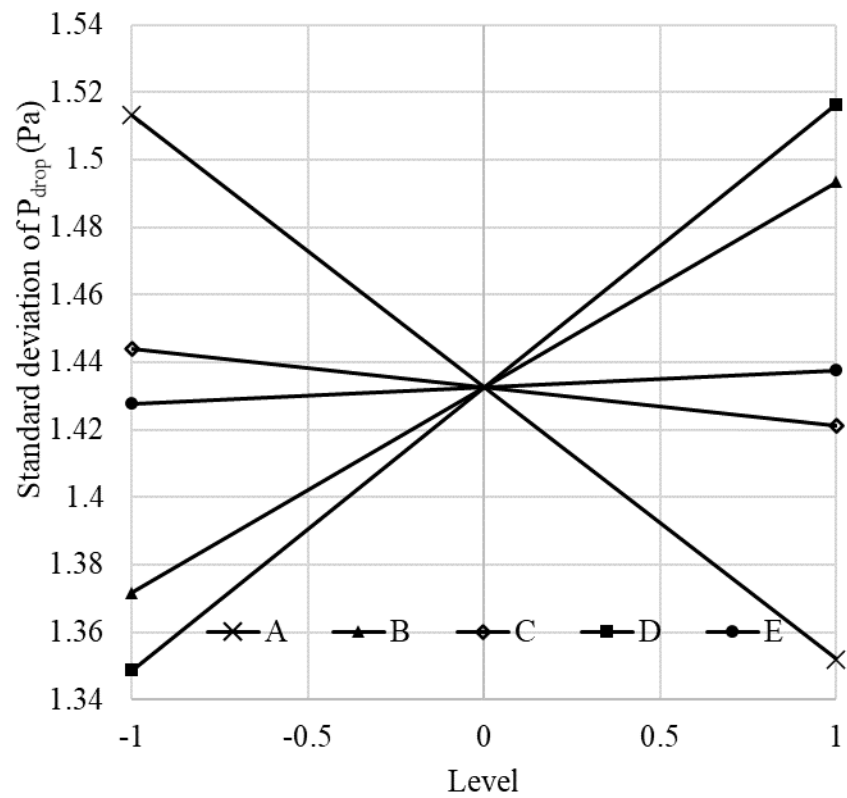


Figure 5.13 The main effect plot of the standard deviation of pressure drop

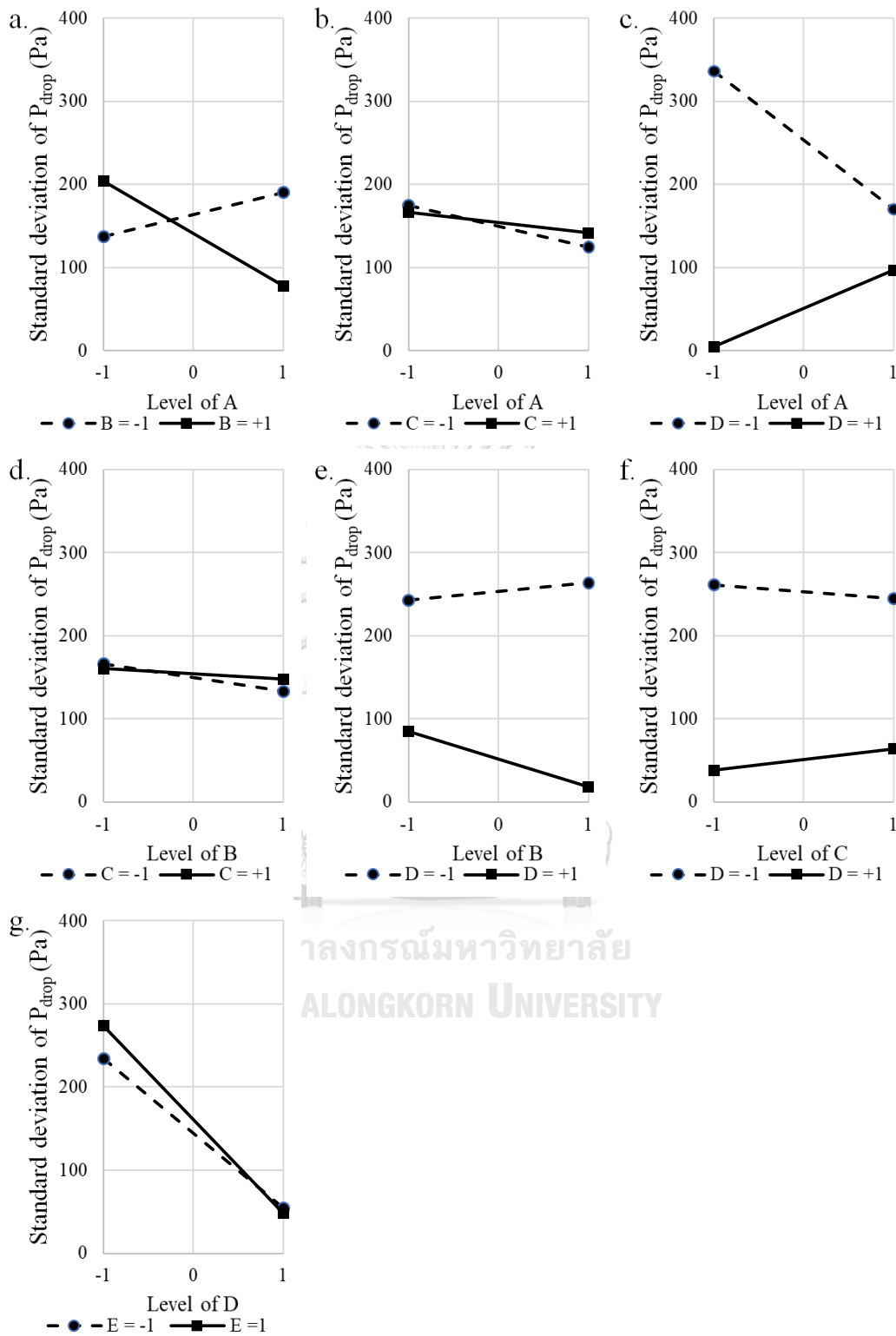


Figure 5.14 The interaction effect plot of the standard deviation of  $P_{drop}$  of a) AB, b) AC, c) AD, d) BC, e) BD, f) CD and g) DE

#### 5.4 Conclusion

The contact modeling parameter such as coefficient (A), the spring constant (B), the ratio of the tangential spring constant to normal spring constant (C), the normal restitution coefficient (D), and the tangential restitution coefficient (E) were studied the significant by  $2^k$  experimental design through CFD-DEM simulation of the spouted bed reactor system. The transient simulation was successful perform by MFX opensource code. A good agreement of simulation and experimental was obtained. It could be concluded that the particle-particle friction coefficient (A), spring constant (B), and normal particle- particle restitution coefficient (D) were the importance collision modeling parameters on the response parameters, the translation kinetic energy of particles, the rotational kinetic energy of particles, the bed expansion, and the standard deviation of pressure drop. They resulted in the significant on hydrodynamics behaviour on the spouted bed and related system. Moreover, the interaction of AB, AD, BD and ABD were the importance of the predicted responses. Thus, the main effect of the particle-particle friction coefficient (A), spring constant (B), and normal particle- particle restitution coefficient (D) and their combination should be received attention for the simulation of multiphase flow system such as the fluidized bed reactor. Finally, this study presented the using of  $2^k$  factorial design to screen the contact parameters including individual and interaction effect which proposed the solution to understanding the various perspective of the system.

## CHAPTER 6

### Developing the correlation of coefficient of restitution from experimental results and other literature results

#### 6.1 The effect of diameter on the coefficient of restitution

In this study, the solid particles with a diameter of 3-6 mm as the testing particle were investigated the kinetic energy loss after contacting by drop test apparatus. The effect of diameter on the coefficient of restitution is shown in Figure 6.1 and Figure 6.2. Figure 6.1 shows the collision between the glass bead and acrylic. Figure 6.2 displays the collision between polypropylene ball and acrylic. The experimental results showed a similar trend in the coefficient of restitution. However, different material types gave a different range of the coefficient of restitution. From the results, the coefficient of restitution was independent of the sizing or diameter. Even though the contact area and particle indentation were widened with the increasing of the diameter (Wang & Zhu, 2013). But the difference in the millimeter scale gave a similar ratio between indentation and radius which resulted in the close coefficient of restitution (Johnson, 1985a).

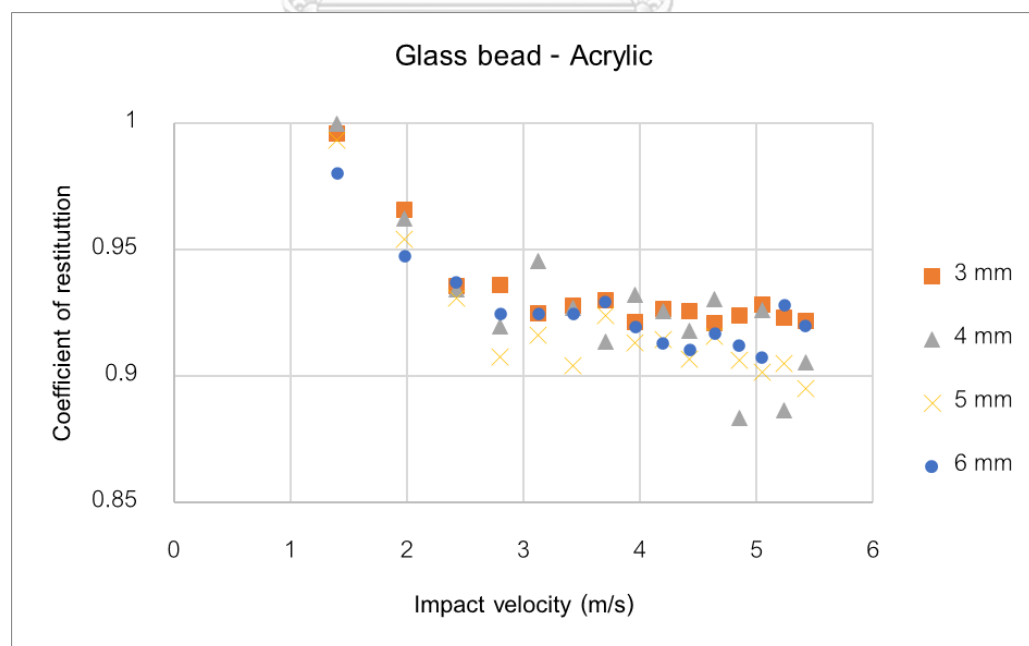


Figure 6.1 The sizing independent of coefficient of restitution for the contact between glass bead and acrylic plate

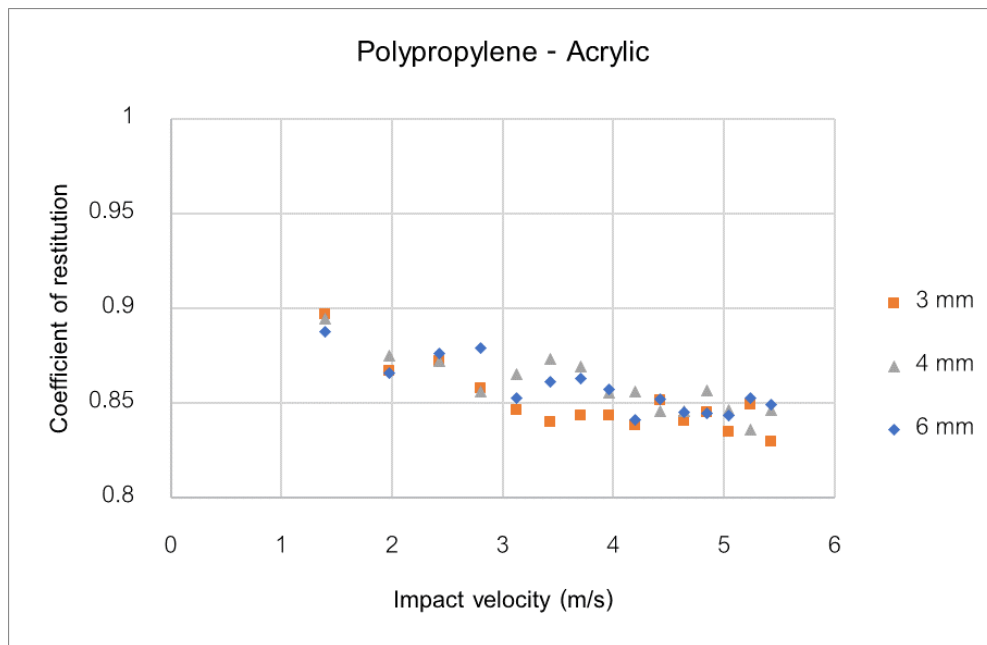


Figure 6.2 The sizing independent of the coefficient of restitution for the collision between polypropylene and acrylic plate

## 6.2 The effect of impact velocity on the coefficient of restitution

The impact velocity was an influencing factor on the coefficient of restitution as shown in Figure 6.3. The material types were reported by effective elastic modulus ( $E^*$ ). The table of material types, elastic modulus and Poisson's ratio are summarized in Table 6.1. It was observed the negative relation between impact velocity and coefficient of restitution. The coefficient of restitution was high at low impact velocity and low at high impact velocity. The impulse force penetrated the collision at high impact velocity at the contact area. Several theories and researches discussed the dissipation energy from the collision while W. J. Stronge, Sofi, and Ravani (2019) discussed the dissipation energy from the perspective of viscoelastic theory. The increasing of the impact velocity increased the compression during contact which required more work to return to the original shape state due to the friction inside the solid particle. The kinetic energy was a loss due to the dissipation wave from immediate contact (W. Stronge, 1995). It effected the decreasing of the coefficient of restitution while the impulse contact increased from the impact velocity (Y. Q. Li, Gao, Horner, & Zheng, 2017). However, some study obtained

an opposite trend due to the cohesive force for the micro sizing particle. (Sun et al., 2019; Tsuji, Tanaka, & Ishida, 1992).

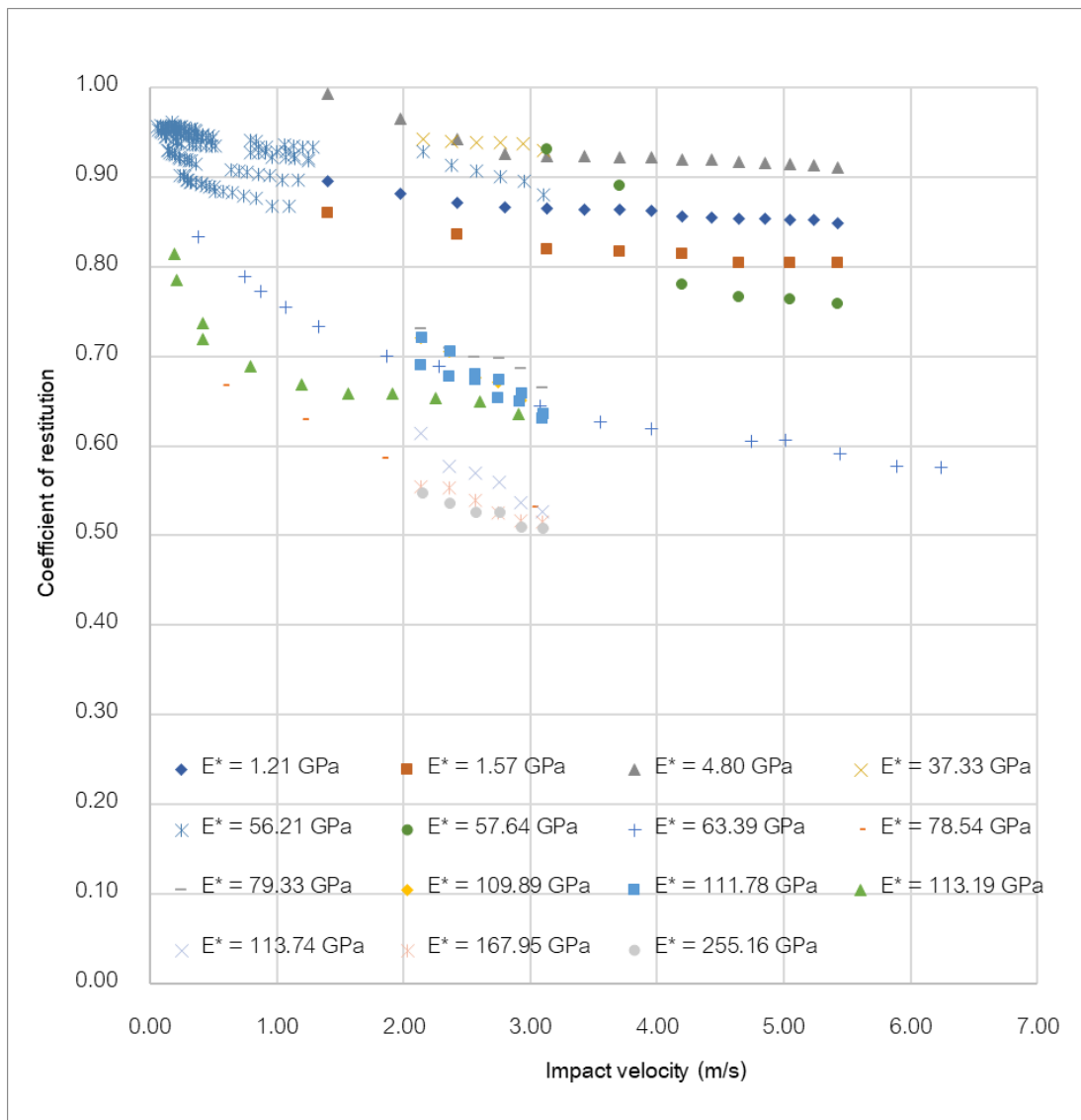


Figure 6.3 The effect of impact velocity on the coefficient of restitution at difference effective elastic modulus ( $E^*$ )

Table 6.1 Material properties and calculated effective elastic modulus

Material A	Material B	E,A (GPa)	E,B (GPa)	$\nu$ ,A	$\nu$ ,B	E* (GPa)
Polypropylene	Acrylic	1.3	4.41	0.42	0.37	1.20
Polypropylene	Steel	1.3	200	0.42	0.25	1.57
Glass	Acrylic	73	4.41	0.25	0.37	4.80
Glass	Glass	70	70	0.25	0.25	37.33
Glass	S7 steel	70	207	0.25	0.3	56.21
Glass	Steel	73	200	0.27 5	0.25	57.64
Aluminium oxide	Aluminium alloy	314	70	0.27	0.32	63.39
Chrome steel	Aluminium bronze	200	110	0.3	0.31 6	78.54
Brass	S7 steel	103	207	0.39 3	0.3	79.33
Chrome steel	Stainless steel	200	200	0.3	0.3	109.89
Low carbon steel	S7 steel	200	207	0.3	0.3	111.78
S7 steel	S7 steel	206	206	0.3	0.3	113.19
Tungsten carbide	S7 steel	621	207	0.18	0.3	167.95
Tungsten carbide	Stainless steel	622	200	1.18	0.3	255.16

### 6.3 The effect of material type on the coefficient of restitution

Material types played a role in the coefficient of restitution. The evidence is shown in Figure 6.3. The collision between two objects was examined by drop test including the experiment from this study and the other reference. In the field of contact mechanics, the specific physical properties were usually presented by effective elastic modulus which

was the function of elastic modulus and Poisson's ratio as shown in Equation 61 (W. Stronge, 1995). The effective elastic modulus was developed from the serial of two spring which combined the ability of elastic and deformation. The pairs of the collision between material are summarized in Table 6.1.

Figure 6.1, Figure 6.2 and Figure 6.3 showed that the coefficient of restitution was decreased until it reached some constant. The coefficient of restitution of glass bead and the acrylic plate was reduced nearly 0.92 while the polypropylene on the acrylic plate was lessened to 0.85 approximately. The trend from these results was similar to the previous studies (Aman et al., 2016; Brake, 2012; J. Coaplen, W. J. Stronge, & B. Ravani, 2004). Thus, the physical properties were important for the coefficient of restitution (Tsuji et al., 1992). For instance, the elastic modulus of the glass bead and polypropylene were 70 GPa and 2 GPa, respectively, (ToolBox, 2003), while Poisson's ratio of the glass bead and polypropylene were 0.25 and 0.42, respectively, (ToolBox, 2008).

The comparison of elastic modulus showed that the glass bead had the elastic ability from the compression force more than polypropylene. The contrast of Poisson's ratio was observed that polypropylene had more sensitivity on the deformation than glass bead. Thus, the coefficient of restitution of polypropylene was lower than the glass bead. However, the collision between metal material did not propose a high coefficient of restitution than the glass or polymer material. The force that acts on the contact surface was high due to the density of the material as shown in Table 6.1. As discussed above, the dissipation energy was released from impulse force which is related to the indentation and sizing of the contact area.

#### **6.4 The effect of temperature on the coefficient of restitution**

The effect of temperature on the coefficient of restitution is shown in Figure 6.4 and Figure 6.5. The similar trends between temperature and the coefficient of restitution at each impact velocity were observed. Two pair of materials such as glass bead-steel plate and polypropylene-steel plate was studied for the effect of temperature on the coefficient of restitution. The results showed that the coefficient of restitution was decreased with the increase of temperature. The trend of the coefficient of restitution and impact velocity was



still the same. For the glass bead, the maximum temperature was 350°C due to the limitation of the heating source. For polypropylene, the maximum of studied temperature was 150°C closing to the melting point at 160°C but this point was neglected. This is because the permanent deformation occurred after contact which violence the assumption of this study. The increase in temperature reduced the elastic modulus and increased the Poisson's ratio (Carneiro & Puga, 2018; Nguyen, Yu, & Park, 2011). However, it was not practical to measure to physical properties at each temperature. Thus, this study developed the coefficient of restitution by fitting the correlation from the deviation from the coefficient of restitution at room temperature.



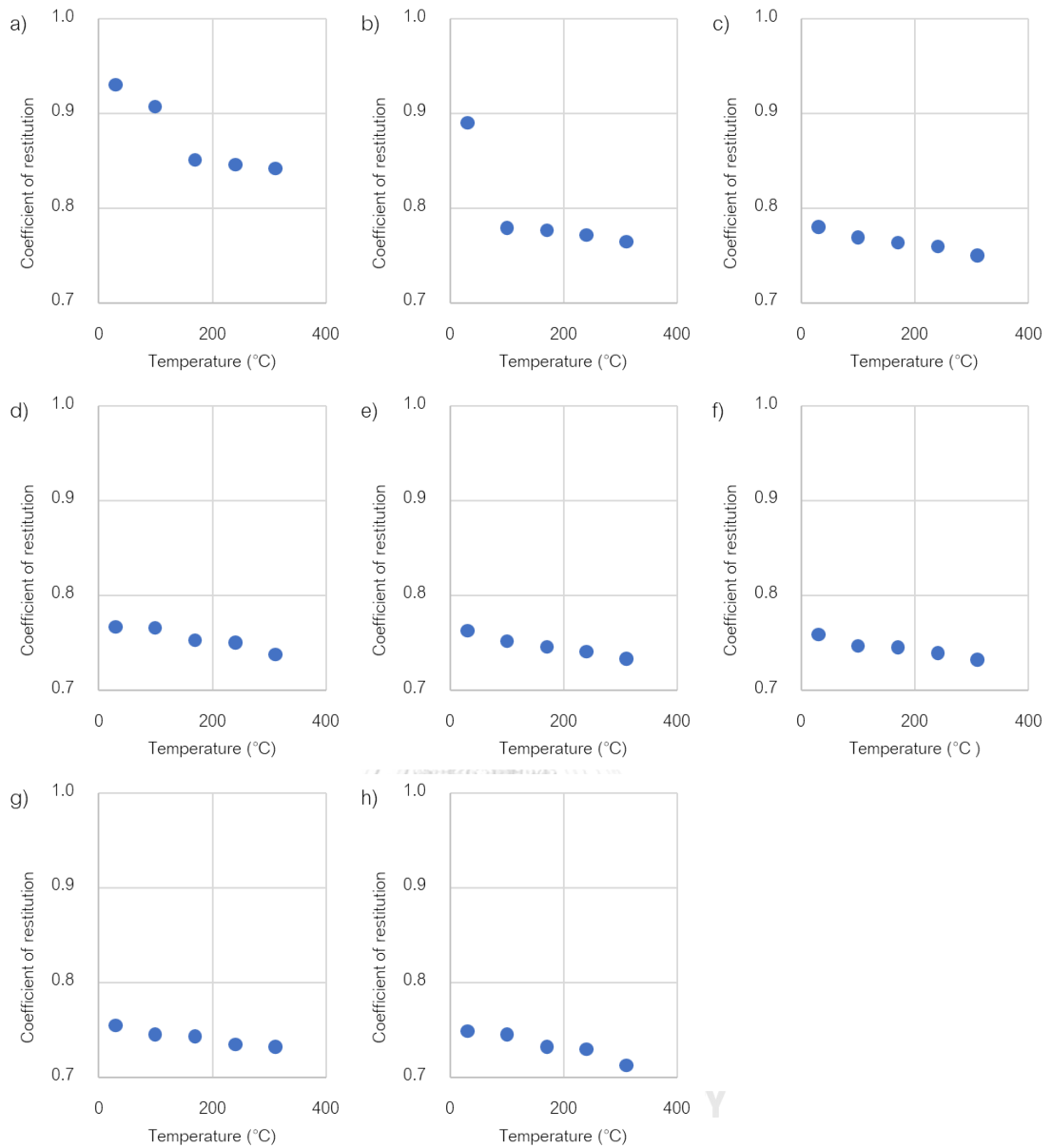


Figure 6.4 The effect of temperature on coefficient of restitution at difference impact velocity of the collision between glass bead and steel plate, a)  $V_{imp} = 1.4$  m/s, b)  $V_{imp} = 2.4$  m/s, c)  $V_{imp} = 3.1$  m/s, d)  $V_{imp} = 3.7$  m/s, e)  $V_{imp} = 4.2$  m/s, f)  $V_{imp} = 4.6$  m/s, g)  $V_{imp} = 5.0$  m/s and h)  $V_{imp} = 5.4$  m/s

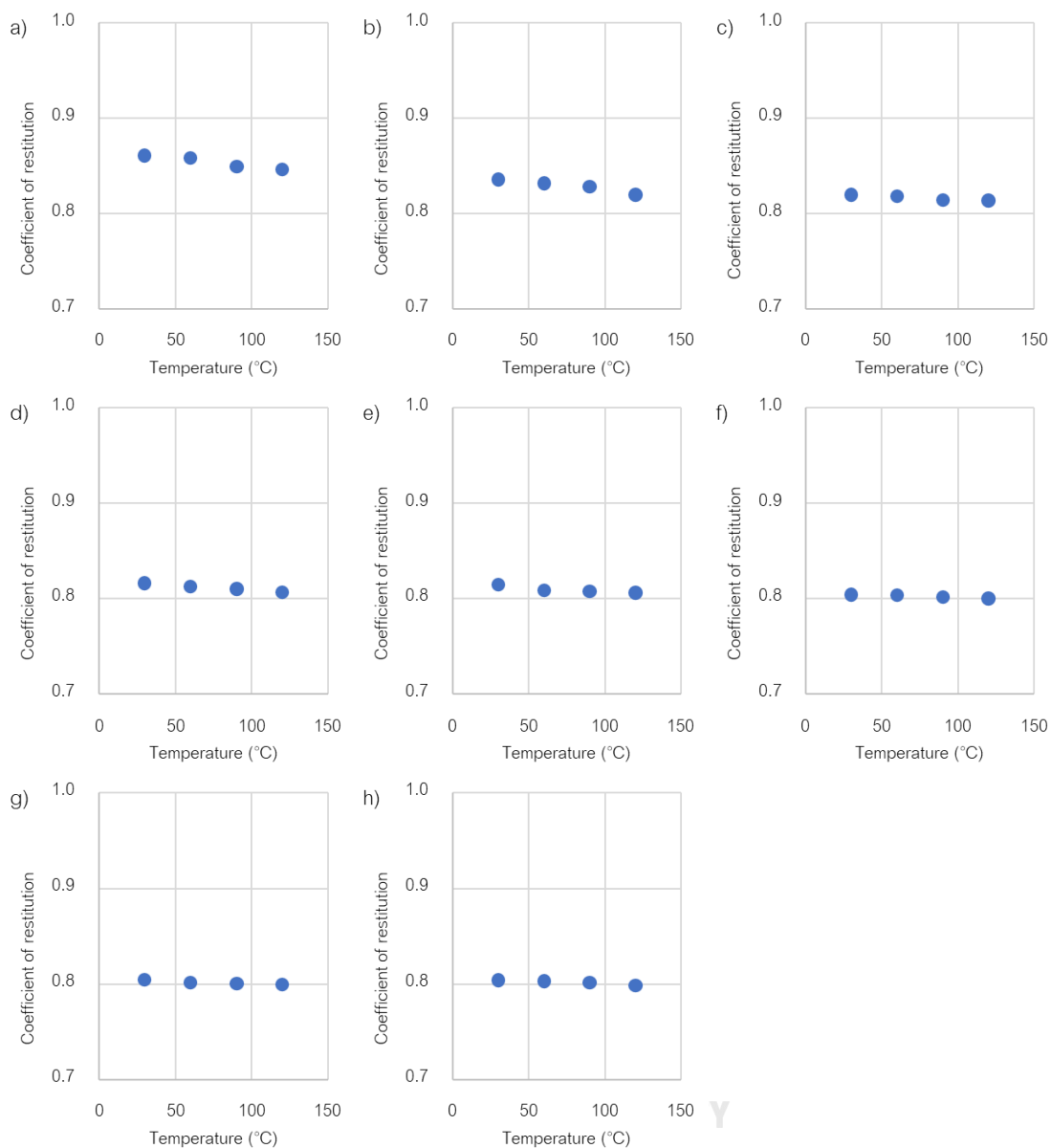


Figure 6.5 The effect of temperature on coefficient of restitution at difference impact velocity of the collision between polypropylene and steel plate, a)  $V_{imp} = 1.4$  m/s, b)  $V_{imp} = 2.4$  m/s, c)  $V_{imp} = 3.1$  m/s, d)  $V_{imp} = 3.7$  m/s, e)  $V_{imp} = 4.2$  m/s, f)  $V_{imp} = 4.6$  m/s, g)  $V_{imp} = 5.0$  m/s and h)  $V_{imp} = 5.4$  m/s

### 6.5 The correlation of coefficient of restitution

The experimental results were imported to develop the correlation of coefficient of restitution. The logistic equation was selected to fit the correlation. The pattern of the Logistic equation was shown below (Verhulst, 1845; Weisstein, 2003).

$$e_0 = \left[ \frac{C_1 - C_2^*}{1 + \left( \frac{v_{imp}}{C_3} \right)^{C_4}} \right] + C_2^* \quad (64)$$

$e_0$  is coefficient of restitution,  $C_1$  is an initial value or maximum coefficient of restitution,  $C_2^*$  is the final value or the minimum coefficient of restitution,  $V_{imp}$  is dependence value or impact velocity,  $C_3$  is a center parameter and  $C_4$  is power parameter.

The correlation of coefficient of restitution was first developed with the function of impact velocity. After that the parameter of each condition was summarized to investigate the relationship with the effective elastic modulus. It was observed that the minimum of coefficient of restitution was the function of an effective modulus base on the logarithm equation in term  $C_2^*$  as shown below.  $C_8$ ,  $C_9$  and  $C_{10}$  were parameters in the correction factor of the minimum coefficient of restitution.

$$C_2^* = \frac{C_5 \ln(C_6 E^*) + C_7}{C_8^{C_9} + C_{10}} \quad (65)$$

$$\frac{1}{E^*} = \frac{1 - \nu_1^2}{E_1} + \frac{1 - \nu_2^2}{E_2} \quad (66)$$

Parameter	Definition	Unit
$e_0$	Restitution coefficient at room temperature	-
$v_{imp}$	Impact velocity	m/s
$C$	Arbitrary Constant	
$\nu$	Poisson's ratio	-
$E$	Elastic modulus	GPa
$E^*$	Effective modulus	GPa

Finally, the correlation of coefficient of restitution was divided into 4 groups to decrease the error percentage from the raw data which is summarized in Table 6.2.

The coefficient of restitution with the function of temperature was developed by using the correction factor multiply with the coefficient of restitution at room temperature as shown in Equation 64.

$$e(T) = e_0 \left[ -A_1 \ln\left(\frac{T}{T_{melt}}\right) + A_2 \right] \quad (67)$$

However, the correction factor function was developed individual function for the collision between glass bead – steel plate and polypropylene – steel plate as shown in Table 6.3. The temperature was presented by normalized temperature which was described by the ratio of operating temperature and melting point of the material. The melting temperatures of glass bead and polypropylene were 704 °C and 160 °C, respectively. The correlation from this studied proposed the novel correlation which included the operating temperature in the correlation. The comparison of predicted coefficient of restitution between this study and the existing model from Thornton (1997) were shown in Figure 6.6 and Figure 6.7. It showed that the coefficient of restitution from this study obtained a good agreement with the experimental results than the traditional model of Thornton (1997). This is because the correlation from Thornton (1997) depended only impact velocity and physical properties as shown in Equation 62.

Table 6.2 The coefficient in the correlation of coefficient of restitution at each range of effective elastic modulus ( $E^*$ )

Equation set	1	2	3	4
$E^*$ (GPa)	$1.21 < E^* \leq 21.07$	$21.07 < E^* \leq 60.51$	$60.51 < E^* \leq 140.8$	$140.8 < E^* \leq 255.2$
$C_1$	1.000	1.000	1.000	1.000
$C_3$	0.722	2.430	14.324	0.847
$C_4$	1.722	2.111	0.347	0.756
$C_5$	0.077	0.001	0.004	0.002
$C_6$	0.127	0.673	0.426	0.428
$C_7$	0.898	0.841	0.103	0.371
$C_8$	0.402	0.451	1.533	0.501
$C_9$	0.112	0.354	0.000	0.583
$C_{10}$	0.047	0.458	1.928	0.492

$$e(T) =_2 \left[ -A_1 \ln\left(\frac{T}{T_{melt}}\right) + A_2 \right] e_0 \quad (68)$$

Parameter	Definition	Unit
$e_0$	Restitution coefficient at room temperature	-
$e(T)$	Restitution coefficient at T K	-
A	Arbitrary Constant	
T	Contact Temperature	K
$T_{melt}$	Melting temperature	K

Table 6.3 The coefficient for temperature correction factor

Material	Glass bead	Polypropylene
$T_{\text{melt}}$ (K)	1073	433
$A_1$	0.073	0.034
$A_2$	0.91	0.99



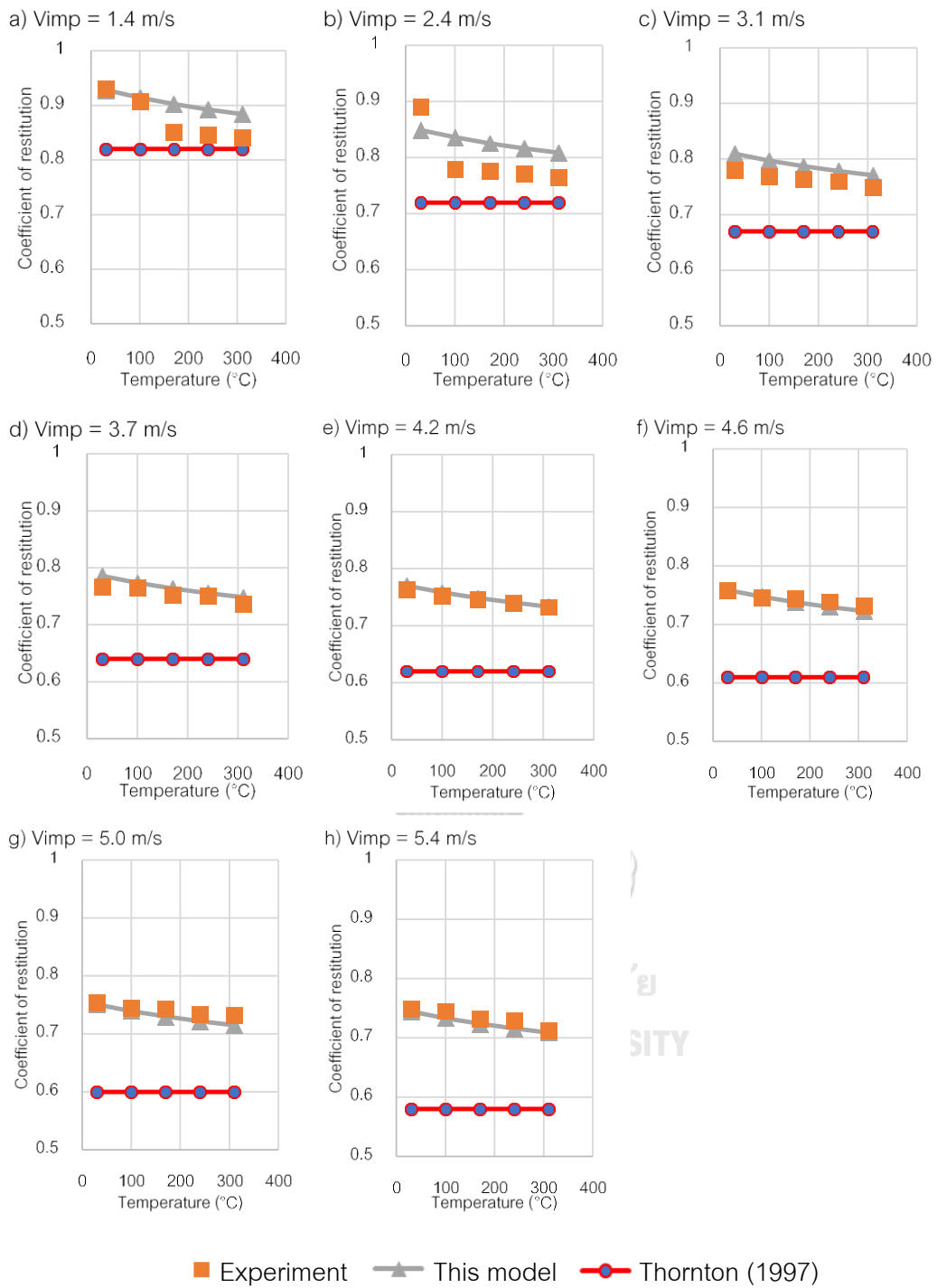


Figure 6.6 The comparison of predicted coefficient of restitution with the existing model of the collision between glass bead and steel plate at difference impact velocity and temperature



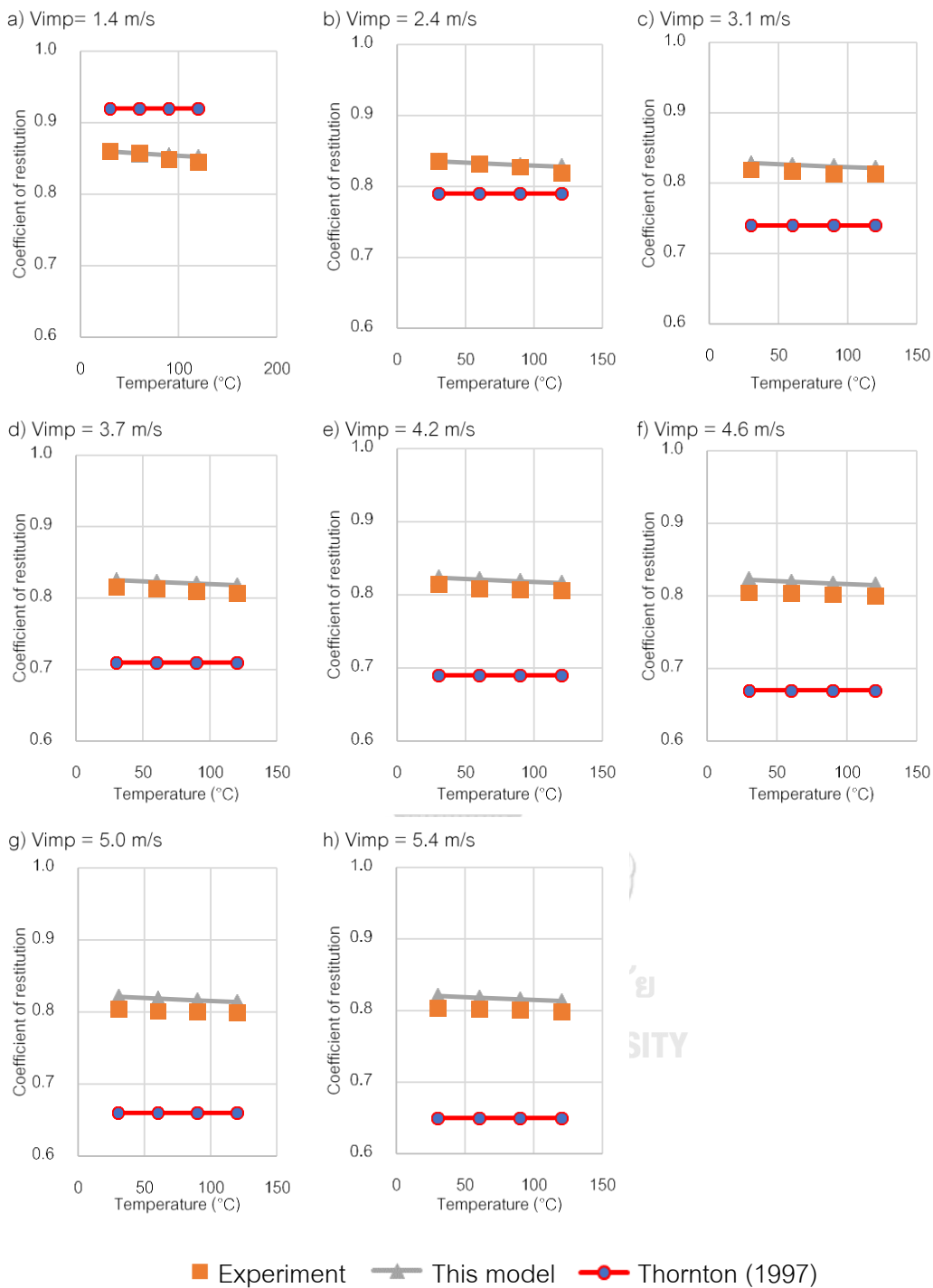


Figure 6.7 The comparison of predicted coefficient of restitution with the existing model of the collision between polypropylene and steel plate at difference impact velocity and temperature

## 6.6 The validation of correlation coefficient of restitution by free fall of the single particle

The free fall from experimental result and simulation was compared to the particle trajectory in Figure 6.8. It was the simplest case which widely used to validate for any development of DEM simulation (Garg, 2010). The comparison was demonstrated by the plot of impact velocity and rebound height as shown in Figure 6.9. From the results, it showed the advantage using the dynamics coefficient of restitution which obtained the accurately predicted rebound height. In contrast, using a constant coefficient of restitution resulted in a good prediction of the specific impact velocity. It could not represent the real system which contained many parameters and relative velocity. For instance, the simulation with constant close to 1 of the coefficient of restitution was matched only the low impact velocity. The coefficient of restitution at 0.9 for glass bead – acrylic plate and 0.85 for polypropylene – acrylic plate was agreed with the experiment results at high impact velocity. The simulation also predicted the rebound height at each impact velocity and temperature of the object as shown in Figure 6.10 and Figure 6.11. Figure 6.10 shows the predicted coefficient of restitution of the contact between glass bead and steel. Figure 6.11 shows the predicted coefficient of restitution of the contact between polypropylene and steel. The good agreement was obtained except the collision of polypropylene and steel at 150 °C due to close with the melting point at 160 °C as described above. Moreover, the predicted rebound height from the free-fall simulation with a constant coefficient of restitution 0.7, 0.8, 0.9 and 1.0 were comparable with the experimental results and prediction from correlation. Furthermore, this result showed that using the coefficient of restitution obtained good validation in the local impact velocity and temperature. Low impact velocity and low temperature were suitable with the high coefficient of restitution. In contrast, the high impact velocity and high temperature were appropriate for low coefficient of restitution.

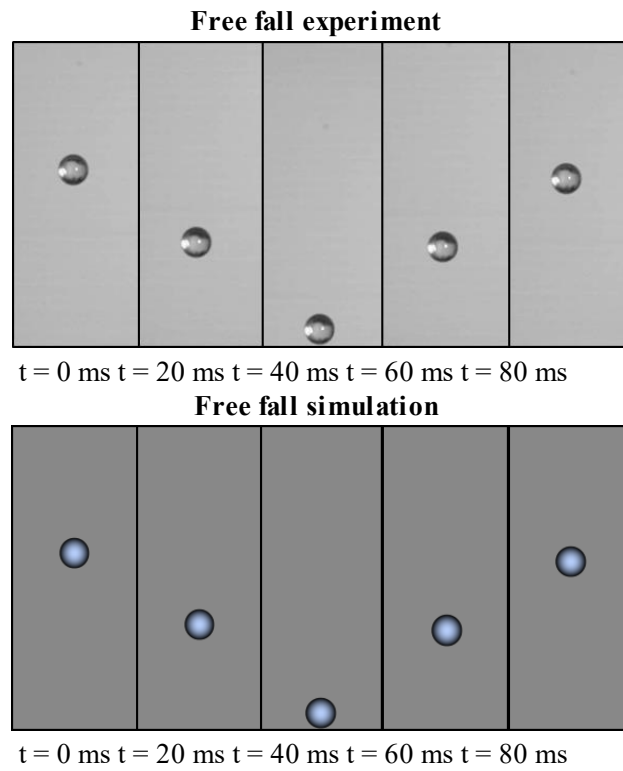


Figure 6.8 The comparison between drop test from experiment and simulation



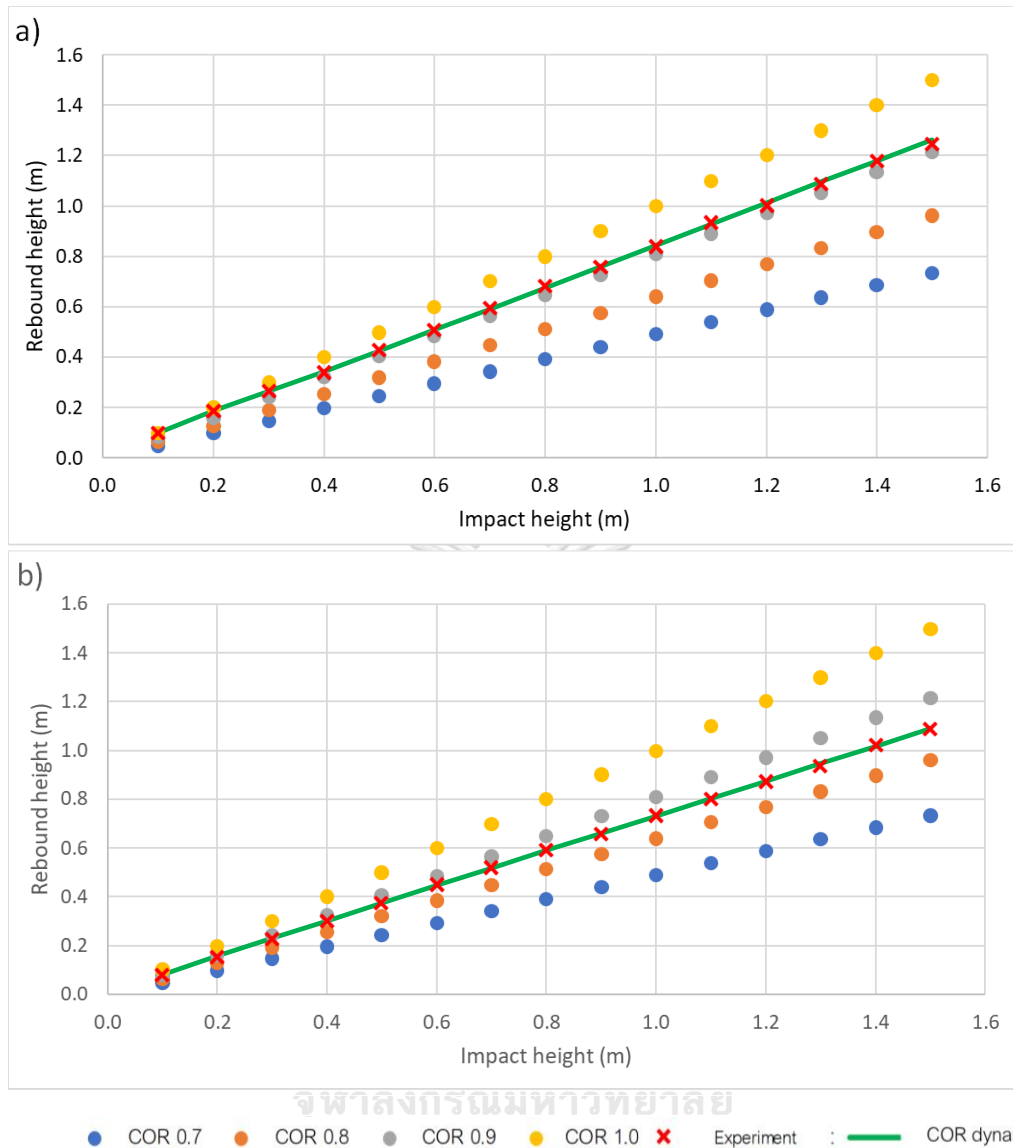


Figure 6.9 The comparison of predicted rebound height at each coefficient of restitution  
 a) the collision of the glass bead and acrylic plate at room temperature and b) the collision of polypropylene and acrylic plate at room temperature

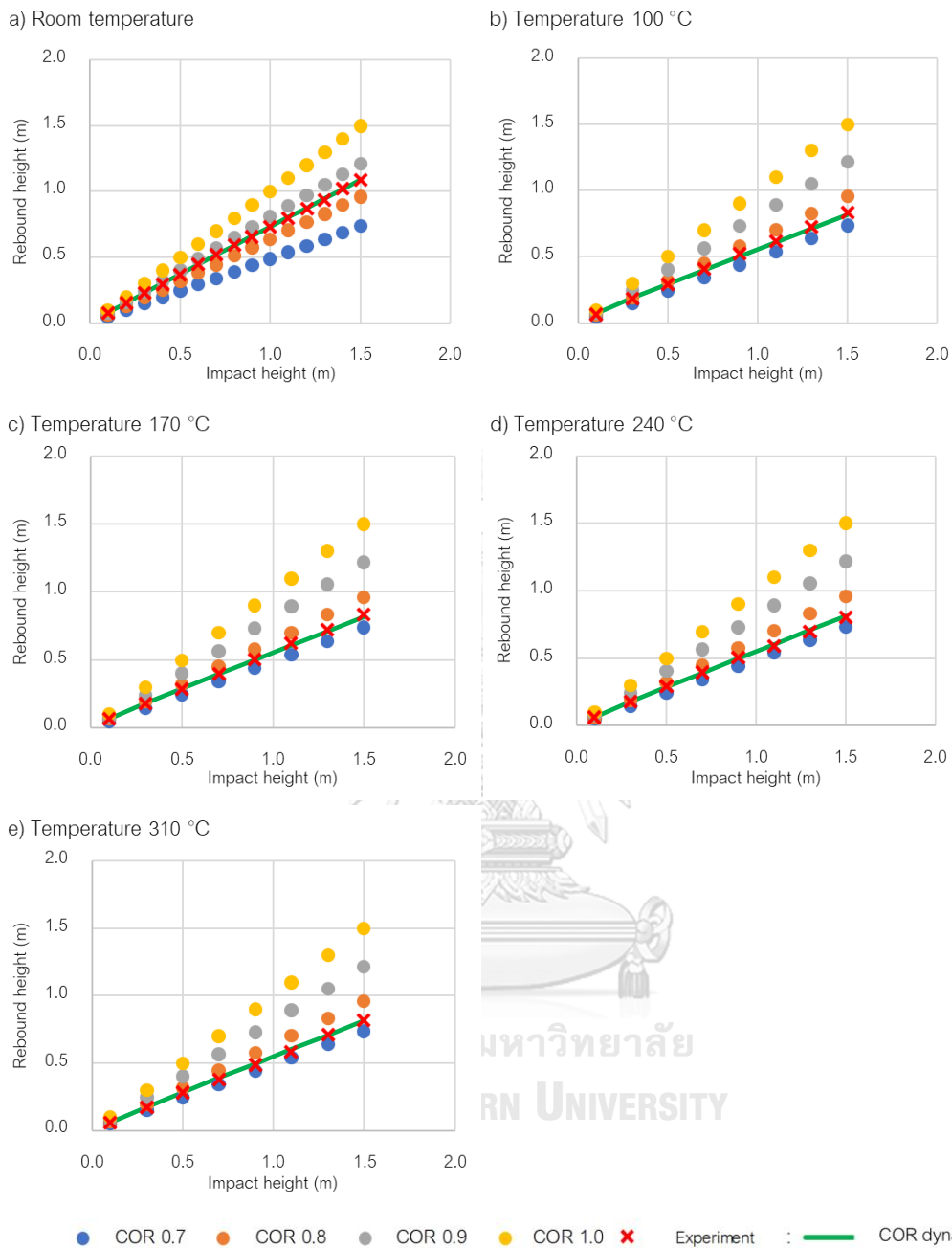


Figure 6.10 The predicted free fall height at difference impact velocity and temperature of the collision between glass bead and steel plate a) Room temperature, b) 100 °C, c) 170 °C, d) 240 °C and e) 310 °C

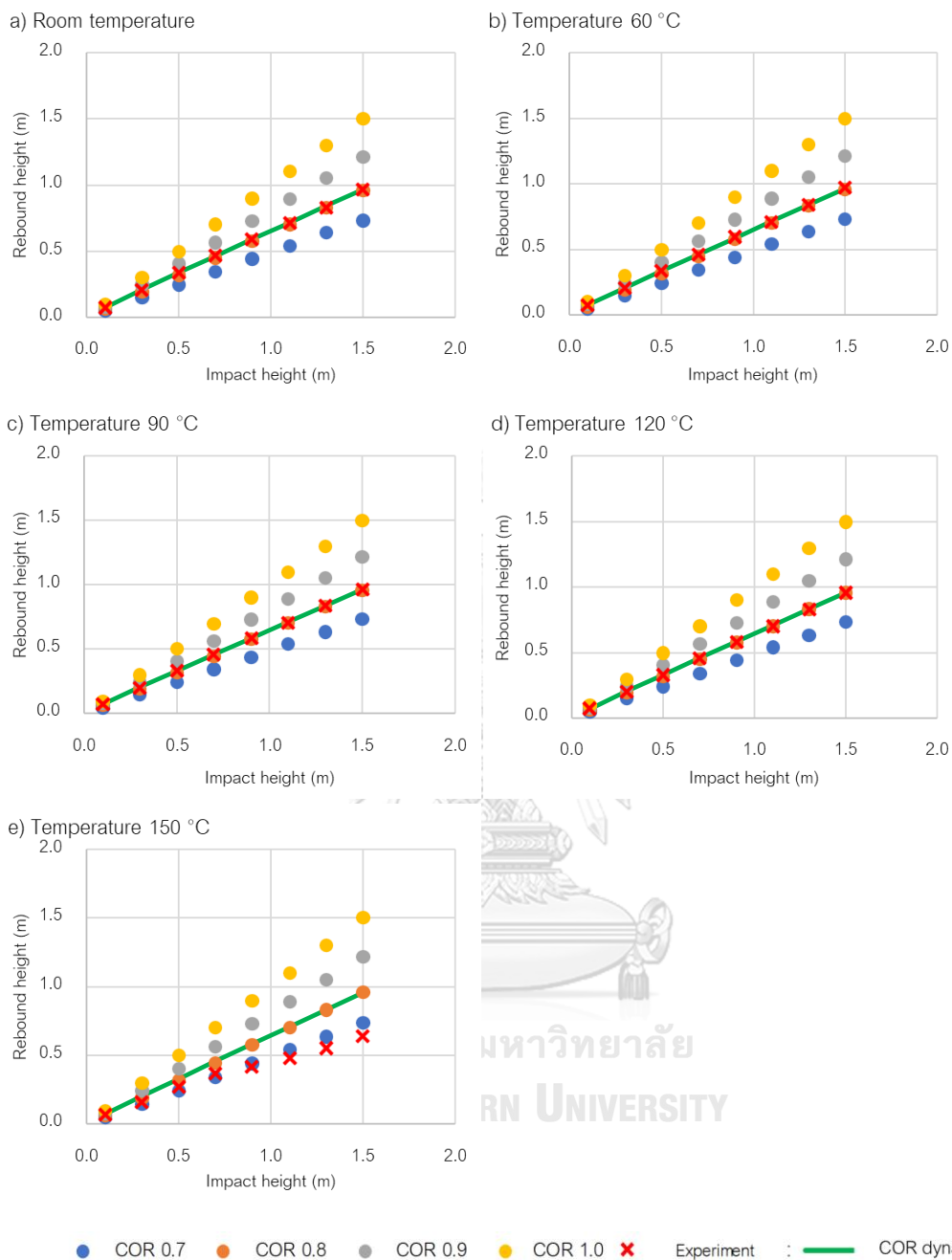


Figure 6.11 The predicted free fall height at different impact velocity and temperature of the collision between polypropylene and steel plate a) Room temperature, b) 60 °C, c) 90 °C, d) 120 °C and e) 150 °C

## 6.7 Conclusion

The dynamics coefficient of restitution correlations was developed from the drop test experimental approach. The impact velocity was generated up to 5.4 m/s from the maximum dropped height of 1.5 m without permanent deformation of the solid particle. Both the experiment and the dynamics coefficient of restitution showed a negative trend with increasing impact velocity and temperature for each sample material-plate surface combination. The coefficient of restitution trend of glass beads was more elastic than polypropylene beads for all impact velocities. In addition, the conventional DEM simulation using a constant coefficient of restitution was compared with the novel DEM simulation using the dynamics coefficient of restitution. The predicted collision from conventional DEM simulation was closed to some specific range of impact velocity and operating temperature. On the other hand, the novel DEM simulation using the dynamics coefficient of restitution obtained good agreement with the experimental result at a wide range of impact velocity and operating temperature. This dynamics coefficient of restitution concept then can be applied for other material combinations with a wide range of operating conditions to obtain the database of dynamics coefficient of restitution for simulation of solid handling application.

## CHAPTER 7

### The development of the CFD-DEM simulation with the dynamics coefficient of restitution

The comparison of constant coefficient of restitution and dynamics coefficient of restitution in CFD-DEM simulation was demonstrated by three cases which were internal circulating fluidized bed, rotating drum and spouted bed.

#### 7.1 Internal circulating fluidized bed

The internal circulating fluidized bed is a good comparison example which consists of two fluidized bed chambers. One chamber is introduced by high inlet velocity which is typically called high-velocity chamber (HV). The other chamber is fed by low inlet velocity and is called low-velocity chamber (LV). Two systems of ICFB with difference solid material types including glass bead and polypropylene were demonstrated.

The snapshot of the particle movement of ICFB with glass bead at each coefficient of restitution constant is shown in Figure 7.1. The description of hydrodynamics behaviour was already discussed in Chapter 4. The snapshot of the particle movement of ICFB with glass bead at different operating temperature was also simulated using dynamics coefficient of restitution approach. The snapshot of particle movement using the dynamics coefficient of restitution at each operating temperature is shown in Figure 7.2. Three operating temperatures were configured at 298 K, 600 K and 900 K. The increasing of operating temperature enhanced the bubble formulation as same as the decreasing coefficient of restitution. The experimental result and correlation were consistent in which obtained the negative trend with the increasing of the coefficient of restitution. The comparison of the solid flux of ICFB with glass bead is shown in Figure 7.3. The solid flux was confirmed to have negative trend with the increasing of operating temperature. Besides, the ICFB was simulated with the other type of material. The snapshot of ICFB with polypropylene at each constant coefficient is shown in Figure 7.4. Polypropylene was simulated at 298 K, 350 K and 400 K. The snapshot of ICFB with polypropylene using the dynamics coefficient of restitution at each operating temperature is shown in Figure 7.5. The bubble formation for all configured operating temperature was higher than the



predicted hydrodynamics profile of ICFB with glass bead. The trend of solid flux with the increasing of operating temperature is shown in Figure 7.6. The negative trend of solid flux with the increasing of operating temperature was obtained.

The DEM simulation result of the ICFB system demonstrated the feasibility to apply the correlation of coefficient of restitution in the same system but different material types and operating temperature. The advantage of using a dynamics coefficient of restitution is obtained the reliable kinetic energy loss corresponding to the experimental result. Moreover, the convenience is obtained in which no need to iterate the coefficient of restitution.



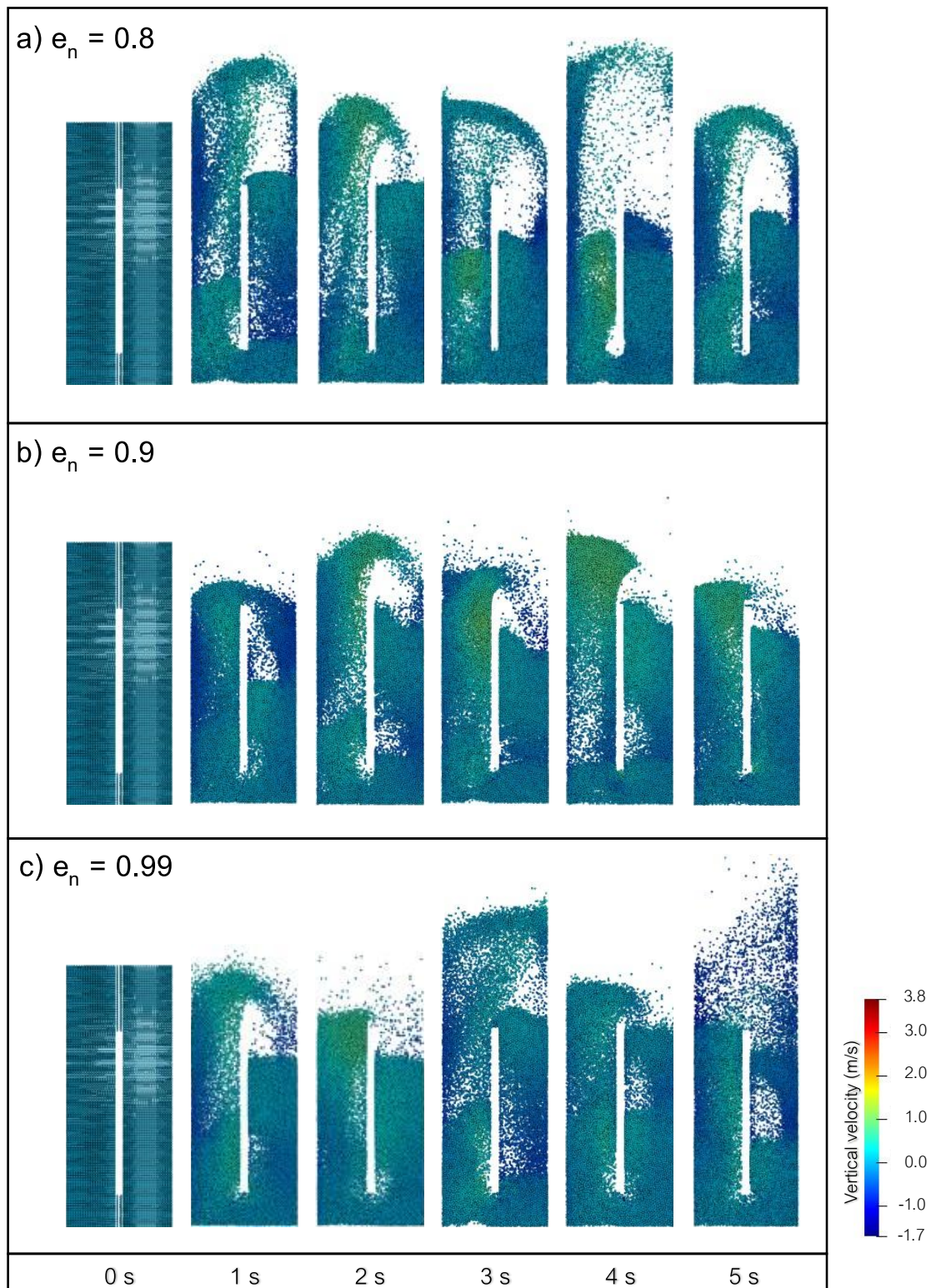


Figure 7.1 The snapshots of glass bead in ICFB model with constant coefficient of restitution ( $e_n$ ): a)  $e_n = 0.8$ , b)  $e_n = 0.9$  and c)  $e_n = 0.99$

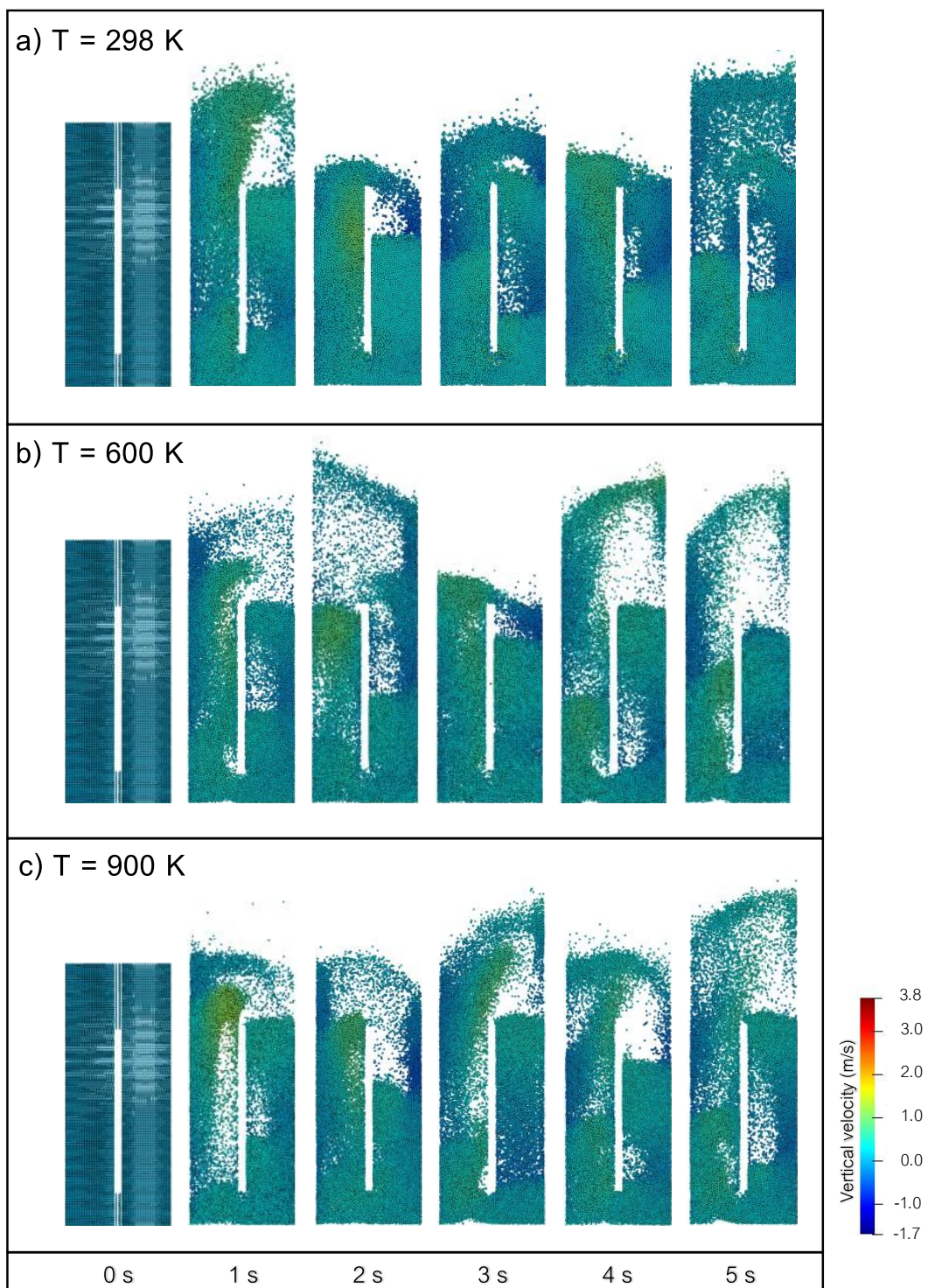


Figure 7.2 The snapshots of glass bead in ICFB model with dynamics coefficient of restitution ( $e_n$ ) at each operating temperature : a) 298 K, b) 600 K and c) 900 K

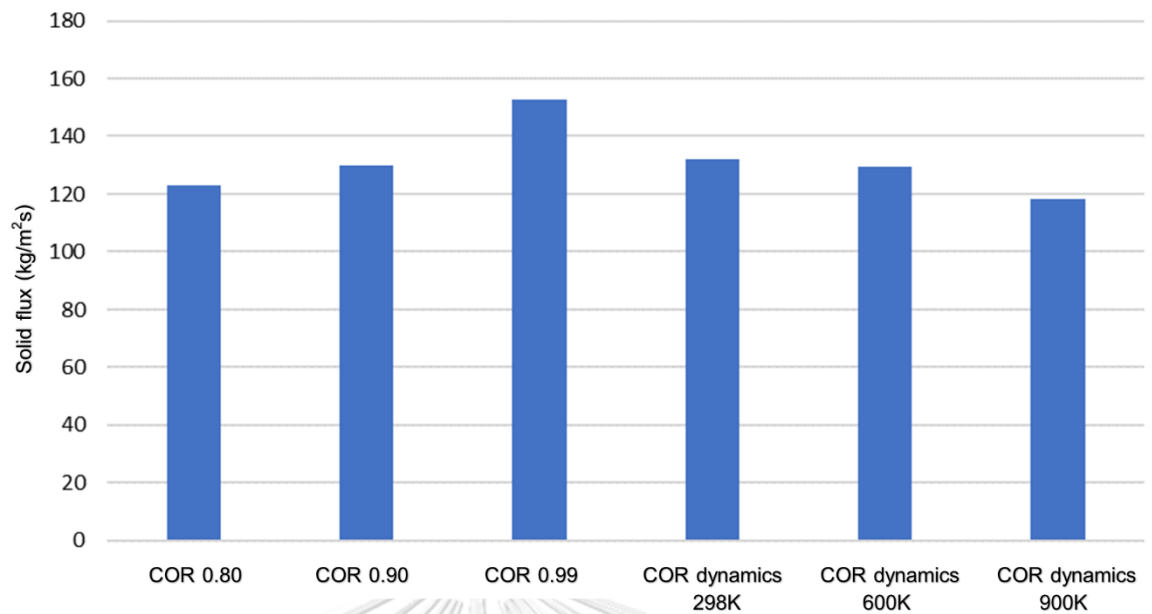


Figure 7.3 The solid flux of ICFB with glass bead at coefficient of restitution approach





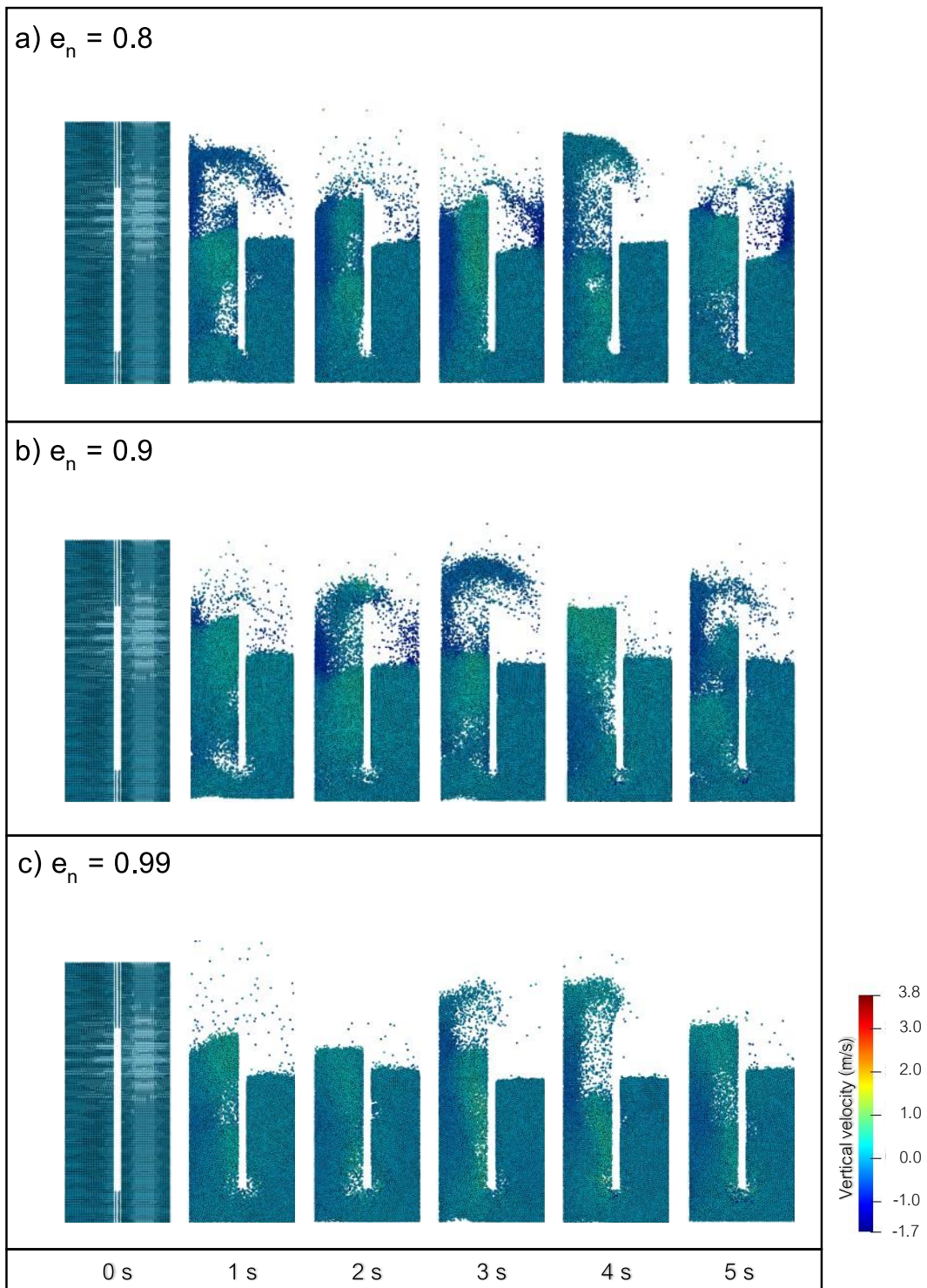


Figure 7.4 The snapshots of polypropylene in ICFB model with constant coefficient of restitution ( $e_n$ ): a)  $e_n = 0.8$ , b)  $e_n = 0.9$  and c)  $e_n = 0.99$

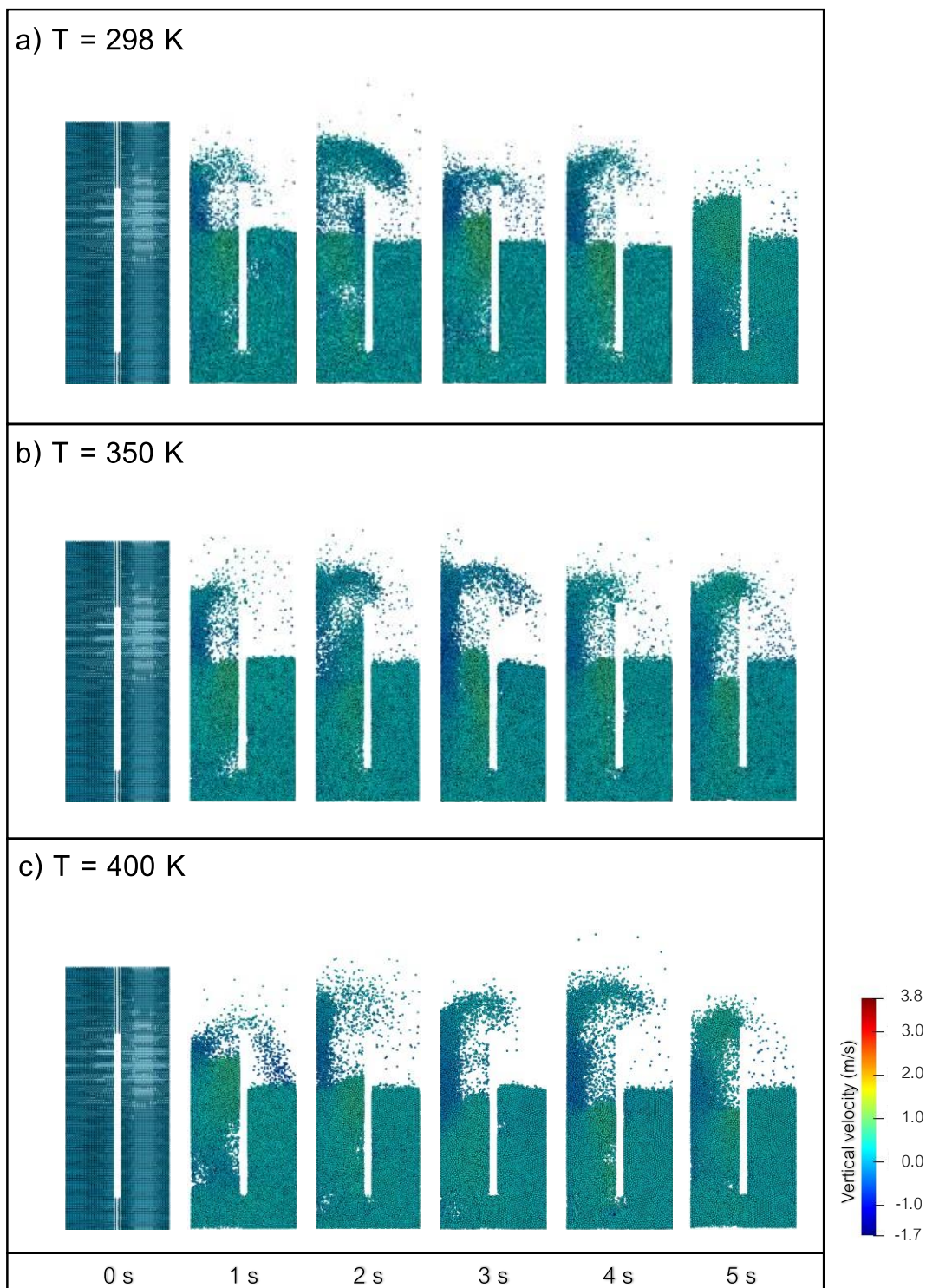


Figure 7.5 The snapshots of polypropylene in ICFB model with dynamics coefficient of restitution ( $e_n$ ) at each operating temperature : a) 298 K, b) 350 K and c) 400 K

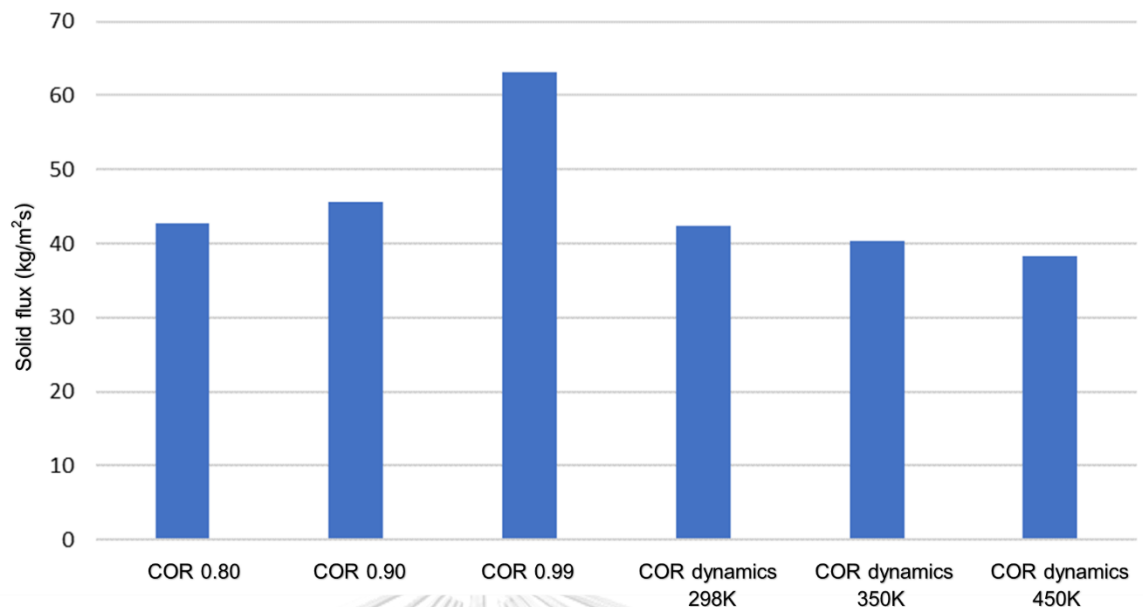


Figure 7.6 The solid flux of ICFB with polypropylene at coefficient of restitution approach

## 7.2 Rotating drum

The snapshot of the rotating drum at each operating condition is shown in Figure 7.7 which shows the angle of repose and vertical velocity by contour color. The results showed that all simulated rotating drum cases rotated in cascading regime. The power draw was selected to compare the lifting power in a vertical direction. Figure 7.8 illustrates that the power draw was increased with the increasing rotating speed. This is because increasing the rotating speed exhibits the analogy with the increasing of the input of kinetic energy. For 15 RPM, the power draw from the simulation with the dynamics coefficient of restitution was closed to 1. However, the power draw of simulation with the dynamics coefficient of restitution at 35 RPM was closed to 0.9. The decreasing of the predicted coefficient of restitution happened from the number of avalanche particle. Moreover, the higher impact velocity was obtained from the drum at a higher rotating speed.

The dynamics coefficient of restitution in the rotating drum computed the local variation of the coefficient of restitution. It shows the advantage for the system which

consists of two or more contact characteristics to represent the real local coefficient of restitution.

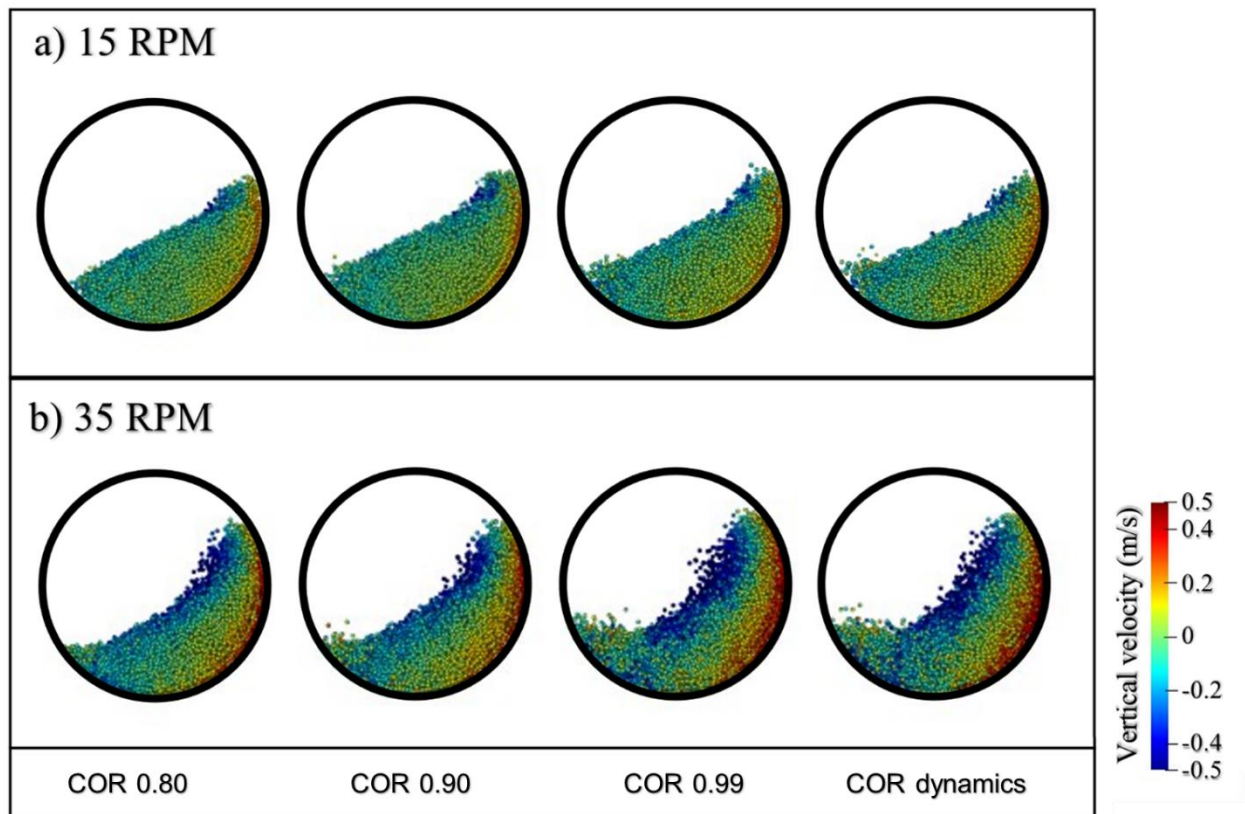


Figure 7.7 The snapshots at 15 s of rotating drum simulation at different rotating speed and coefficient of restitution approaches: a) 15 RPM and b) 35 RPM



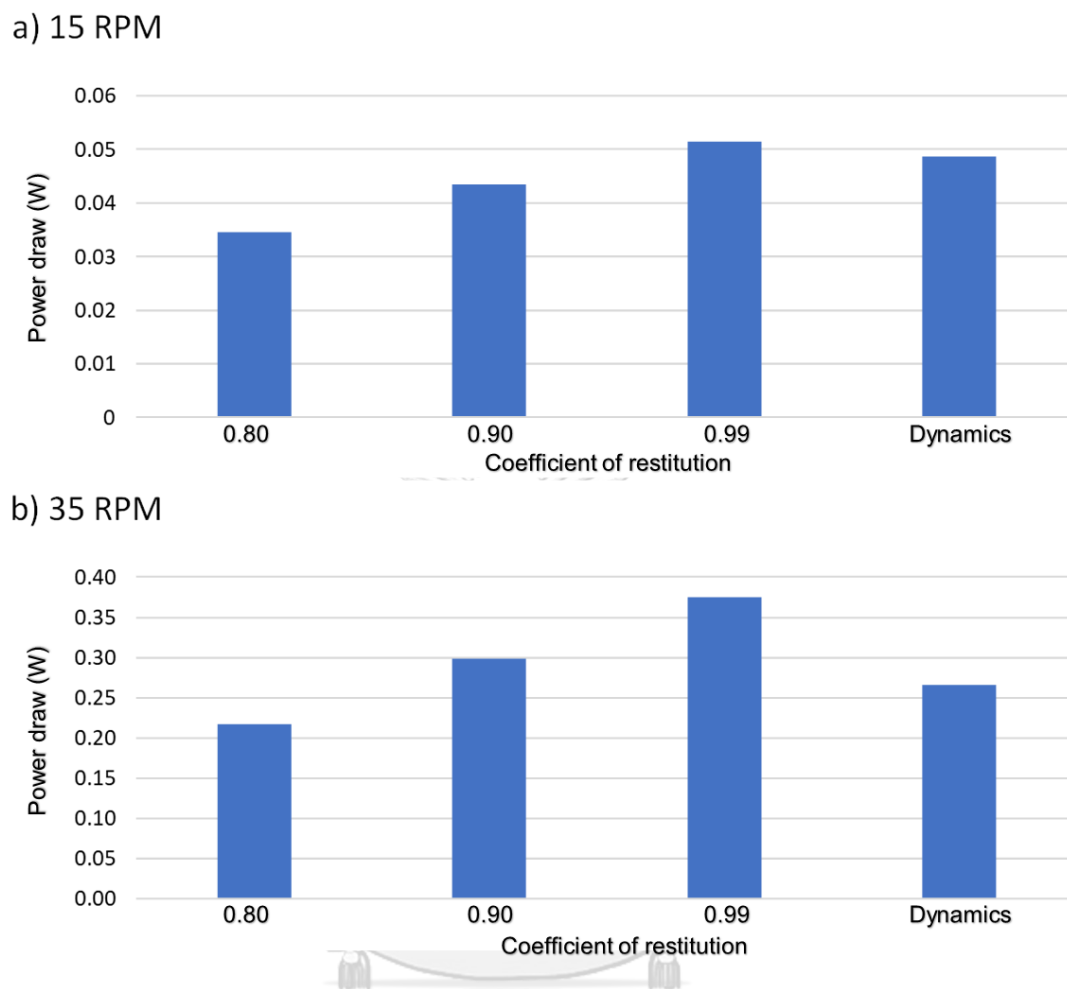


Figure 7.8 The predicted power draw of rotating drum at each operating condition and coefficient of restitution approaches: a) 15 RPM and b) 35 RPM

### 7.3 Spouted bed

The spouted bed simulation was selected to investigate the feasibility of using the novel CFD-DEM approach. The comparisons of the spouted bed simulation with a constant coefficient of restitution and the dynamics coefficient of restitution were compared. This section aimed to illustrate the flexibility of the dynamics coefficient of restitution on the operating condition. The particle movement plots are shown in Figure 7.9. The bed expansion and spout height were compared. The results showed that using low constant lower bed expansion and higher spouted height. The pressure fluctuation at each coefficient of restitution approach is plotted as the comparison in Figure 7.10. The

result showed that high fluctuation was resulted from the simulation using a low coefficient of restitution. This is because the dissipation of kinetic energy enhanced the void space and bubble which caused pressure fluctuation. For the first 0.5 seconds, the pressure fluctuation using the dynamics coefficient of restitution was closed to the simulation with a coefficient of restitution equally 1. In addition, the comparison showed that a quasi-steady state from the simulation with a low constant coefficient of restitution required more computation time. Using the dynamics coefficient of restitution proposed the simulation result with the dissipation energy similar to the case with a 0.9-1.0 coefficient of restitution. It however required computational resource less than the simulation using 1.0 of the coefficient of restitution. The average solid vertical velocity is plotted in Figure 7.11. It showed that the dynamics coefficient of restitution could apply to the model due to a good agreement with the experimental results.

The simulation using the dynamics coefficient of restitution obtained the prediction related to the different operating condition such as gas inlet velocity. The novel approach improves the simulation procedure which can neglect the guessing of the coefficient of restitution.

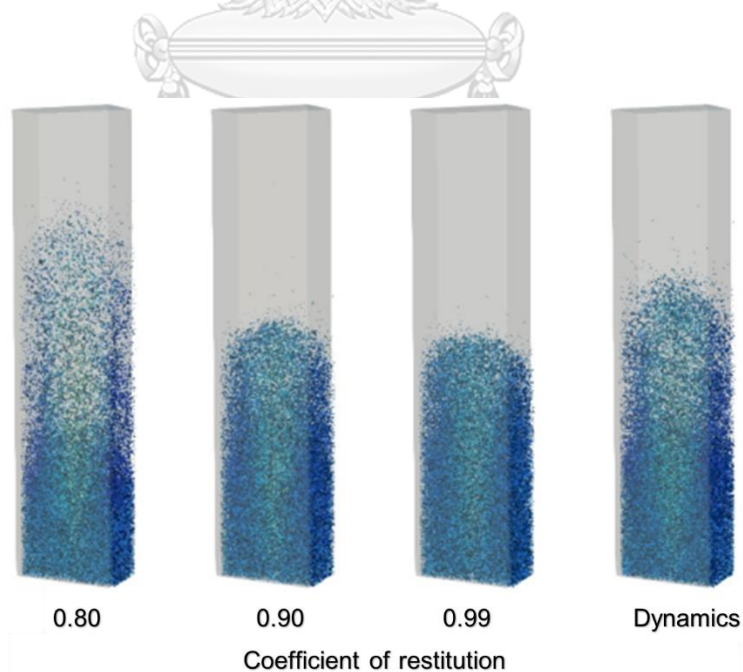


Figure 7.9 Discrete solid particles movement at each coefficient of restitution condition

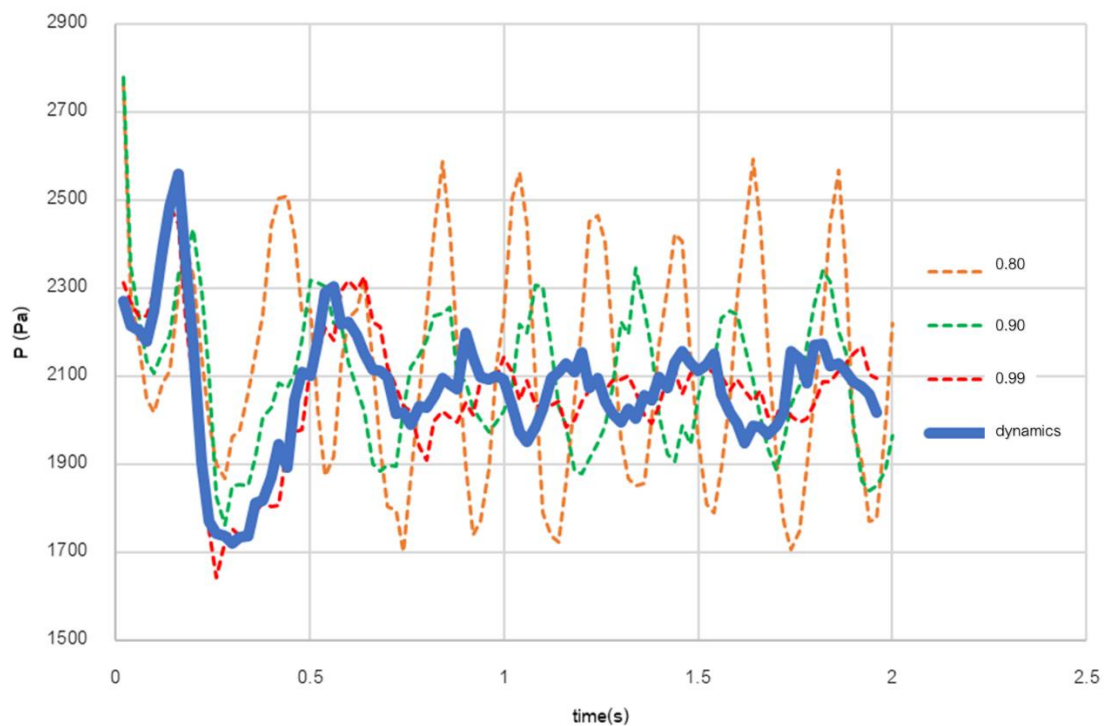


Figure 7.10 The pressure drop fluctuation of spouted bed reactor at  $V_{sp} = 90$  m/s



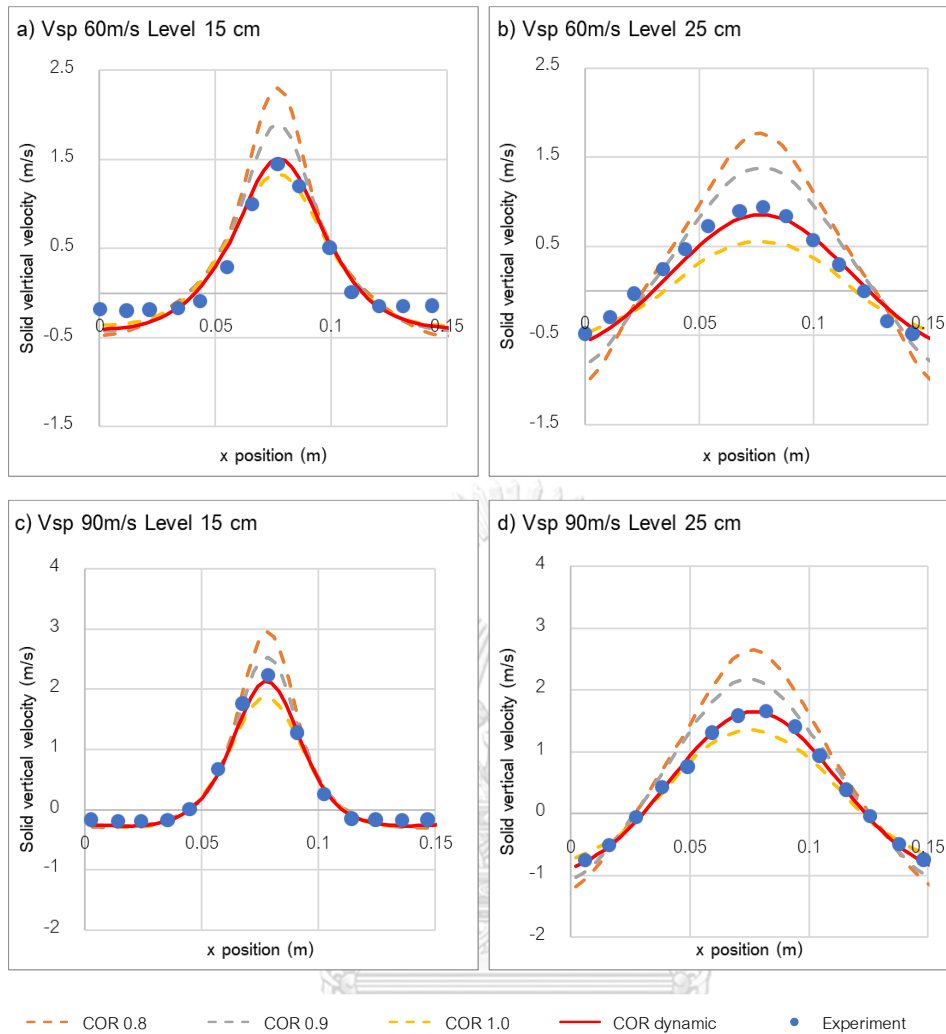


Figure 7.11 The comparison of average solid vertical velocity at each coefficient of restitution approach and experimental results a)  $V_{sp} = 60$  m/s at 15 cm above the bottom, b)  $V_{sp} = 60$  m/s at 25 cm above the bottom, c)  $V_{sp} = 90$  m/s at 15 cm above the bottom and d)  $V_{sp} = 90$  m/s at 25 cm above the bottom

#### 7.4 The limited of correlation coefficient on CFD simulation

The CFD simulation has two approaches including the TFM approach and the DEM approach. The CFD simulation using the dynamics coefficient of restitution is promptly applied to the DEM approach. The DEM simulation computes the individual momentum particle-based on Newton's laws of motion. The correlation of coefficient of restitution can be utilized directly in the contact force module. The necessary contact parameters such as relative impact velocity, direction and temperature have existed in the module. However, the CFD with TFM approach cannot easily apply to simulate the system using the dynamics coefficient of restitution. The TFM simulation treats the solid phase similar to the fluid phase. The momentum of solid-phase is reported by solid volume fraction and average solid velocity in local cells. Thus, the correlation of coefficient of restitution requires the conversion of the discrete phase to the continuous phase before applying to the TFM simulation.

#### 7.5 Conclusion

The CFD-DEM simulation with the dynamics coefficient of restitution was proposed. The simulation using a dynamics coefficient of restitution had an advantage which eliminated the trial and error for this parameter. The dynamics coefficient of restitution was suitable for the system which changing physical properties, impact velocity and operating temperature occurred inside the system. Moreover, the modification did not affect the computational time even though the modification increased the complexity. Finally, the development of DEM simulation using a dynamics coefficient of restitution in which developed from the experiment was achieved which offered the guideline for further study.

## CHAPTER 8

### Conclusion

The computational fluid dynamics (CFD) has been receiving attention to predict the hydrodynamics profile of gas-solid system due to the power of the computational unit today. However, the CFD simulation requires many modelling parameters in which necessary to iterate until the simulation obtains reliable result, a good agreement with the experimental result. This study initially demonstrated the importance of the coefficient of restitution in the various system including TFM approach and DEM approach. The coefficient of restitution has a value range between 0 to 1. The different value of the coefficient of restitution gave the difference predicted result from the simulation. Chapter 4 studied the effect of coefficient of restitution by one-factor-at-a-time method (OFAT) which varied the coefficient of restitution at the specific operating condition. The reduction of coefficient of restitution enhanced the bubble formation in the gas-solid system such as three interconnected fluidized bed reactors, internal circulating fluidized bed and spouted bed. It affected to the decreasing of solid circulation flux for the system which operated in the cycle for three interconnected fluidized bed reactors and internal circulating fluidized bed. For the spouted bed, the decreasing of the coefficient of restitution increased the bubble which caused the spout at the center of the chamber. For rotating drum, the coefficient of restitution had an effect on the predicted kinetic energy of solid in vertical direction per unit time or power draw. The increasing of the coefficient of restitution raised the power draw of the rotating drum system.

The study using one-factor-at-a-time method could not obtain an interaction effect between contact parameters. Thus, the effect of contact parameters by  $2^k$  factorial experimental design was studied on CFD-DEM simulation of spouted bed reactor in Chapter 5. In this chapter, it illustrated the significant of contact parameters both main effect and interaction effect using the statistical approach as ANOVA analysis. The effect of contact parameter such as friction coefficient (A), the spring constant (B), the ratio of the tangential spring constant to normal spring constant (C), the normal restitution coefficient (D), and the tangential restitution coefficient (E) was explored based on  $2^k$

experimental design. The significant effects on response parameters including the translation kinetic energy of particles, the rotational kinetic energy of particles, the bed expansion, and the standard deviation of pressure drop were demonstrated both individual and interaction between contact parameters. The particle–particle friction coefficient (A), spring constant (B), and normal particle–particle restitution coefficient (D) proposed the major effect on spouted bed simulation. Moreover, the interaction which resulted from the combination from the individual parameters such as AB, AD, BD and ABD also proposed the dominant on the hydrodynamics behaviour. Thus, the involving contact parameters such as the particle–particle friction coefficient (A), spring constant (B), and normal particle–particle restitution coefficient (D) required an extensive attention for the simulation of multiphase flow system such as the fluidized bed reactor.

In Chapter 6, the experiment was conducted to measure the coefficient of restitution from various material type, impact velocity and temperature. The results were gathering with the other works of literature to formulate the correlation of coefficient of restitution. The coefficient of restitution was measured by drop test experimental approach. The kinetic energy dissipation was captured by high speed camera at high frame rate recorded (4000 fps) and analyzed by image processing method. The effect of impact velocity, temperature, and material types on coefficient of restitution were studied. The solid diameter was neglected from the similar characteristic and coefficient of restitution at diameter 3 mm to 6 mm. The decreasing trend of coefficient of restitution was obtained from the increasing of impact velocity and increasing of temperature. The correlation of coefficient of restitution was developed from the experimental results including this study and reference literatures. The logistic equation pattern obtained well agreement to match the coefficient of restitution and impact velocity due to the highest resolution of data. The developed correlation of coefficient of restitution was the function of impact velocity, elastic modulus and Poisson's ratio and temperature. The coefficient in the developed equation was observed and classified into four groups to decrease the truncate error from correlation developing. The excellent agreement between the coefficient of restitution from the correlation and experiment was obtained by free fall

simulation. Moreover, this chapter performed the problem using the coefficient of restitution. The constant coefficient of restitution validated in the specific impact velocity and temperature. But the correlation of coefficient of restitution achieved a reliable value according to the wide range of impact velocity and temperature.

Chapter 7 showed the stability of DEM simulation with dynamics coefficient of restitution from the obtained correlation in Chapter 6. The correlation of coefficient of restitution was applied to the contact force module algorithm in DEM simulation. The guideline for the novel approach of DEM simulation using dynamics coefficient of restitution was proposed. The novel approach can be utilized to the various system such as internal circulating fluidized bed, spouted bed and rotating drum. It improves the simulation procedure to obtain a consistent coefficient of restitution value instead of guessing this modeling parameter.

#### **Research outcomes**

This study proposed the coefficient of restitution measurement by drop test and image analysis. The effect of operating parameters such as impact velocity, material types and temperature were observed the influence on the coefficient of restitution. The correlation was developed from the experimental results in which covered a wide range of solid types. It was suitable for fluidization process and involving process such as rotating drum, cyclone etc. This study proposed the novel approach to apply the dynamics coefficient of restitution with the operating condition including impact velocity and operating temperature. Comparing to the constant coefficient of restitution, the realistic simulation was obtained due to the coefficient of restitution depending on the local area. It was the key to the improvement of DEM simulation to be able to handle more realistic simulation. The DEM simulation with dynamics coefficient of restitution offered the optional feature for further study in which received the convenient for the modeler to avoid the iteration of coefficient of restitution.



### Recommendations for future studies

In this study, the DEM simulation was developed by correlation of coefficient of restitution which gave the convenient for the modeler to set the DEM modeler. However, the multiphase flow of gas – solid system was widely simulated both CFD simulation (Eulerian-Eulerian) and DEM simulation (Eulerian- Lagrangian). The CFD simulation was received attention to simulate the system which contained huge amount of solid phase. It reduced the computational time compared with DEM simulation. It was straightforward to apply the dynamics coefficient of restitution with DEM simulation because the solid movement was computed and resulted in point information. The collision could detect by neighbour search algorithm in which represented the real contact between a pair of solid particles. However, the CFD simulation was developed from the governing equation which based on finite cell or finite volume including gas phase and solid phase. The result of solid phase from CFD simulation was resulted in the average velocity and solid fraction by cell data. Thus, the correlation of coefficient of restitution from this study could not be applied to the CFD simulation directly due to the difference solving approach. To develop the CFD simulation with dynamics coefficient of restitution, the correlation of coefficient of restitution could be transformed the local point function from DEM simulation to local cell function for CFD simulation. The correlation is required to develop in terms of solid volume fraction, solid average velocity in the local cell, cluster parameter, shape factor etc.

## REFERENCES

- Abbasfard, H., Evans, G., & Moreno-Atanasio, R. (2016). Effect of van der Waals force cut-off distance on adhesive collision parameters in DEM simulation. *Powder Technology*, 299, 9-18.
- Agrawal, K., Loezos, P., Syamlal, M., & Sundaresan, S. (2001). The role of meso-scale structures in rapid gas-solid flows. *J. Fluid. Mech.*, 445, 151-185.  
doi:<https://doi.org/10.1017/S0022112001005663>
- Aman, S., Mueller, P., Tomas, J., Kozhar, S., Dosta, M., Heinrich, S., & Antonyuk, S. (2016). Combined viscoelastic and elastic wave dissipation mechanism at low velocity impact. *Advanced Powder Technology*, 27(4), 1244-1250.  
doi:<https://doi.org/10.1016/j.appt.2016.04.012>
- Andrews, A. T., Loezos, P. N., & Sundaresan, S. (2005). Coarse-grid simulation of gas-particle flows in vertical risers. *Industrial and Engineering Chemistry Research*, 44 (16), 6022-6037. doi:<https://doi.org/10.1021/ie0492193>
- Ansari, M. K., Ahmad, M., Singh, R., & Singh, T. (2015). Correlation between Schmidt hardness and coefficient of restitution of rocks. *Journal of African Earth Sciences*, 104, 1-5.
- Aryaei, A., Hashemnia, K., & Jafarpur, K. (2010). Experimental and numerical study of ball size effect on restitution coefficient in low velocity impacts. *International Journal of Impact Engineering*, 37(10), 1037-1044.
- Asegehegn, T. W., Schreiber, M., & Krautz, H. J. (2012). Influence of two-and three-dimensional simulations on bubble behavior in gas–solid fluidized beds with and without immersed horizontal tubes. *Powder Technology*, 219, 9-19.
- Bbosa, L. S., Govender, I., & Mainza, A. (2016). Development of a novel methodology to determine mill power draw. *International Journal of Mineral Processing*, 149, 94-103. doi:<https://doi.org/10.1016/j.minpro.2016.02.009>

- Beetstra, R., van der Hoef, M. A., & Kuipers, J. (2007). Drag force of intermediate Reynolds number flow past mono- and bidisperse arrays of spheres. *AIChE Journal*, 53(2), 489-501.
- Bharadwaj, R., Smith, C., & Hancock, B. C. (2010). The coefficient of restitution of some pharmaceutical tablets/compacts. *International Journal of Pharmaceutics*, 402(1), 50-56. doi:<https://doi.org/10.1016/j.ijpharm.2010.09.018>
- Biele, J., Kessler, L., Grimm, C. D., Schröder, S., Mierheim, O., Lange, M., & Ho, T.-M. (2017). Experimental determination of the structural coefficient of restitution of a bouncing asteroid lander. *arXiv preprint arXiv:1705.00701*.
- Brake, M. (2012). An analytical elastic-perfectly plastic contact model. *International Journal of Solids and Structures*, 49(22), 3129-3141.
- Carneiro, V., & Puga, H. (2018). Temperature Variability of Poisson's Ratio and Its Influence on the Complex Modulus Determined by Dynamic Mechanical Analysis. *Technologies*, 6(3), 81.
- Chand, R., Khaskheli, M. A., Qadir, A., Ge, B., & Shi, Q. (2012). Discrete particle simulation of radial segregation in horizontally rotating drum: Effects of drum-length and non-rotating end-plates. *Physica A: Statistical Mechanics and its Applications*, 391(20), 4590-4596.
- Chu, K., Chen, J., & Yu, A. (2016). Applicability of a coarse-grained CFD-DEM model on dense medium cyclone. *Minerals Engineering*, 90, 43-54.
- Ciavarella, M. (2015). Transition from stick to slip in Hertzian contact with "Griffith" friction: The Cattaneo-Mindlin problem revisited. *Journal of the Mechanics and Physics of Solids*, 84, 313-324.
- Coaplen, J., Stronge, W., & Ravani, B. (2004). Work equivalent composite coefficient of restitution. *International Journal of Impact Engineering*, 30(6), 581-591.
- Coaplen, J., Stronge, W. J., & Ravani, B. (2004). Work equivalent composite coefficient of restitution. *International Journal of Impact Engineering*, 30(6), 581-591. doi:<https://doi.org/10.1016/j.ijimpeng.2003.10.038>

- Crüger, B., Salikov, V., Heinrich, S., Antonyuk, S., Sutkar, V. S., Deen, N. G., & Kuipers, J. (2016). Coefficient of restitution for particles impacting on wet surfaces: An improved experimental approach. *Particuology*, 25, 1-9.
- Cundall, P. A., & Strack, O. D. (1979). A discrete numerical model for granular assemblies. *geotechnique*, 29(1), 47-65.
- Darwish, A. S., Zewail, T. M., Yousef, N. S., & El-Tawail, Y. A. (2015). Investigation of the performance of a batch air spouting bed in conducting ion exchange reactions involving heavy metal removal. *Journal of the Taiwan Institute of Chemical Engineers*, 47, 171-176. doi:<https://doi.org/10.1016/j.jtice.2014.10.003>
- Deb, S., & Tafti, D. (2014). Investigation of flat bottomed spouted bed with multiple jets using DEM–CFD framework. *Powder Technology*, 254, 387-402.
- Deza, M., Battaglia, F., & Heindel, T. J. (2008). *A validation study for the hydrodynamics of biomass in a fluidized bed*. Paper presented at the Fluids Engineering Division Summer Meeting.
- Dias, G. H., Barbosa Guedes, C. L., Tavares da Silva, E., Gomes Angilelli, K., Lopes Coppo, R., & Borsato, D. (2014). Application of the simplex-centroid design with process variable in the optimization of production conditions of B100 biodiesel from sunflower oil. *Acta Scientiarum. Technology*, 36(3).
- Ding, J.-T., Yan, P.-Y., Liu, S.-L., & Zhu, J.-Q. (1999). Extreme vertices design of concrete with combined mineral admixtures. *Cement and Concrete Research*, 29(6), 957-960.
- Ding, J., & Gidaspow, D. (1990). A bubbling fluidization model using kinetic theory of granular flow. *AIChE journal*, 36(4), 523-538.
- Dong, M., Li, S., Xie, J., & Han, J. (2013). Experimental studies on the normal impact of fly ash particles with planar surfaces. *Energies*, 6(7), 3245-3262.
- Esmaili, E., & Mahinpey, N. (2011). Adjustment of drag coefficient correlations in three dimensional CFD simulation of gas–solid bubbling fluidized bed. *Advances in Engineering Software*, 42(6), 375-386.  
doi:<https://doi.org/10.1016/j.advengsoft.2011.03.005>

- Feng, Y., Swenser-Smith, T., Witt, P. J., Doblin, C., Lim, S., & Schwarz, M. P. (2012). CFD modeling of gas–solid flow in an internally circulating fluidized bed. *Powder Technology*, 219, 78-85. doi:<https://doi.org/10.1016/j.powtec.2011.12.007>
- Fogler, H. S. (2010). *Essentials of Chemical Reaction Engineering*: Pearson Education, .
- Garg, R. (2010). Documentation of open-source MFIX–DEM software for gas–solids flows.
- Garg, R., Galvin, J., Li, T., & Pannala, S. (2012). Open-source MFIX-DEM software for gas–solids flows: Part I—Verification studies. *Powder Technology*, 220, 122-137. doi:10.1016/j.powtec.2011.09.019
- Gibson, L. M., Gopalan, B., Pisupati, S. V., & Shadle, L. J. (2013). Image analysis measurements of particle coefficient of restitution for coal gasification applications. *Powder Technology*, 247, 30-43.
- Gidaspow, D. (1994). *Multiphase flow and fluidization: continuum and kinetic theory descriptions*: Academic press.
- Gilardi, G., & Sharf, I. (2002). Literature survey of contact dynamics modelling. *Mechanism and machine theory*, 37(10), 1213-1239.
- Glicksman, L. R. (1984). Scaling relationships for fluidized beds. *Chemical Engineering Science*, 39(9), 1373-1379. doi:[https://doi.org/10.1016/0009-2509\(84\)80070-6](https://doi.org/10.1016/0009-2509(84)80070-6)
- Gorham, D. A., & Kharaz, A. H. (2000). The measurement of particle rebound characteristics. *Powder Technology*, 112(3), 193-202. doi:[https://doi.org/10.1016/S0032-5910\(00\)00293-X](https://doi.org/10.1016/S0032-5910(00)00293-X)
- Guo, Q., Yue, G., Zhang, J., & Liu, Z. (2001). Hydrodynamic characteristics of a two-dimensional jetting fluidized bed with binary mixtures. *Chemical Engineering Science*, 56(15), 4685-4694. doi:[https://doi.org/10.1016/S0009-2509\(01\)00117-8](https://doi.org/10.1016/S0009-2509(01)00117-8)
- Hastie, D. (2013). Experimental measurement of the coefficient of restitution of irregular shaped particles impacting on horizontal surfaces. *Chemical Engineering Science*, 101, 828-836.
- Hertz, H. (1896). On the contact of solids—on the contact of rigid elastic solids and on hardness. *Miscellaneous papers*, 146-183.

- Horabik, J., Beczek, M., Mazur, R., Parafiniuk, P., Ryżak, M., & Molenda, M. (2017). Determination of the restitution coefficient of seeds and coefficients of visco-elastic Hertz contact models for DEM simulations. *Biosystems Engineering*, 161, 106-119.
- Jeremiáš, M., Pohořelý, M., Svoboda, K., Manovic, V., Anthony, E. J., Skoblia, S., . . . Šyc, M. (2017). Gasification of biomass with CO<sub>2</sub> and H<sub>2</sub>O mixtures in a catalytic fluidised bed. *Fuel*, 210, 605-610. doi:<https://doi.org/10.1016/j.fuel.2017.09.006>
- Jiménez, A. E., & Bermúdez, M. D. (2011). 2 - Friction and wear. In J. P. Davim (Ed.), *Tribology for Engineers* (pp. 33-63): Woodhead Publishing.
- Johnson, K. (1985a). Contact mechanics cambridge univ. Press, Cambridge, 95, 365.
- Johnson, K. (1985b). Contact mechanics cambridge univ. Press, Cambridge.
- Jung, J., Gidaspow, D., & Gamwo, I. K. (2005). Measurement of two kinds of granular temperatures, stresses, and dispersion in bubbling beds. *Industrial & engineering chemistry research*, 44(5), 1329-1341.
- Kawaguchi, T., Tanaka, T., & Tsuji, Y. (1998). Numerical simulation of two-dimensional fluidized beds using the discrete element method (comparison between the two- and three-dimensional models). *Powder Technology*, 96(2), 129-138.
- Lazic, Z. R. (2006). *Design of experiments in chemical engineering: a practical guide*: John Wiley & Sons.
- Li, T., Zhang, Y., & Hernández-Jiménez, F. (2016). Investigation of particle-wall interaction in a pseudo-2D fluidized bed using CFD-DEM simulations. *Particuology*, 25, 10-22.
- Li, Y. Q., Gao, X. L., Horner, S. E., & Zheng, J. Q. (2017). Analytical models for the impact of a solid sphere on a fluid-filled spherical shell incorporating the stress wave propagation effect and their applications to blunt head impacts. *International Journal of Mechanical Sciences*, 130, 586-595. doi:<https://doi.org/10.1016/j.ijmecsci.2017.06.015>
- Link, J., Deen, N., Kuipers, J., Fan, X., Ingram, A., Parker, D., . . . Seville, J. (2008). PEPT and discrete particle simulation study of spout-fluid bed regimes. *AIChE journal*, 54(5), 1189-1202.

- Liu, F.-R., Chen, X.-W., Li, Z., & Wang, N.-X. (2017). DEM–CFD simulation of modular PB-FHR core with two-grid method. *Nuclear Science and Techniques*, 28(7), 100.
- Liu, G., Yu, F., Lu, H., Wang, S., Liao, P., & Hao, Z. (2016). CFD-DEM simulation of liquid-solid fluidized bed with dynamic restitution coefficient. *Powder Technology*, 304, 186-197.
- Liu, M., Wen, Y., Liu, R., Liu, B., & Shao, Y. (2015). Investigation of fluidization behavior of high density particle in spouted bed using CFD–DEM coupling method. *Powder Technology*, 280, 72-82.
- Liu, P., & Hrenya, C. M. (2014). Challenges of DEM: I. Competing bottlenecks in parallelization of gas–solid flows. *Powder Technology*, 264, 620-626.
- Lun, C., Savage, S. B., Jeffrey, D., & Chepurmy, N. (1984). Kinetic theories for granular flow: inelastic particles in Couette flow and slightly inelastic particles in a general flowfield. *Journal of Fluid Mechanics*, 140, 223-256.  
doi:<https://doi.org/10.1017/S0022112084000586>
- Luo, K., Fang, M., Yang, S., Zhang, K., & Fan, J. (2013). LES–DEM investigation of an internally circulating fluidized bed: Effects of gas and solid properties. *Chemical Engineering Journal*, 228, 583-595. doi:<https://doi.org/10.1016/j.cej.2013.05.031>
- Mahinpey, N., Vejahati, F., & Ellis, N. (2007). CFD simulation of gas–solid bubbling fluidized bed: an extensive assessment of drag models. In *Computational Methods in Multiphase Flow IV*, (pp. 51-60).
- Mansourpour, Z., Karimi, S., Zarghami, R., Mostoufi, N., & Sotudeh-Gharebagh, R. (2010). Insights in hydrodynamics of bubbling fluidized beds at elevated pressure by DEM–CFD approach. *Particuology*, 8(5), 407-414.  
doi:<https://doi.org/10.1016/j.partic.2010.03.017>
- Marinack Jr, M. C., Musgrave, R. E., & Higgs III, C. F. (2013). Experimental investigations on the coefficient of restitution of single particles. *Tribology Transactions*, 56(4), 572-580.
- Mathur, K. B., & Gishler, P. (1955). A technique for contacting gases with coarse solid particles. *AIChE Journal*, 1(2), 157-164.



- Minamoto, H., Seifried, R., Eberhard, P., & Kawamura, S. (2008). Effects of strain rate dependency of material properties in low velocity impact. *International Journal of Modern Physics B*, 22(09n11), 1165-1170.
- Moysey, P. A., Rao, N. V. R., & Baird, M. H. J. P. t. (2013). Dynamic coefficient of friction and granular drag force in dense particle flows: Experiments and DEM simulations. *248*, 54-67.
- Navarro, H. A., & de Souza Braun, M. P. (2013). Determination of the normal spring stiffness coefficient in the linear spring–dashpot contact model of discrete element method. *Powder Technology*, 246, 707-722.
- Nguyen, T. T., Yu, D., & Park, S. B. (2011). Characterizing the Mechanical Properties of Actual SAC105, SAC305, and SAC405 Solder Joints by Digital Image Correlation. *Journal of Electronic Materials*, 40(6), 1409-1415. doi:10.1007/s11664-011-1534-z
- O'Sullivan, C. (2014). *Particulate discrete element modelling: a geomechanics perspective*: CRC Press.
- Pohndorf, R. S., Camara, Á. S., Larrosa, A. P. Q., Pinheiro, C. P., Strieder, M. M., & Pinto, L. A. A. (2016). Production of lipids from microalgae *Spirulina* sp.: Influence of drying, cell disruption and extraction methods. *Biomass and Bioenergy*, 93, 25-32. doi:<https://doi.org/10.1016/j.biombioe.2016.06.020>
- Qiu, K., Hu, C., Yang, S., Luo, K., Zhang, K., & Fan, J. (2016). Computational evaluation of depth effect on the hydrodynamics of slot-rectangular spouted bed. *Powder Technology*, 287, 51-60.
- Rong, W., Feng, Y., Schwarz, P., Yurata, T., Witt, P., Li, B., . . . Zhou, J. (2020). Sensitivity analysis of particle contact parameters for DEM simulation in a rotating drum using response surface methodology. *Powder Technology*, 362, 604-614. doi:<https://doi.org/10.1016/j.powtec.2019.12.004>
- Stronge, W. (1995). Coupling of friction and internal dissipation in planar collision of compliant bodies. In *Contact Mechanics* (pp. 417-426): Springer.



- Stronge, W. J., Sofi, A. R., & Ravani, B. (2019). Computing the composite coefficient of restitution for inelastic impact of dissimilar bodies. *International Journal of Impact Engineering*, 133, 103333. doi:<https://doi.org/10.1016/j.ijimpeng.2019.103333>
- Sun, Y., Wu, Y.-C. M., Veysset, D., Kooi, S. E., Hu, W., Swager, T. M., . . . Hsieh, A. J. (2019). Molecular dependencies of dynamic stiffening and strengthening through high strain rate microparticle impact of polyurethane and polyurea elastomers. *Applied Physics Letters*, 115(9), 093701.
- Suresh, P., Sreedhar, I., Vaidhiswaran, R., & Venugopal, A. (2017). A comprehensive review on process and engineering aspects of pharmaceutical wet granulation. *Chemical Engineering Journal*, 328, 785-815. doi:<https://doi.org/10.1016/j.cej.2017.07.091>
- Syamlal, M., & O'Brien, T. J. (1989). *Computer simulation of bubbles in a fluidized bed*. Paper presented at the AIChE Symp. Ser.
- Taghipour, F., Ellis, N., & Wong, C. (2005). Experimental and computational study of gas–solid fluidized bed hydrodynamics. *Chemical Engineering Science*, 60(24), 6857-6867. doi:<https://doi.org/10.1016/j.ces.2005.05.044>
- Thornton, C. (1997). Coefficient of restitution for collinear collisions of elastic-perfectly plastic spheres.
- Tommey, R. (1952). Gaseous fluidization of solid particles. *Chem. Eng. Progr.*, 220-226.
- ToolBox, E. (2003). Young's Modulus - Tensile and Yield Strength for common Materials. Retrieved from [https://www.engineeringtoolbox.com/young-modulus-d\\_417.html](https://www.engineeringtoolbox.com/young-modulus-d_417.html)
- ToolBox, E. (2008). Poisson's ratio. Retrieved from [https://www.engineeringtoolbox.com/poissons-ratio-d\\_1224.html](https://www.engineeringtoolbox.com/poissons-ratio-d_1224.html)
- Tsuji, Y., Tanaka, T., & Ishida, T. (1992). Lagrangian numerical simulation of plug flow of cohesionless particles in a horizontal pipe. *Powder Technology*, 71(3), 239-250.
- Verhulst, P.-F. (1845). Resherches mathematiques sur la loi d'accroissement de la population. *Nouveaux memoires de l'academie royale des sciences*, 18, 1-41.

- Wang, Q. J., & Zhu, D. (2013). Hertz Theory: Contact of Spherical Surfaces. In Q. J. Wang & Y.-W. Chung (Eds.), *Encyclopedia of Tribology* (pp. 1654-1662). Boston, MA: Springer US.
- Weir, G., & Tallon, S. (2005). The coefficient of restitution for normal incident, low velocity particle impacts. *Chemical Engineering Science*, *60*(13), 3637-3647.
- Weisstein, E. W. (2003). Logistic equation. <https://mathworld.wolfram.com/>.
- Wen, C., & Yu, Y. (1966). A generalized method for predicting the minimum fluidization velocity. *AIChE Journal*, *12*(3), 610-612. doi:<https://doi.org/10.1002/aic.690120343>
- Wolff, M. F. H., Salikov, V., Antonyuk, S., Heinrich, S., & Schneider, G. A. (2014). Novel, highly-filled ceramic-polymer composites synthesized by a spouted bed spray granulation process. *Composites Science and Technology*, *90*, 154-159. doi:<https://doi.org/10.1016/j.compscitech.2013.11.006>
- Wu, C.-Y., Thornton, C., & Li, L.-Y. J. A. P. T. (2003). Coefficients of restitution for elastoplastic oblique impacts. *14*(4), 435-448.
- Xue, Z., Chen, S., Wang, D., & Xiang, W. (2012). Design and fluid dynamic analysis of a three-fluidized-bed reactor system for chemical-looping hydrogen generation. *Industrial and Engineering Chemistry Research*, *51*(11), 4267-4278. doi:<https://doi.org/10.1021/ie201052r>
- Yang, S., Luo, K., Fang, M., & Fan, J. (2013). Discrete element simulation of the hydrodynamics in a 3D spouted bed: Influence of tube configuration. *Powder Technology*, *243*, 85-95.
- Yang, S., Luo, K., Fang, M., Zhang, K., & Fan, J. (2014). Parallel CFD-DEM modeling of the hydrodynamics in a lab-scale double slot-rectangular spouted bed with a partition plate. *Chemical Engineering Journal*, *236*, 158-170.
- Yang, S., Luo, K., Zhang, K., Qiu, K., & Fan, J. (2015). Numerical study of a lab-scale double slot-rectangular spouted bed with the parallel CFD-DEM coupling approach. *Powder Technology*, *272*, 85-99.

- Yang, S., Sun, Y., Zhang, L., Zhao, Y., & Chew, J. W. (2016). Numerical investigation on the effect of draft plates on spouting stability and gas–solid characteristics in a spout-fluid bed. *Chemical Engineering Science*, 148, 108-125.
- Yang, X., Wang, S., Li, B., Liu, H., & He, Y. (2020). Evaluation of sorption-enhanced reforming over catalyst-sorbent bi-functional particles in an internally circulating fluidized bed. *Advanced Powder Technology*, 31(6), 2566-2572.  
doi:<https://doi.org/10.1016/j.appt.2020.04.020>
- Yurata, T., Lei, H., Tang, L., Lu, M., Patel, J., Lim, S., . . . Li, C. e. (2019). Feasibility and sustainability analyses of carbon dioxide–hydrogen separation via de-sublimation process in comparison with other processes. *International Journal of Hydrogen Energy*, 44(41), 23120-23134.
- Zhang, Q., Wang, S., Lu, H., Wang, Q., Tao, M., & Liu, G. (2018). Impact velocity-dependent restitution coefficient using a coupled Eulerian fluid phase-Eulerian solid phase-Lagrangian discrete particles phase model in gas-monodisperse particles internally circulating fluidized bed. *International Journal of Multiphase Flow*, 105, 142-158. doi:<https://doi.org/10.1016/j.ijmultiphaseflow.2018.04.002>
- Zhang, Y.-J., Wang, J.-J., Gu, X.-P., Feng, L.-F., & Wu, B. (2016). CFD simulation of an agitated gas-fluidized bed: Effects of particle–particle restitution coefficient on the hydrodynamics. *Chemical Engineering Research and Design*, 111, 353-361.
- Zhang, Y., Ye, M., Zhao, Y., Gu, T., Xiao, R., & Liu, Z. (2015). Emulsion phase expansion of Geldart a particles in bubbling fluidized bed methanation reactors: A CFD–DEM study. *Powder Technology*, 275, 199-210.  
doi:<https://doi.org/10.1016/j.powtec.2015.01.064>
- Zhao, Y., Xu, L., & Zheng, J. (2017). CFD–DEM simulation of tube erosion in a fluidized bed. *AIChE journal*, 63(2), 418-437.
- Zhong, W., & Zhang, M. (2005). Pressure fluctuation frequency characteristics in a spout-fluid bed by modern ARM power spectrum analysis. *Powder Technology*, 152(1), 52-61. doi:<https://doi.org/10.1016/j.powtec.2005.01.007>

Zhou, F., Hu, S., Liu, Y., Liu, C., & Xia, T. (2014). CFD–DEM simulation of the pneumatic conveying of fine particles through a horizontal slit. *Particuology*, 16, 196-205.

Zhou, L., Zhang, L., Bai, L., Shi, W., Li, W., Wang, C., & Agarwal, R. (2017). Experimental study and transient CFD/DEM simulation in a fluidized bed based on different drag models. *RSC advances*, 7(21), 12764-12774.





จุฬาลงกรณ์มหาวิทยาลัย  
**CHULALONGKORN UNIVERSITY**

## VITA

**NAME** Tarabordin Yurata

**DATE OF BIRTH** 07 Jan 1992

**PLACE OF BIRTH** Rayong, Thailand

**INSTITUTIONS ATTENDED** Department of Chemical technology, Faculty of Science,  
Chulalongkorn University

**HOME ADDRESS** 53/4 Moo.6, Choeng Noen, Muang Rayong, Rayong, 21000

**PUBLICATION**

- 1) Yurata, T., Liangguang, T., Lim, S., Feng, Y., Peter, W., Piumsomboon, P., and Chalermssinsuwan, B. CFD simulation of a cold model inter-connected three fluidized bed reactors applicable to chemical looping hydrogen production. 2nd International Symposium on Computational Particle Technology & 13th International Conference on CFD in the Minerals and Process Industries, Melbourne, Australia (2018).
- 2) Yurata, T., Feng, Y., Piumsomboon, P., and Chalermssinsuwan, B. Development of CFD-DEM simulation with dynamics restitution coefficient. RGJ University Forum, Bangkok, Thailand (2019).
- 3) Yurata, T., Feng, Y., Piumsomboon, P., and Chalermssinsuwan, B. Development of CFD-DEM simulation with dynamics restitution coefficient. Thailand Science Research and Innovation (TSRI) Congress 2019, Bangkok, Thailand (2019).
- 4) Yurata, T., Hongwu, L., Liangguang, T., Meng, L., Jim, P., Seng, L., Piumsomboon, P., Chalermssinsuwan, B., and Chao'en, Li. Feasibility and sustainability analyses of carbon dioxide – hydrogen separation via de-sublimation process in comparison with other processes. International Journal of Hydrogen Energy 41(44) (2019), 23120-23134.
- 5) Yurata, T., Piumsomboon, P., and Chalermssinsuwan, B. Effect of contact force modeling parameters on the system hydrodynamics of spouted bed using CFD-DEM simulation and 2k factorial

experimental design. *Chemical Engineering Research and Design* 153 (2020) 401-418.

6) Rong, W., Feng, Y., Schwarz, P., Yurata, T., Witt, P., Li, B., Song, T. and Zhou, J. Sensitivity analysis of particle contact parameters for DEM simulation in a rotating drum using response surface methodology. *Powder Technology* 362 (2020) 604-614.

7) Chuenphan, T., Yurata, T., Sema, T., and Chalermnsinsuwan, B. Sensitivity analysis by the 2k factorial experimental design of CO<sub>2</sub> capture with amine gas treating process using Aspen Plus®. The 29th Thai Institute of Chemical Engineering and Applied Chemistry Conference (TICHE2020), Bangkok, Thailand (2020).

#### AWARD RECEIVED

1) Best student oral presentation award from Yurata, T., Liangguang, T., Lim, S., Feng, Y., Peter, W., Piumsomboon, P., and Chalermnsinsuwan, B. CFD simulation of a cold model interconnected three fluidized bed reactors applicable to chemical looping hydrogen production. 2nd International Symposium on Computational Particle Technology & 13th International Conference on CFD in the Minerals and Process Industries, Melbourne, Australia (2018). (Advisor)

2) Best presentation award from Yurata, T., Feng, Y., Piumsomboon, P., and Chalermnsinsuwan, B. Development of CFD-DEM simulation with dynamics restitution coefficient. RGJ University Forum, Bangkok, Thailand (2019).

3) 2nd runner up oral presentation certificate (popular vote) from Yurata, T., Feng, Y., Piumsomboon, P., and Chalermnsinsuwan, B. Development of CFD-DEM simulation with dynamics restitution coefficient. Thailand Science Research and Innovation (TSRI) Congress 2019, Bangkok, Thailand (2019).